CORROSION FATIGUE IN NICKEL BASE ALLOYS

FOR NUCLEAR STEAM GENERATOR APPLICATIONS

by

RONALD GEORGE BALLINGER

B.S., Worcester Polytechnic Institute
(1975)

S.M., Massachusetts Institute of Technology
(1978)

SUBMITTED IN PARTIAL FULFILLMENT
OF THE REQUIREMENTS FOR THE
DEGREE OF

DOCTOR OF SCIENCE

at the

MASSACHUSETTS INSTITUTE OF TECHNOLOGY
February 1982

Signature of Author . . . . . .
Department of Nuclear Engineering
February 5, 1982

Certified by. . . . . .
R.M. Latanision

. . . . . .
R.M.N. Pelloux
Thesis Supervisors

Accepted by . . . . . .
A.F. Henry
Chairman, Departmental Graduate Committee

CORROSION FATIGUE IN NICKEL BASE ALLOYS FOR NUCLEAR STEAM GENERATOR APPLICATIONS

by

RONALD GEORGE BALLINGER

Submitted to the Department of Nuclear Engineering on 5 February 1982 in partial fulfillment of the requirements for the degree of Doctor of Science.

ABSTRACT

An experimental facility has been designed and constructed for use in investigations of fatigue cracking behavior of materials in environments which simulate that which exists in Pressurized Water Reactors and Boiling Water Reactors. The facility consists of a high pressure, high temperature autoclave system composed of three refreshed autoclaves and associated piping and support systems. One of the autoclaves has been incorporated for use in a servo-hydraulic fatigue machine.

Experimental and analytical procedures have been developed and verified for use in experimental determinations of fatigue crack growth rates in a high pressure autoclave system. A complete uncertainty analysis has been conducted and estimates of confidence for the experimentally generated data established. Estimated errors in crack length have been confirmed by actual measurement and Monte Carlo simulation.

Using the experimental facility discussed above, an investigation of the effect of thermal treatment and oxygen potential on the fatigue crack growth behavior of Alloy-600 was conducted. Tests were performed in high purity deoxygenated water and high purity air saturated water at 288°C with sensitized and desensitized material at a frequency of 5 Hz and a ΔK range from 15-35 MPa $\sqrt{m}$. The results of the program were compared to data generated by others.

The results of the program indicate that there is little or no effect of thermal treatment on the fatigue crack growth behavior of Alloy-600 for the experimental conditions used. Fatigue crack growth rates in 288°C high purity deoxygenated water are not significantly different from those in air at room temperature. The results indicate that oxygen has a significant effect. Fatigue crack growth rates in air saturated water at 288°C are approximately ten times that in deoxygenated water at the same temperature.

Thesis Supervisors:	R.M. Latanision	R.M.N. Pelloux
Title:	Professor	Professor

Table of Contents

Table of Contents (cont.)

Table of Contents (cont.)

Table of Contents (cont.)

Figures

Figures (cont.)

Tables

Tables (cont.)

ACKNOWLEDGEMENTS

The successful completion of this thesis was made possible only through a team effort. I am especially greatful for the opportunity to work under the guidance of Professors R.M.N. Pelloux and R.M. Latanision. They always seemd to make the right comments at the right time.

Funding for this project came from the Electric Power Research Institute and I am greatful for the financial support, as well as technical guidance from Tom Passell, Mike Fox, Al McIlree, and Robin Jones

Thanks go to Ron Christensen for his statistical genius and the use of his place of business for much of the analytical work.

Special thanks go to my fellow group members, Kerry Seibein, Dave Knorr and Bill Moshier. Dave made the fractographs in the thesis possible. Bill treated work for my thesis as if it were his own and without his help the job could not have been done.

Finally, special thanks go to Heather Kraemer. That she did an outstanding piece of work in typing the thesis will be obvious if you read further. What is not obvious is the assistance provided by someone who cares.

1.0 Introduction

The use of corrosion resistant materials in nuclear power systems is mandated by the requirement that circulating corrosion products, which would become radioactive and increase personal exposure, be kept to an absolute minimum. As a result, austenitic stainless steels and nickel base alloys are widely used materials of construction. Alloy-600, an austenitic nickel base alloy, containing approximately 14-17 wt % Cr, 6-10 wt % Fe, and 72% Ni, is used extensively in the U.S. for Pressurized Water Reactor (PWR) Steam Generator tubing material, as well as for other components such as piping and fittings, pump casings and instrumentation penetrations. Alloy-600 is used in Boiling Water Reactor (BWR) environments for safe ends and other fittings.

The original decision to use Alloy-600 for applications in the nuclear industry was based on the material's superior general corrosion resistance and its immunity to stress corrosion cracking in the presence of chloride. However, experience has led to the realization that the alloy is susceptible to various forms of stress assisted cracking, intergranular attack, and fatigue assisted failure. Failures have occurred in both normal chemistry environments and in faulted conditions. Failures have initiated from both the primary and secondary systems in PWRs. Fatigue has been implicated in a recent Once Through Steam Generator (OTSG) failure [1] which necessitated the plugging of 139 of a total of 90,000 tubes.

The proliferation of environmentally assisted problems, which have occurred with Alloy-600, has led to several studies with the goal of improving the material's resistance to selected environments. Airey and co-workers [2] have conducted several studies in an attempt to adjust the thermal treatment of tubing material and improve its resistance to attack in caustic environments. These environments are postulated to exist within the tube to tube sheet crevice of some older recirculating steam generators. He found that a thermal treatment consisting of an age at approximately 700°C for 15 hours produced a microstructure that exhibited superior performance in deaerated caustic, an environment thought to simulate that in the tube sheet crevice.

The susceptability to cracking of Alloy-600 in primary chemistry environments, both PWR and BWR, has been demonstrated by several studies [3-6]. In the primary system environments the presence of a fatigue loading component, be it of thermal or mechanical origin, can not be discounted. In the case of a steam generator tube, the fatigue component is likely to be vibrationally induced, as pointed out in reference 1, and is likely to be of a high cycle nature dominated by the required initiation time. In the case of thicker sections, such as BWR safe ends and other components such as pump casings, fatigue crack growth is likely to be an important consideration in evaluating component life. Thus, there is a need for information concerning the fatigue crack growth behavior of Alloy-600 in PWR and BWR environments.

Despite the potential usefulness of fatigue cracking information for Alloy-600 in PWR and BWR operating environments, the amount of data available in the literature is almost non-existant. The purpose of this thesis is to investigate the effect of thermal treatment on the fatigue crack growth behavior of Alloy-600 in high purity deaerated water and thus provide needed information to fill an existing void. This investigation is part of a larger investigation designed to provide fatigue cracking information for several nickel base alloys used in the nuclear power industry.

The overall thesis program was divided into four major tasks: (1) the assessment and definition of the overall problem, (2) the design and construction of a high temperature autoclave system for use in the program, (3) the development and validation of experimental techniques for use in the program, and (4) the generation and interpretation of experimental fatigue crack growth data. With these divisions of labor in mind, this document is divided into eight chapters including this introduction. Chapter 2 describes the overall approach to the, Task 1, program. The third chapter presents what limited data there currently exists, describing the fatigue cracking behavior of Alloy-600. Chapter 4 describes the material used for the experimental program. Chapters 5, 6, and 7 describe each of the three remaining major tasks in detail and chapters 8-9 provide a summary, draw conclusions, and suggests recommendations for further study.

2.0 Description of Research Program

The research program was divided into four major tasks. The purpose of Task one was to define the problem and idenfity a course of action for completion of the three subsequent tasks. Task two consisted of the design and construction of an autoclave system for use in the experimental program. Task three consisted of the development and verification of test methods and analysis procedures to be used in the experimental program. Finally, Task four contained the actual experimental program which was defined in Task one.

2.1 Task 1: Program Definition

This task had, as its major goals, the compilation and evaluation of previously reported work, the identification of a reasonable set of experimental parameters, the identification of material heat treatments to be used, and the identification of a test matrix for completion of the investigation.

An extensive literature search was conducted to identify previous published work concerning the fatigue crack growth behavior of Alloy-600. The results of this literature search are reported in Section 3, but the overall conclusion is that very little work had been done in Light Water Reactor (LWR) environments.

Because of the apparent lack of published results, considerable freedom was available for definition of a set of

experimental parameters. The decision was made to limit this study to an environment of 288°C high purity deoxygenated water. These conditions partially simulate PWR operating conditions and serve as a base line for the future evaluation of higher oxygen content environments, typical of BWR systems. Table 2.1 lists the environmental conditions decided upon for the experimental program.

The definition of an appropriate set of metallurgical conditions for the test program was dictated by the requirement that the material used be prototypic of the type and conditions used in service. At the same time, the material used had to be available in the proper form for the type of specimens used. Table 2.2 lists the general metallurgical conditions decided upon for the program.

Since most of the Alloy-600 in service is used for steam generator tubing, it was decided to use a material whose microstructure was similar to tubing. This microstructure, however, is also similar to that used for other components used in the plants. The carbon content decided upon is also consistent with that used for tubing.

The heat treatments decided upon were based upon duplicating: (1) the most severe metallurgical conditions with respect to sensitization which could exist in "mill annealed" tubing and other components presently in service, and (2) microstructural conditions present in newer generation material which have been healed with respect to chromium depletion. Early on in the program a problem was encountered

Table 2.1

Environmental Conditions for

Experimental Program

Solution	High Purity Water
Temperature	288°C
Oxygen	<40 PPB
PH	7.0
Resistivity	>10 megohm-Cm
Flow Rate	3.8 l/hr

Table 2.2

General Metallurgical Conditions for

Alloy-600 Used in the Program

Microstructure	As close to tubing as possible
Carbon Content	.03% to duplicate tubing
Heat Treatments	Mill annealed + aged 2 hrs @ 700°C
	Mill annealed + aged 120 hrs @ 700°C

concerning just what "mill annealed" really meant. After consultations with several manufacturers of Alloy-600 material, the conclusion was the "mill annealed" could mean just about anything short of water quenched, with regard to cooling rates, depending on section thickness. It was thus apparent that a wide degree of variation with respect to sensitization, the susceptibility of the alloy to intergranular attack due to grain boundary chromium depletion, could exist in service. This is especially true when one considers the post fabrication heat treatments that components, especially steam generators, receive to relieve fabrication induced stresses. For this reason the first heat treatment chosen was an age for 2 hours at 700°C of the as received "mill annealed" material. As will be discussed in Section 4, this heat treatment produced the most severely sensitized material.

The second heat treatment was chosen to allow simulation of a thermal treatment now being given to Westinghouse manufactured tubing, which is designed to result in better performance over "mill annealed" material in off normal crevice conditions which might exist in the tube to tube sheet region in some steam generators. The Westinghouse treatment, 705°C/15 hours, is designed to insure that any sensitization, present in the "mill annealed" condition, is removed. The choice of an age at 700°C for 120 hours for this investigation was intended to insure that a healed microstructure was produced independent of variability in the starting material.

A complete description of the material used is given in Section 4.

The choice of a carbon content of .03 wt % was made to insure compatibility with typical tubing material. Scarberry [7] and Tedman and Vermilyea [8] have shown that the response to heat treatment of Alloy-600 and the subsequent corrosion behavior is a function of the carbon content and morphology.

The mechanical parameters for the test program were decided upon based on the desirability of being able to compare results with what limited data is available and by the desire to complete the experimental program in a reasonable amount of time. Table 2.3 lists the mechanical parameters decided upon.

The specimen dimensions were dictated by the form that the material used in the program was supplied in, 12.7 mm thick plate. These size requirements placed certain restrictions on the range of validity for the test results. These restrictions are discussed in Section 6.

The precrack and test cyclic frequencies were decided upon based primarily on time considerations. It was expected, however, that based on the work of Speidel [9] discussed in Section 3, that testing at a frequency of 5 Hz would eliminate any affects due to time dependent stress corrosion cracking. Precracking in air allowed the crack to be clearly defined, physically, prior to each test so that an accurate measurement could be made after the test as part of the test

Table 2.3

Mechanical Parameters for

Test Program

Specimen Type	Compact Tension (ASTM E547-68T)
Specimen Thickness	12.7 mm
Specimen Width	50.8 mm
Test Frequency	5 Hz
Stress Ratio $\frac{\text{min load}}{\text{max load}}$	0.05
Wave Shape	Sine
Test Method	Constant-Loan-Amplitude (ASTM E647-78T)
Crack Length Measurement Technique	Compliance
Crack Mouth Opening Displacement Measurement Method	Direct Mounted Linear Variable Differential Transformer
Precrack Environment	Air, Room Temperature
Precrack Frequency	80 Hz

results validation discussed in Section 6.

The decision to use elastic compliance measurement to determine crack length was based on the apparent simplicity of the technique and the lower instrumentation costs compared to other techniques.

The final test matrix decided upon for the experimental program is shown in Table 2.4. In addition, several additional tests were performed on the "as received" material and material solutionized at 1150°C for 15 minutes.

2.2 Task 2: Autoclave System Design and Construction

A detailed description of the high pressure autoclave system is given in Section 5. The overall design of the system was arrived at after consultation and site visits with several other investigators active in the field. The final design incorporated what the author believes to be the best features of several other designs, along with additional features unique to this system. Prime considerations which governed the overall design included: (1) simplicity and ease of operation, (2) reliability, and (3) safety.

The question of system safety received special attention since, to the author's knowledge, the autoclave system used in this study represents the only refreshed autoclave system in operation in a university environment. The location and potential for accidental accessibility of the system by untrained personnel required that the system be absolutely fool proof. This objective was achieved by the use of mul-

Table 2.4

Experimental Test Matrix

Heat Treatment	Environment	Number Tests
MA2 [1]	25°C, Air	1
MA120 [2]	25°C, Air	1
MA2	288°C, H.P. Water	2
MA120	288°C, H.P. Water	2

[1] Mill annealed followed by an age at 700°C for 2 hours

[2] Mill annealed followed by an age at 700°C for 120 hours

tiple safety systems. Experience has born out the achievement of the above mentioned goals.

2.3 Task 3: Development and Verification of Test Methods and Analysis Procedures

The purpose of this task was to identify appropriate test methods and to develop experimental and analytical techniques for use in the data acquisition and reduction. As with the design of the autoclave system, the starting point was a blank piece of paper. It soon became apparent that a perhaps as significant a contribution to the field would be made in the area of test procedures and evaluation as from the actual numerical results.

The currently recommended procedures for fatigue crack growth rate testing were evaluated and found to be inadequate for testing in autoclave systems such as the one used in this study. Because of this inadequacy, a full uncertainty analysis of the overall procedures and system was conducted to establish appropriate data reduction procedures and to establish confidence limits for the crack growth rate data generated.

The work in this task provided recommendations regarding analytical procedures for data acquisition and reduction. A detailed description of the results of this task are given in Section 6.

2.4 Task 4: Experimental Program

The experimental program was conducted for the conditions arrived at in Task 1. Data acquisition and analysis were performed using procedures developed in Task 3. The results of the experimental program are presented in Section 7.

3.0 Fatigue Crack Growth Behavior of Alloy-600

Despite the extensive use of Alloy-600 in the power and chemical industry, very little work has been published concerning the fatigue cracking hehavior of this alloy. This lack of published data is no doubt partially due to the fact that in the past Alloy-600 was primarily used in the chemical industry in applications where the primary motivation for its use was its excellent corrosion resistance. Until the advent of its use in power generation and energy conversion applications, the conditions which might be expected to influence fatigue crack growth, namely high temperatures combined with a corrosive environment and high stresses, were not normally present. In the power generation and energy conversion industry not only are the above mentioned conditions normally present but the cost of a premature failure of a component can be extremely high. Still, the amount of published data is sparse. Speidel [9], in a paper on the general subject of corrosion fatigue in Fe-Ni-Cr alloys, shows data for fatigue crack growth in Alloy-600 in air and molten NaOH at 335°C. His data indicated that there was no difference in crack growth rates between material tested in air and that tested in molten NaOH at 335°C. Heat treatment had no effect and he speculated that, were it not for the high oxygen concentration in the NaOH, the crack growth rates might be lower. His tests were performed using a cyclic frequency of 2.5 Hz sine wave.

Speidel makes two important points in his paper: (1) when the fatigue crack growth rates for Alloy-600 and other Fe-Ni-Cr alloys are normalized with their modulus of elasticity, there is a general trend for all of these alloys to exhibit similar behavior, (2) he points out the fact that, depending on test frequency and stress intensity factor range, there can be a significant contribution to the fatigue crack growth rate from time dependent stress corrosion cracking. He speculates that, in the case of Alloy-600, a significant contribution to the overall crack growth rate from stress corrosion cracking should not be seen until cyclic frequencies below 10^{-3} Hz for his test conditions.

James [10], has reported fatigue crack growth data for Alloy-600 in air and sodium in the temperature range of 25-600°C as a function of frequency (.0014-6.67 Hz), stress ratio, Pmin/Pmax, (.05-.6), and thermal aging treatment. His data showed an increase in the fatigue crack growth rate with decreasing cyclic frequency and an increase in rate with an increase in stress ratio. He found that the fatigue crack growth rates in sodium at 427°C were less than the corresponding growth rates in air. He attributed this to the low oxygen concentration in the sodium, resulting in a more benign environment. He found no effect of thermal aging at 538°C for 18,000 hours or 649°C for 14,500 hours. His material, as received, had been annealed at 863°C for 45 minutes. He reported no data as to the degree of sensitization of his

material, but based on the above information one might speculate that the "as received" material was at least partially sensitized while the long thermal agings most certainly resulted in a healed microstructure with regard to chromium depletion.

The dependence of crack growth rate on the stress ratio with the maximum load held constant prompted James to normalize his data by plotting crack growth rate with respect to K_{eff} where:

$$K_{eff} = K_{max} (1-R)^{m} \qquad 2.1$$

where, for Alloy-600 m ranged from 0.4 at 427°C to 0.7 at 538°C. Using this procedure he was able to band the data for a given temperature. The strong temperature dependence of m indicates that an influence of creep crack growth may be manifesting itself as the temperature is increased.

Hale et. al [11] have published a limited amount of data for fatigue crack growth in Alloy-600 in high purity oxygenated water at 288°C. No specifics were given concerning the microstructure other than to mention that their material was tested in the "as received" condition. Their cyclic wave form was a sawtooth with cyclic frequencies ranging from .005 to .083 Hz. They observed that crack growth rates for Alloy-600 were generally slower than for 300 series stainless steels tested under the same conditions. Their data represents the only data, to this point, for conditions simulating power reactor environments.

Mills and James [2] have presented additional fatigue crack growth data for the same material reported on earlier by James [10]. Their investigation concentrated on a test temperature of 427°C in air and sodium with a very low oxygen concentration. They found that the fatigue crack growth rates were from 2-4 times lower in sodium than in air. In fact, the growth rates in sodium at 427°C were virtually identical to those in air at room temperature.

The paper by Mills and James [12] contains the only reasonably detailed fractographic analysis of the crack surfaces after testing. They found that, for low growth rates, the fracture surfaces were crystallographic in appearance with faceted features. At high growth rates the surfaces still exhibited a faceted appearance but the surface now exhibited fatigue striations.

Finally, Was [13] has investigated the effect of thermal treatment and applied electrochemical potential on the fatigue crack growth behavior of Alloy-600 at room temperature. In addition to the effect of applied potential and thermal treatment, his investigation also addressed effects of frequency, mean stress and hydrogen precharging. He found that there was little affect of frequency in air in the frequency range from 1-10 Hz, but that there was a slight increase in crack growth rate with decreasing frequency in this range when the tests were performed at open circuit potential in 1 normal H_2SO_4. At an applied potential of -700 Mv (SCE), a significant frequency effect was observed

with fatigue crack growth rates increasing by a factor of approximately 4 at a ΔK of 35 MPa $\sqrt{m}$ as the test frequency decreased from 10 to .25 Hz. This effect was observed regardless of thermal treatment. At a frequency of 1 Hz he observed a 2.5 fold increase in crack growth rates for specimens tested at -700 Mv (SCE) when compared to the open circuit case.

With regard to thermal treatment, Was observed no significant effect by itself for specimens aged at 700°C for 0.5, 10, and 100 hours.

An increase in mean stress was reported to increase the crack growth rate but only marginally for strees ratios, Pmin/Pmax, between .05 and 0.6.

The addition of a hold time was observed to cause crack bifurcation which made crack growth rate determination impossible.

The increase in crack growth rates, with the imposition of a cathodic potential, was attributed to the presence of hydrogen and a partial transition from a transgranular to an intergranular fracture mode, was cited as supporting evidence. However, hydrogen precharging for up to 480 hours was observed to have no effect. He points out, however, that 4000 hours would be required for hydrogen to reach the center of his specimens under his charging conditions.

The data discussed thus far represents, to the authors knowledge, the extent of the published data on fatigue crack growth of Alloy-600. It is evident that the available data

is sparse at best and non-existent for most LWR operating conditons. For later comparison, Figure 3.1 shows a plot of the available data exclusive of the controlled potential tests which are relevent to this investigation. Table 3.1 lists the conditions under which the data in Figure 3.1 were obtained.

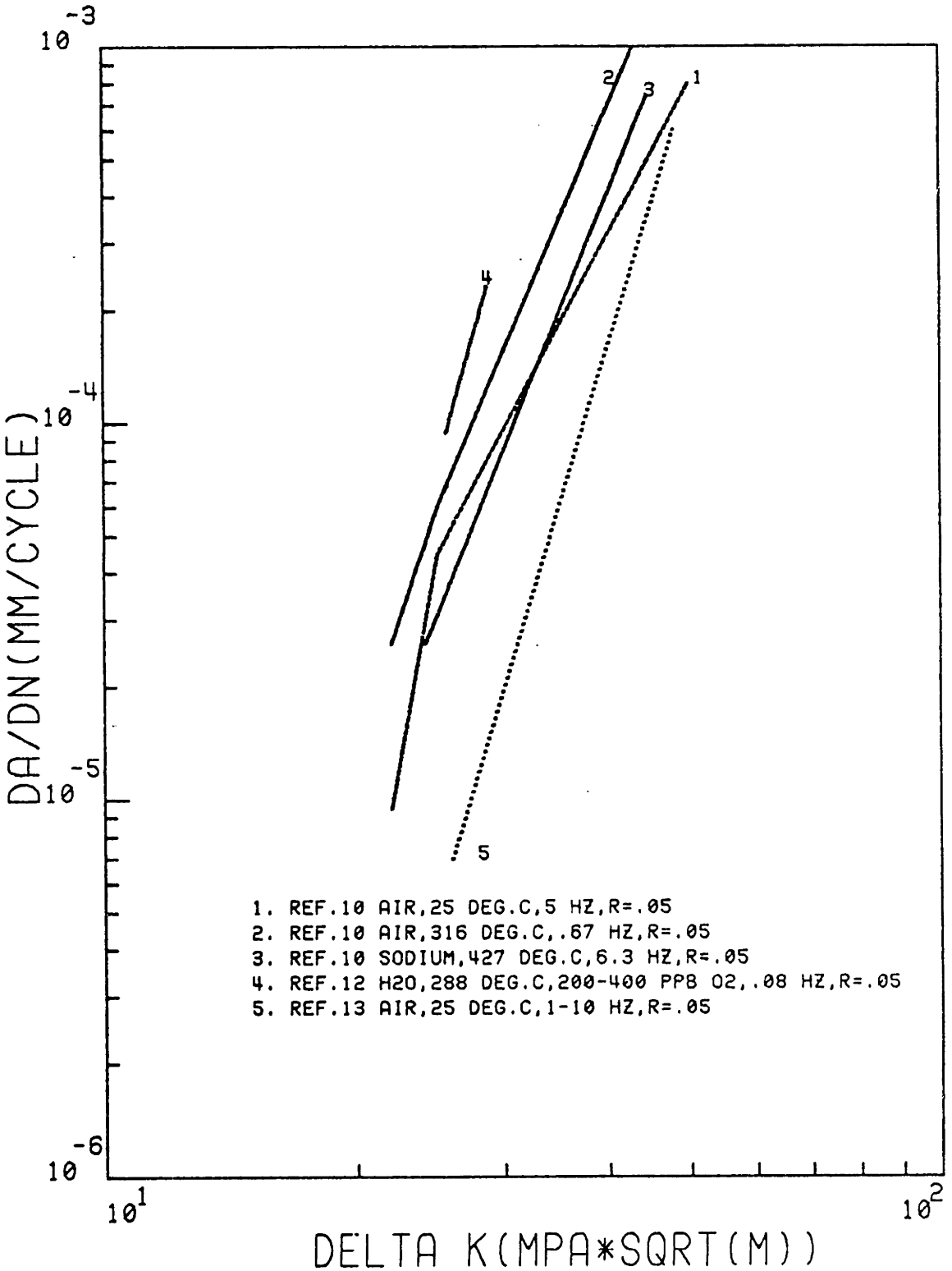

FIGURE 3.1 COMPILATION OF ALLOY-600 FATIGUE CRACK GROWTH DATA FROM PREVIOUS STUDIES.

4.0 Description of Materials

The material requirements for the experimental program were identified as part of Task 1 described in Section 2. Also identified were the mechanical test parameters and the specimen geometry. A conflict arose between the requirement that the carbon content be typical of tubing and that the specimen be of the compact tension design. Alloy-600 plate material was not commercially available with a carbon content of .03 w/o. The reconciliation of this conflict necessitated the fabrication of a special heat of material in the thickness desired with the proper carbon content.

4.1 Fabrication of Plate for Experimental Program

The fabrication schedule for the plate material was tailored in an attempt to duplicate the general microstructure found in tubing material. An attempt was also made to produce a carbide morphology in the material similar to that found in "mill annealed" tubing. Duplication of general tubing chemistry was insured by using actual tubing hollows as starting material.

The plate was fabricated in three steps. First Tube Reduced Extrusions (TREX) were obtained from Huntington Alloys, Inc. The TREXs were part of a shipment of material for the Westinghouse tubing fabrication facility at Blairsville, Pa. The heat number for the material was NXQ922. Table 4.1 shows the chemical analysis for this heat.

The tubing TREXs were sent to the International Nickel

Table 4.1

Chemical Analysis for TREX Material

Used for Plate Fabrication

Heat #NX0922*

Element	Wt%	Nominal	Element	Wt%	Nominal
C	.03	.15 max	Si	.24	.5 max
Mn	.26	1.0 max	Cu	.01	.5 max
Fe	8.51	6-10	Ni+Co	76.31	72 min
S	.001	.015 max	Cr	14.64	14-17

* Huntington Alloys, Inc., Huntington, West Virginia

Table 4.3

Element	Wt%	Element	Wt%
C	.032±.001	Ti	.3
Mn	.18	Mg	<.001
Fe	6.99	Co	.005
S	.003±.001	Mo	.017
Si	.24	B	.001±.001
Cu	.006±.001	P	.003±.001
Cr	14.73	Ni	Balance
Al	.119		

Company Research and Development Laboratory in Sterling Forest, NY for remelting.

The tubing TREXs were remelted and cast into a five inch square billet. The billet was then hot rolled to a thickness of 19 mm. The hot rolled plate was then shipped back to Huntington Alloys, Inc. for further processing to a final thickness of 12.7 mm. Table 4.2 shows the fabrication schedule in more detail. A chemical analysis on the refabricated material was performed and the results are tabulated in Table 4.3.

4.2 Microstructure of Alloy-600 Plate Material

The object of the fabrication schedule for the Alloy-600 materials was to attempt to produce a microstructure similar to that which is found in nuclear steam generator tubing material.

When one attempts to duplicate the vendor's mill annealed microstructure, a problem is encountered immediately--that is that all of the vendors start out with a different mill annealed structure due to slightly different fabrication schedules. In particular, the final annealing temperature-time envelope is different for each vendor. Figure 4.1 shows the microstructure of the various vendor's tubing and the differences are immediately apparent.

The parameters which have the major influence on the final microstructure include (1) the final annealing temperature time envelope, (2) the carbon content, and (3) the

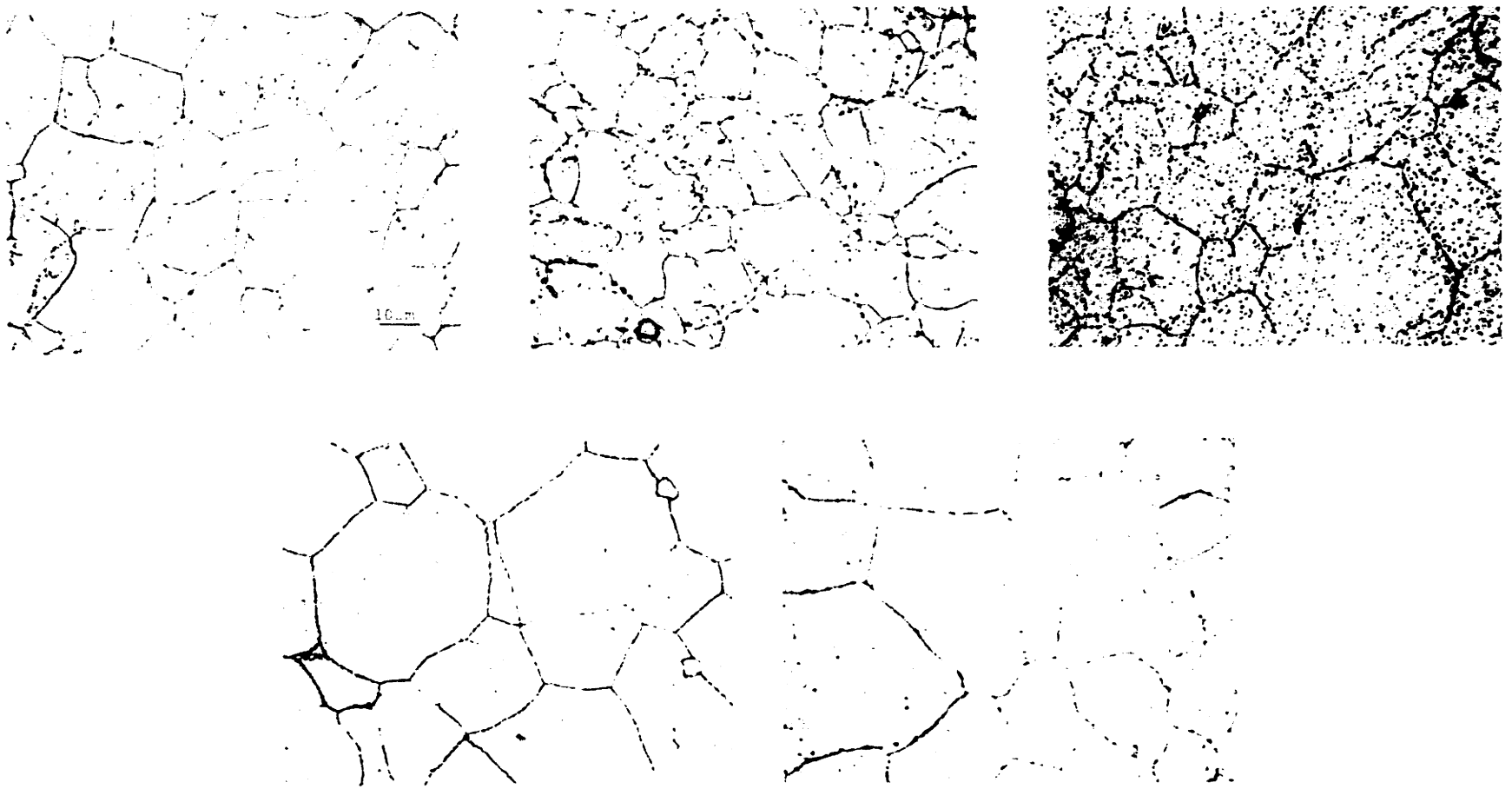

Figure 4.1 Microstructure of Combustion Engineering, Westinghouse mill-annealed, Westinghouse thermally-treated, B&W mill-annealed and B&W stress-relieved tubing, moving clockwise from top left. Dimension marker applies to all.

Table 4.2

Thermomechanical Processing Schedule
for Alloy-600 Material

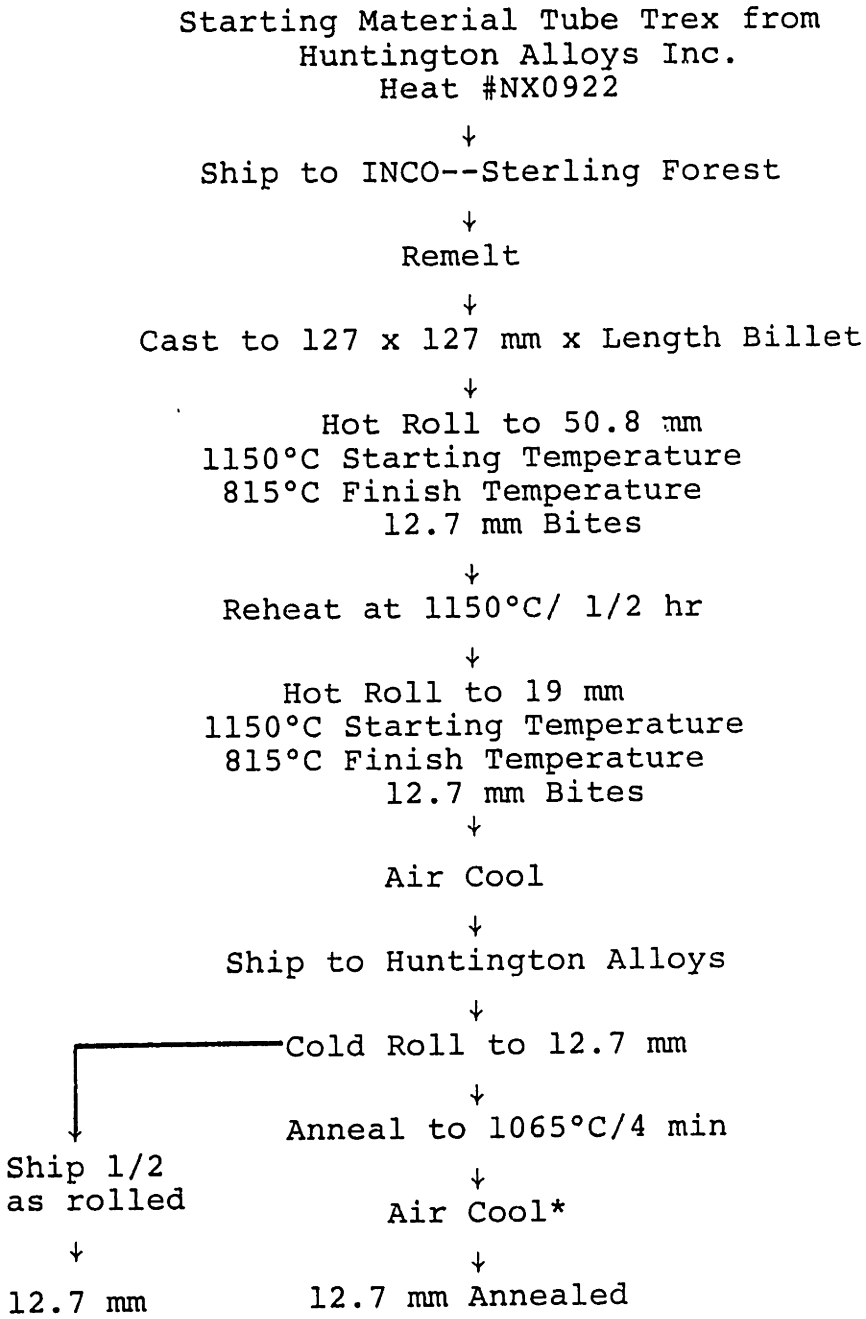

*Pieces 101.6 mm x 610 mm x thickness stacked 4 high for air cool (approximate cooling time to room temp 1/2 hr, approximate cooling time to 400°C 15 min.)

level of cold work present prior to the final anneal.

4.2.1 Final Annealing Temperature-Time Envelope

The annealing temperature-time envelope will influence the final grain size, carbide morphology and sensitization behavior of the material. Above the recrystallization temperature, which is a function of the amount of cold work, grain growth is inhibited until the carbides in the matrix are solutionized. After this occurs, rapid grain growth can occur. Annealing below the carbide resolution temperature results in recrystallization with very little grain growth.

The rate of cooling from the annealing temperature is important with respect to carbide precipitation. If the material is quenched quickly enough no precipitation occurs. At slower cooling rates, precipitation occurs, the extent and location of which depends on the cooling rate.

According to data published by Huntington Alloys, Inc., little grain growth occurs until the temperature is higher than 1010°C after which grain growth occurs at an increasing rate with increasing temperature. The carbides begin to dissolve at 1010°C.

4.2.2 Carbon Content

The solubility of carbon in the Alloy-600 matrix is a function of temperature. Scarberry [7] has investigated the solubility of carbon in Alloy-600 as a function of

temperature. A fit to his data indicates a rough correlation between temperature and solubility for 100 hour soaks at temperature of $T(°C) = 1455.73+131.82 \ln (C_f)$. C_f = weight percent carbon.

4.2.3 Level of Cold Work

The amount of cold work has an effect on the total energy of the system and hence the recrystallization temperature. Figure 4.2 shows the effect of prior cold work on the recrystallization temperature.

4.2.4 Vendor Microstructure (Mill Annealed Material)

Figure 4.1 shows the microstructures present in the vendor's mill annealed material. The Combustion Engineering (CE) material steel exhibits a rolling structure in the carbide morphology. The grain boundaries are relatively free of carbides. These two observations would seem to indicate that the material was recrystallized below the carbide resolution temperature or for too short a time for resolution.

The Westinghouse material exhibits the same grain size as that for CE but has a more course carbide structure with both inter- and intragranular carbides. The grain boundaries show some pinning by carbides. These observations would seem to indicate at least a partial resolution of the carbides during the anneal with some precipitation occurring on cool down. The annealing temperature would have been higher than that for CE.

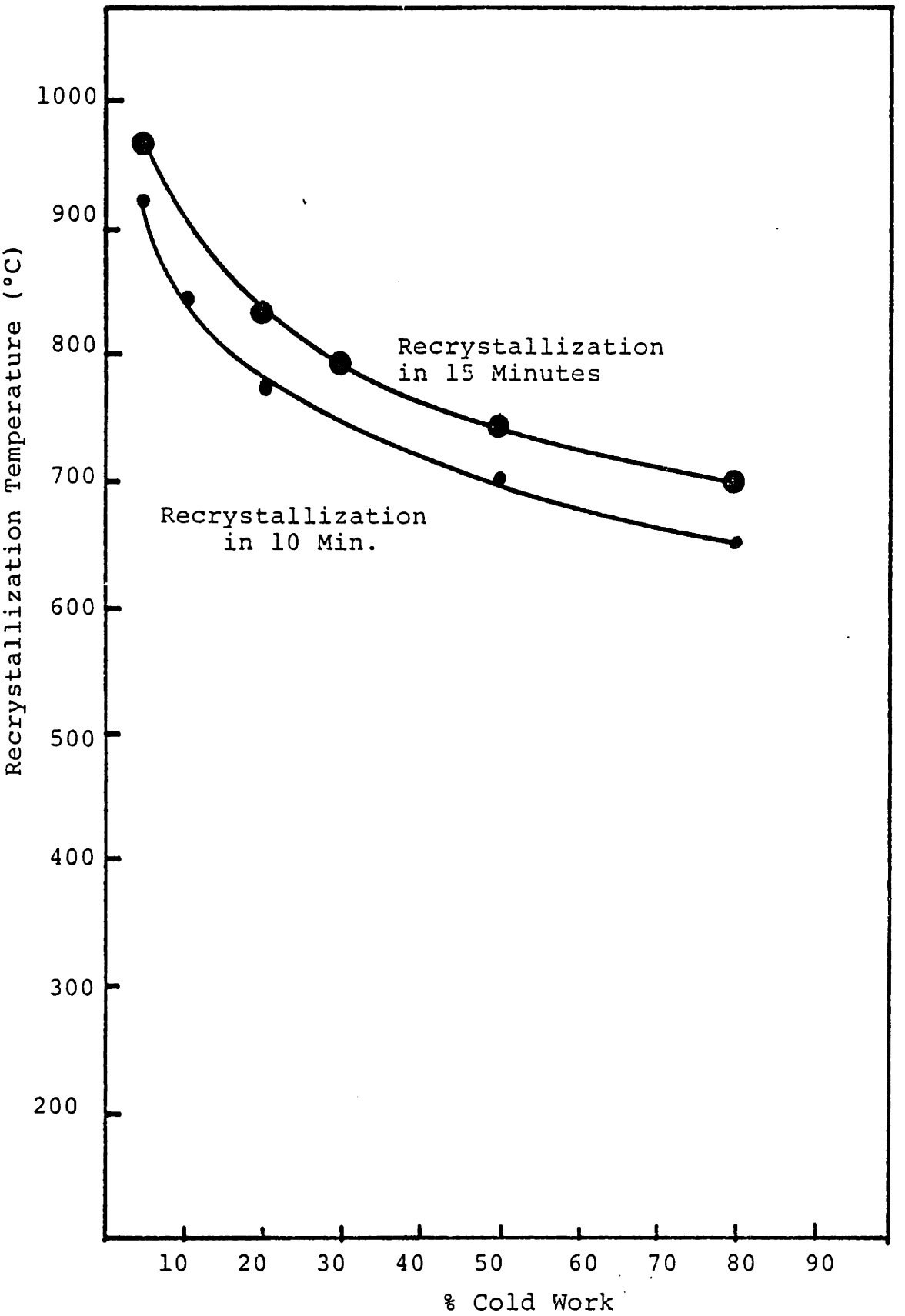

Figure 4.2 Effect of Cold Reduction on Recrystallization Temperature of Alloy-600

The B&W mill annealed material exhibits a larger grain size than either CE or Westinghouse. The grain boundaries are more heavily decorated with carbides. We conclude that the B&W anneal was at a high enough temperature for a long enough time to solutionize the carbides and allow grain growth to occur. (B&W tubing has a higher carbon content also). The carbides which decorate the grain boundaries precipitated upon cool down.

4.2.5 Alloy-600 Plate Microstructure

Figure 4.3 shows the microstructure of the 0.03 w/o carbon plate. From a microstructural point of view, it is apparent that the plate 0.03 w/o carbon mill annealed structure almost duplicates the B&W MA microstructure. Further analyses of the corrosion behavior was necessary to determine if we had indeed duplicated the B&W microstructure.

4.3 Alloy-600 Plate Mechanical Properties

Mechanical properties for the Alloy-600 material were determined at room temperature and at 300°C. Table 4.4 shows the results.

4.4 Corrosion Behavior of the Alloy-600 Plate Material

Having approximately duplicated a general tube type microstructure, the extent of carbide precipitation and grain boundary chromium depletion was investigated using the Streicher test as the indicator of grain boundary chro-

Figure 4.3 Microstructure of .03 w/o Carbon Plate

Table 4.4

Mechanical Properties of Alloy-600
Plate Material

Test Temp	12% Offset Yield (MPa)	UTS (MPa)	Uniform Elongation (%)	Total Elongation (%)	Reduction in Area (%)
25°C	310.3	640	30	36	70
300°C	205	600	32	40	65

Table 4.5

Streicher Test Parameters

Solution Composition

236 ml H_2SO_4 (50.5 wt%)

400 ml H_2O

25 g $(Fe_2SO_4)_3$

Procedure: Immersion in boiling solution for 24 hours

mium depletion. Streicher tests were performed on coupons aged at 700°C for 10 min., 30 min., 2 hrs., 10 hrs., 24 hrs., and 120 hrs. Further tests were performed on coupons aged at 600°C for 10 min., 30 min., 2 hrs., 10 hrs., 24 hrs., 72 hrs., 120 hrs., and 216 hrs. The tests were performed in accordance with ASTM-A262, "Detecting Susceptibility to Intergranular Attack in Stainless Steels", practice B, "Ferric Sulfate-Sulfuric Acid Test for Detecting Susceptibility to Intergranualr Attack in Stainless Steels". The only deviation from this procedure consisted of a shortening of the immersion time from 120 hours to 24 hours or less depending on sample corrosion rates. Table 4.5 lists the test parameters. Table 4.6 and Figure 4.4 show the results of the investigation.

For comparison purposes Streicher test results for several vendor tubing types are shown in Table 4.7.

The results of the corrosion tests indicate that the Alloy-600 plate material for this investigation exhibits a slightly higher degree of susceptability to intergranular attack than the Westinghouse mill annealed material. This is not surprising since the cooling rate of 12.7 mm plate is likely to be slower than that for tubing. The results also show that the peak degree of susceptibility occurs at an aging time of 2 hours and that complete healing has occurred after 24 hours.

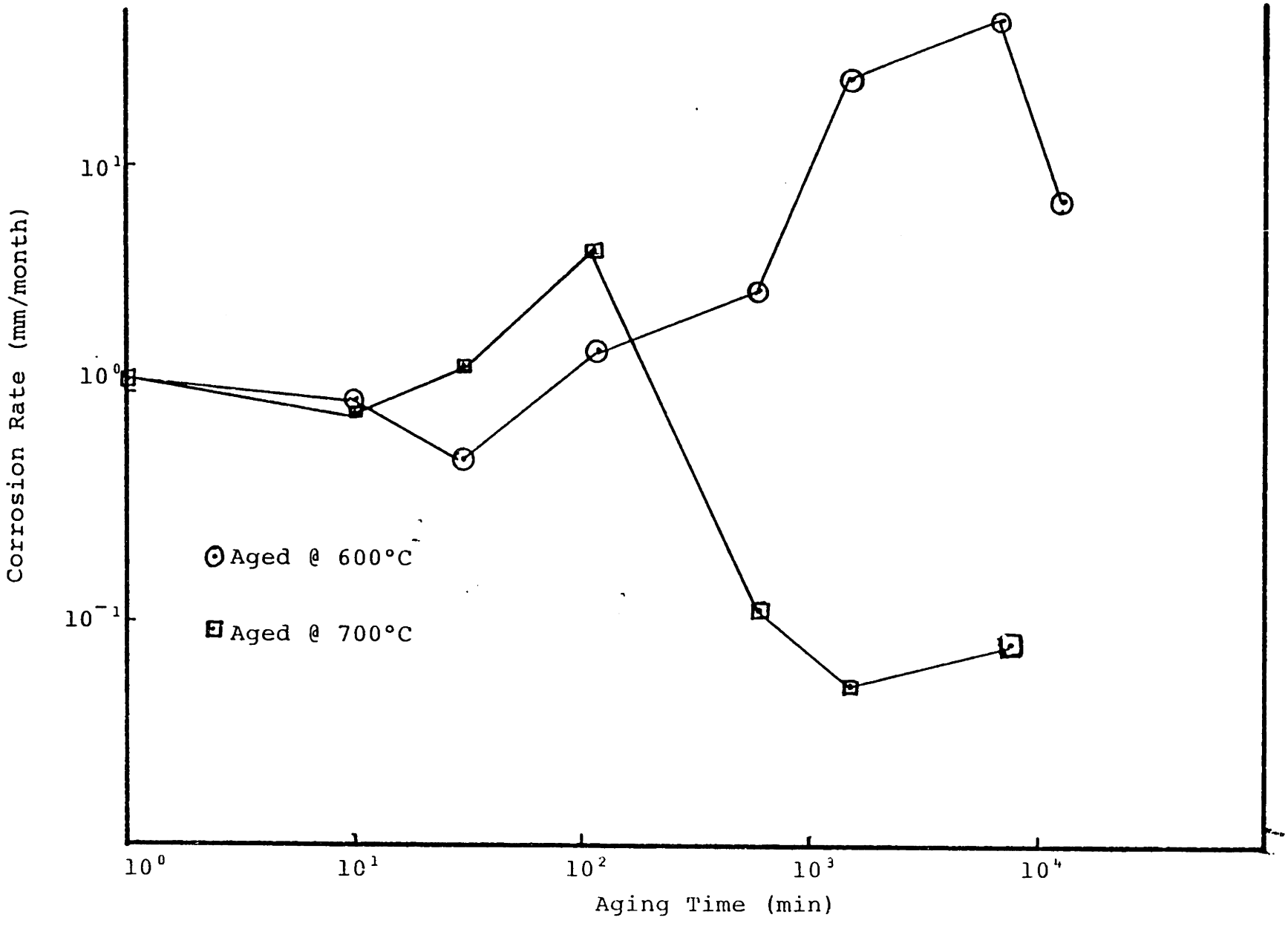

Figure 4.4 Corrosion Test Results for Alloy-600 Plate

Table 4.6

Streicher Test Results for the
Alloy-600 Plate Material

Aging Time (minutes)	Corrosion Rates (mm/month) Mill Annealed + Aged @600°C	Mill Annealed + Aged @700°C
0	1.067	1.067
10	0.889	0.787
30	0.508	1.295
120	1.575	4.06
600	2.870	0.102
1440	24.03	0.050
4320	-----	-----
7200	41.96	0.076
12960	6.833	-----

Table 4.7

Streicher Test Results for
Vendor Alloy-600 Tubing

Vendor	Corrosion Rate (mm/month)
Combustion Engineering	.10
Babcock & Wilcox	.10
Westinghouse Thermally Treated	.18
Westinghouse Mill Annealed	.30
Babcock & Wilcox Stress Relieved	76

5.0 Autoclave System Description

A very significant part of the overall program consisted of the design, construction, and operational checkout of the high pressure autoclave system used for the experimental program. As will be discussed later, the design of the system has a significant effect on the overall accuracy of the system. In this section a detailed description of the experimental system will be presented.

5.1 General Description

The high pressure autoclave system is composed of eight (8) subsystems. These subsystems are: (1) a high purity water distillation and demineralization system, (2) a solution storage and mixing system, (3) a chemical analysis system, (4) a high pressure pumping system, (5) a high pressure autoclave system, (6) a servohydraulic fatigue system, (7) a Crack Opening Displacement (COD) measurement system, and (8) a safety and control system. Figure 5.1 shows a simplified line diagram of the system. Table 5.1 shows the basic design parameters for the system.

The basic design of the system in terms of general layout and component design is patterned after a system in use at the General Electric Corporate Research and Development Center. However, the detailed design represents the amalgamation of what the author considered to be the best features of several systems which are in use at other laboratories, along with features unique to the system.

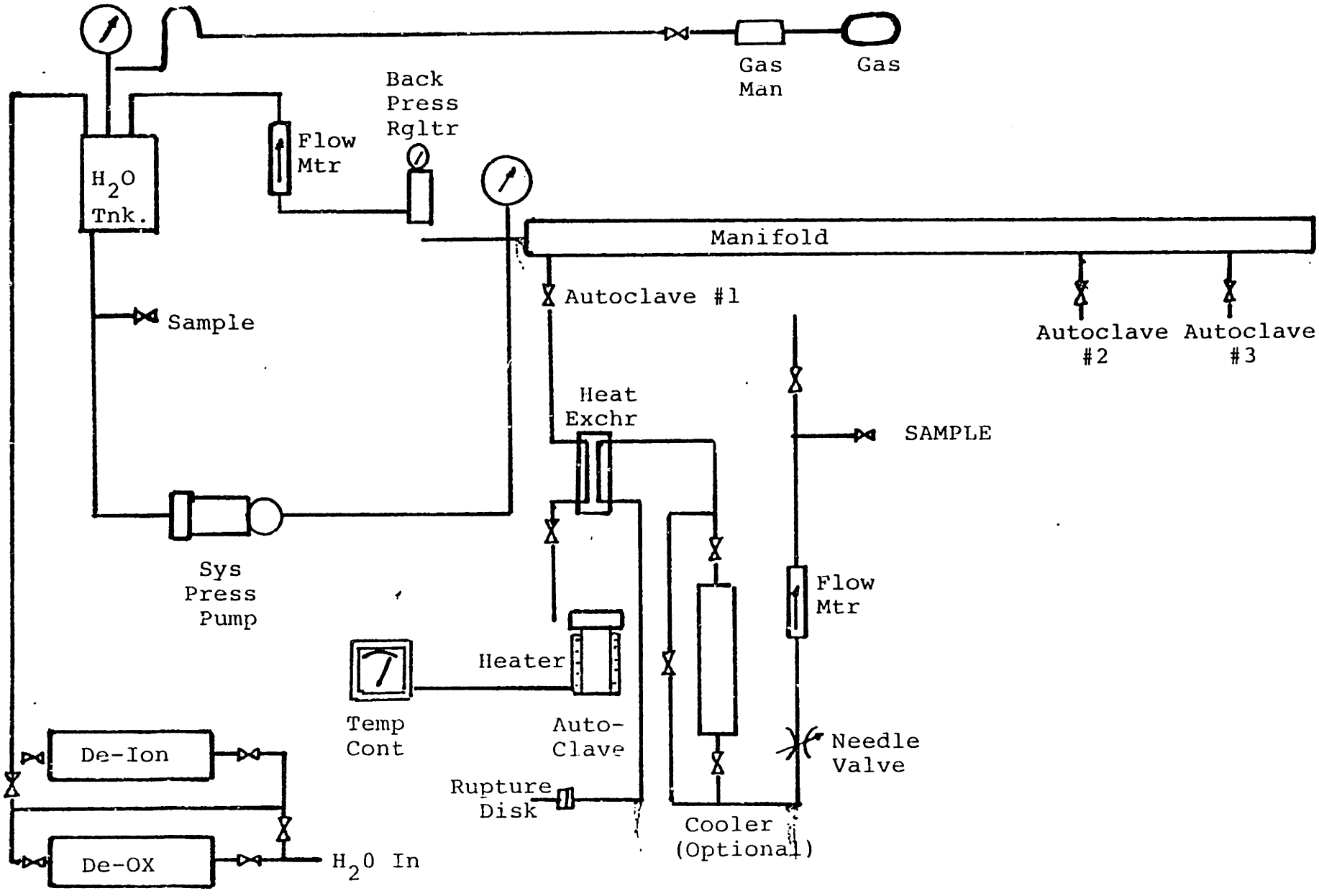

Figure 5.1 Simplified Line Diagram of the High Pressure Autoclave System

Table 5.1

Material of Construction	Titanium
Operating Pressure	10.34 MPa
Operating Temperature	290°C (Sat. Pres. 7.58 MPa)
Flow Rate/Autoclave	3.7 L/hr
Pump Relief	14.0 MPa
High Pressure Shutoff	13.79 MPa
Rupture Disk Setpoint	17.2 MPa
Low Pressure Shutoff	8.62 MPa (Sat. Temp. 300°C)
High Temperature Shutoff	305°C (Sat. Pres. 9.31 MPa)
Autoclave Proof Test	20.7 MPa

In particular, the construction of such a system in a university environment necessitated the incorporation of several safety related features.

The high pressure autoclave system is constructed entirely of titanium. The autoclaves are refreshed and the system is capable of supporting three (3) separate autoclaves. The flow rate through each autoclave can be up to 3.78 liters/hr. Each autoclave can either be operated separately, as a non-refreshed autoclave, or using the same solution supply system in the refreshed mode. One of the autoclaves is mounted in a servohydraulic fatigue machine. This autoclave uas the one used for this study. The following sections provide a description of each of the individual system subsystems.

5.2 High Purity Water Distillation and Demineralization System

This system consists of a 7.6 liter/hour electric distillation system, a four cartridge demineralization system, and a water storage system. The cartridge system consists of two mixed bed resin cartridges, an oxygen removal cartridge, and a submicron filter. The system is capable of providing water with a resistivity greater than 15 megohm-cm and an oxygen concentration less than 10 PPB. Oxygen level is maintained in the storage tank by bubbling high purity argon and continuous recycling through the cartridge system if necessary. The overall system is shown in Figure 5.2.

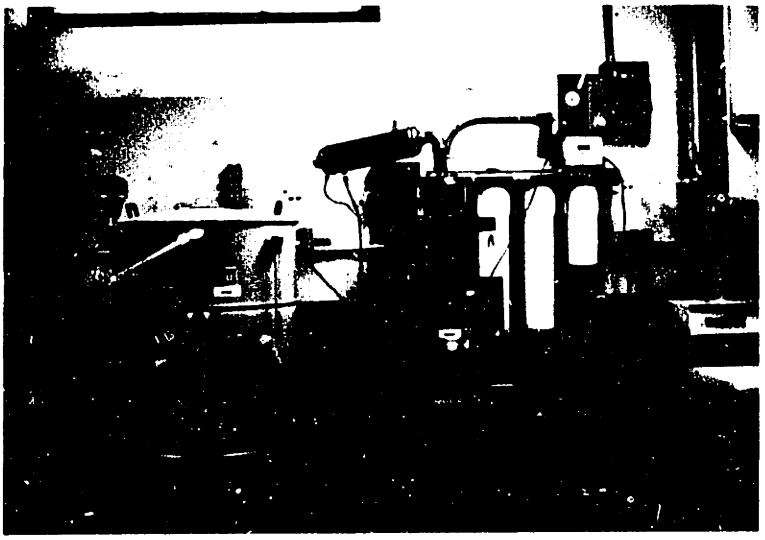

Figure 5.2 High Purity Water Distillation and Demineralization System

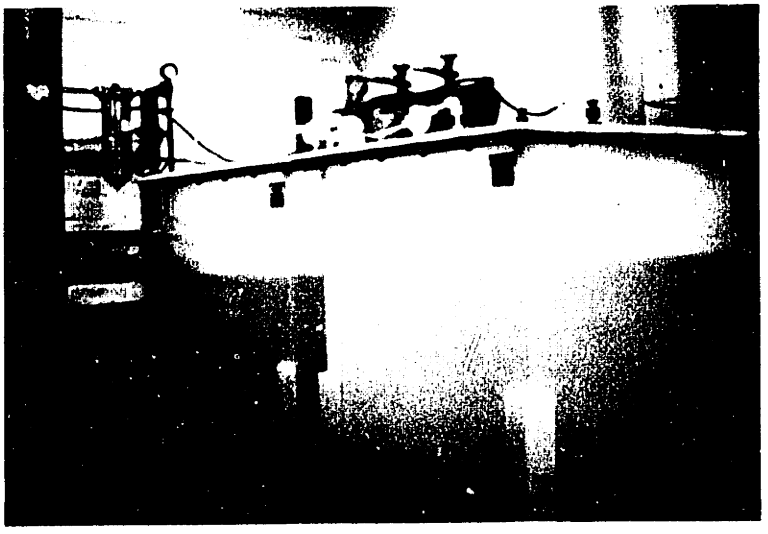

Figure 5.3 Solution Storage and Mixing System-Polypropylene Tanks

Figure 6. Solution Storage and Mixing System-Polypropylene Tanks

5.3 Solution Storage and Mixing System

The solution storage and mixing system consists of four storage tanks, two titanium and two polypropylene, and associated pumps, valves and piping for transferring solution from one tank to another. The two polypropylene tanks are used when oxygen control is not necessary and if a highly corrosive solution is being used. The titanium tanks are used for tests requiring high purity water or oxidizing solutions. Oxygen control is maintained in the titanium tanks by bubbling high purity argon and/or recirculation through the demineralization cartridges. Oxygen levels of less than 10 PPB are capable with this storage system. The overall system is shown in Figures 5.3 and 5.4.

5.4 Chemical Analysis System

The chemical analysis system consists of a conductivity measuring system, a pH measuring system, and an oxygen measuring system incorporated into a portable rack, The system can be attached to the autoclave system at one of several points for solution analysis. During testing the system is normally attached to the effluent of the autoclave and provides a continuous record of the system chemistry. In addition to the portable system, independent measurement of oxygen, pH and conductivity can be made using a simple color comparator type of test for oxygen and separate laboratory instruments for pH and conductivity. The overall system is shown in Figure 5.5.

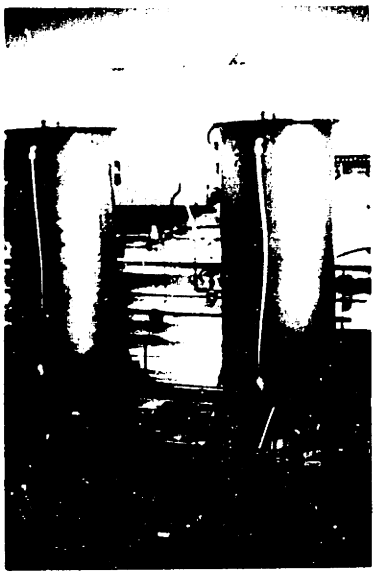

Figure 5.4 Solution Storage and Mixing System-Titanium Tanks

Figure 5.5 Chemical Analysis System

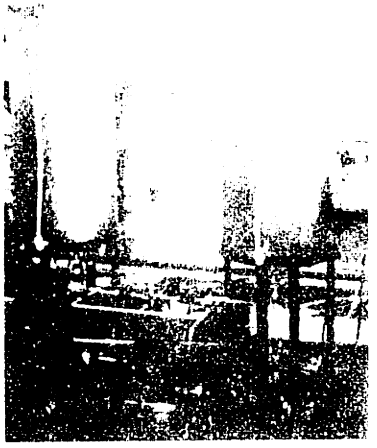

5.5 High Pressure Pumping System

The high pressure pumping system supplies solution at the required system pressure to the three autoclaves in the system. The systems major components are: (1) a booster pump, (2) a high pressure pump, (3) a back pressure regulator for pressure control, (4) associated piping and valves, and (5) a pulsation damper.

The booster pump is a positive displacement gear pump which supplies solution at the required pressure from the storage system to the suction of the high pressure pump. Solution that is not used is recirculated back to the storage system, thus insuring a fresh supply of solution to the high pressure pump at all times.

The high pressure pump is a positive displacement diaphragm pump with an adjustable output from 0-18 l/hr. The pump is capable of operating at pressures up to 13.8 MPa with the pump internal relief set at 14 MPa.

System pressure is controlled by a back pressure regulator on the discharge of the high pressure pump. The back pressure regulator is of the diaphragm type with pressure on the primary side of the diaphragm being regulated by the pressure of a gas supplied to the secondary side. For this system the source of gas is a high pressure nitrogen manifold which services the entire system. Pressure is regulated by partial bypass of the output of the high pressure pump back to the storage system.

System pressure fluctuations, due to the nature of the

pumping system, are minimized by the use of a bellows type pulsation damper installed on the high pressure pump discharge. During operation, system pressure is present on one side of the titanium bellows. The secondary side of the bellows is pressurized with nitrogen at the same pressure. The differences in compressibility between the solution and the nitrogen results in a dampening of the pump pressure pulsations. The gas for the secondary side of the bellows is supplied from the same source as that for the secondary side of the back pressure regulator, thus insuring that the pressure differential across the bellows is not too great.

Flow control through each of the autoclaves is regulated by needle valves located at the outlet of each vessel. These valves supply the pressure drop at the outlet of each vessel. Solution from each vessel can be either sent to drain or returned to the solution storage system. System flow is monitored by flow meters on the outlet of each vessel, downstream of the throttle valves, and a flow meter in the return from the back pressure regulator. A high pressure filter on the exit from each vessel allows the filtration of the effluent for analysis, if desired. Figures 5.6 - 5.8 show various views of the high pressure pumping system.

5.6 High Pressure Autoclave System

The high pressure autoclave system consists of three 3.78 liter titanium vessels and associated piping. One of the autoclaves is mounted in a servohydraulic fatigue ma-

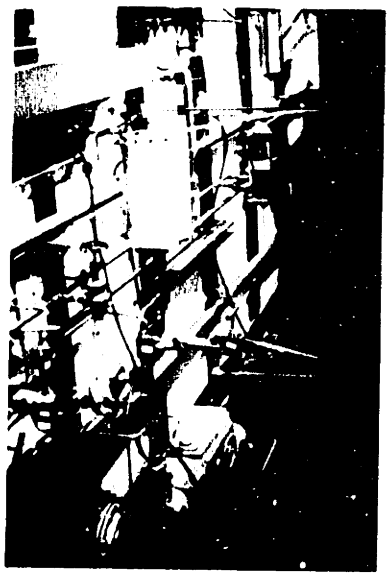

Figure 5.6 Autoclave System High Pressure Pump

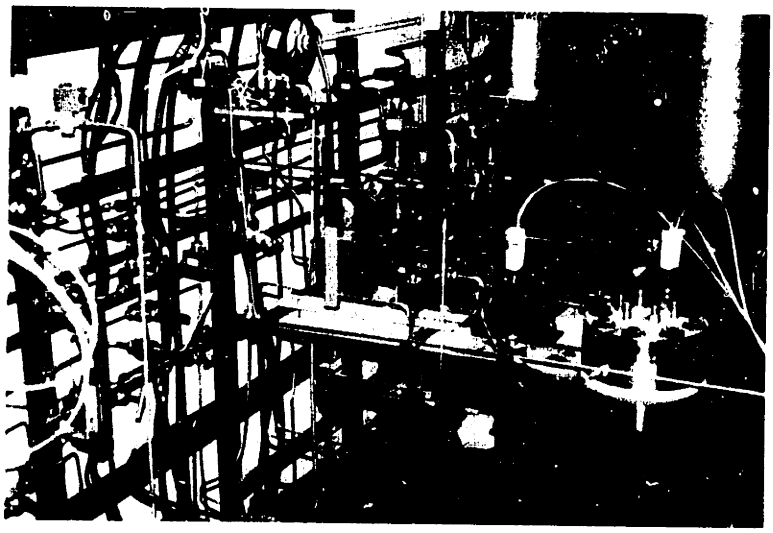

Figure 5.7 Autoclave System Back Pressure Regulator and Pulsation Damper

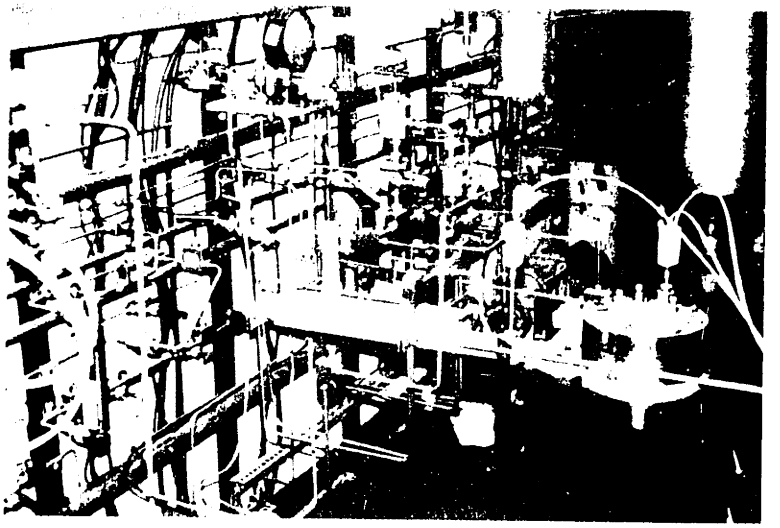

Figure 5.7 Autoclave System Back Pressure Regulator and Pulsation Damper

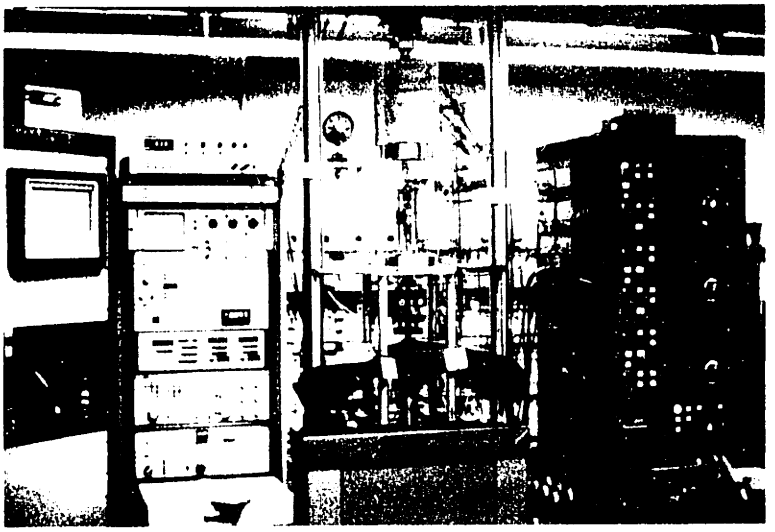

Figure 5.8 Autoclave System Piping System

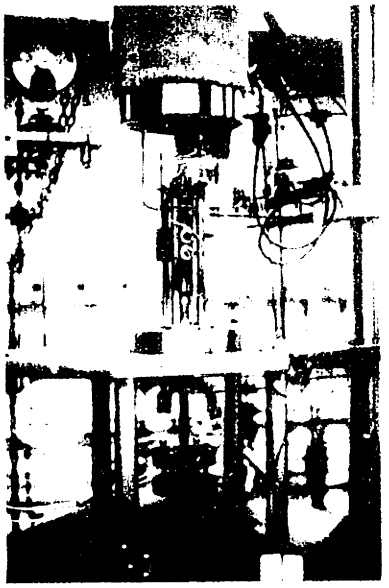

Figure 5.9 Autoclave Installed in Fatigue Machine

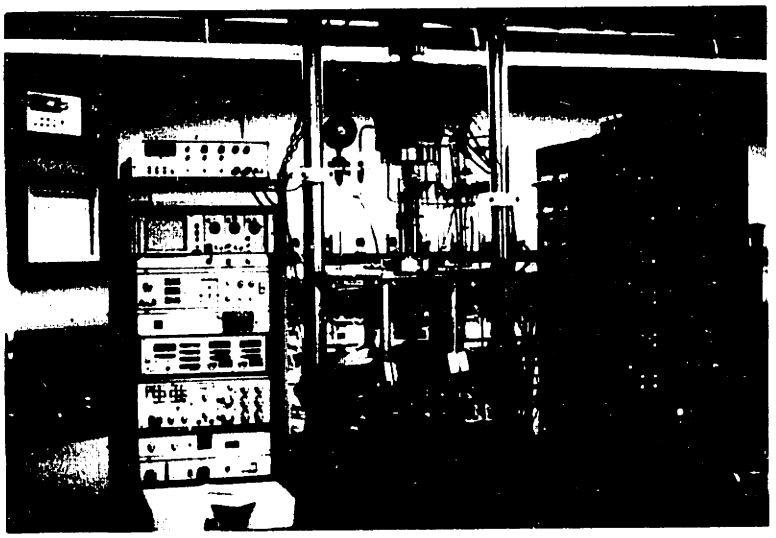

Figure 5.8 Autoclave System Piping System

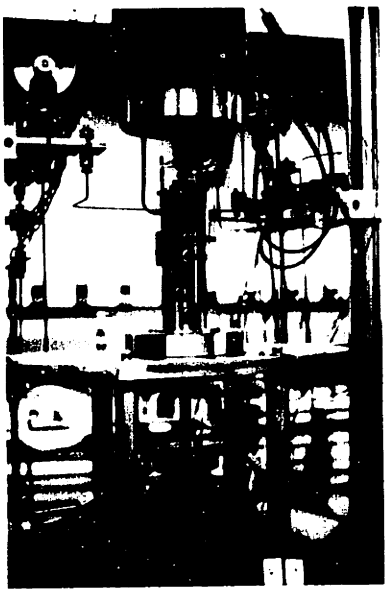

Figure 5.9 Autoclave Installed in Fatigue Machine

chine system for use in fatigue crack growth studies. The other two are mounted in frames and are intended for use in stress corrosion cracking or other corrosion related experiments. Figures 5.9 and 5.10 show the autoclaves used in the fatigue machine and for non-fatigue related studies, respectively.

Solution is supplied to each autoclave through a regenerative heat exchanger. Incoming solution is heated by the effluent solution. This technique minimizes the required external heat input. Effluent solution is further cooled as necessary by a non-regenerative heat exchanger located down stream of the regenerative heat exchanger. Solution enters the bottom of the autoclaves and exits the top.

System heat is supplied by a three zone heater and controller. The heater is located external to the autoclave. Temperature regulation and control is achieved through the use of multiple thermocouples. For temperature regulation, two thermocouples hooked in parallel are used. One of the thermocouples is located in the autoclave at the specimen level, the other is located between the heater and the outside wall of the autoclave. With the two thermocouples connected in parallel, the average temperature between the solution at the specimen level and the heater outside the autoclave is controlled. Specimen temperature is measured independently and the temperature controller adjusted to achieve the desired specimen temperature. The above control technique is necessary due to the high thermal inertia of

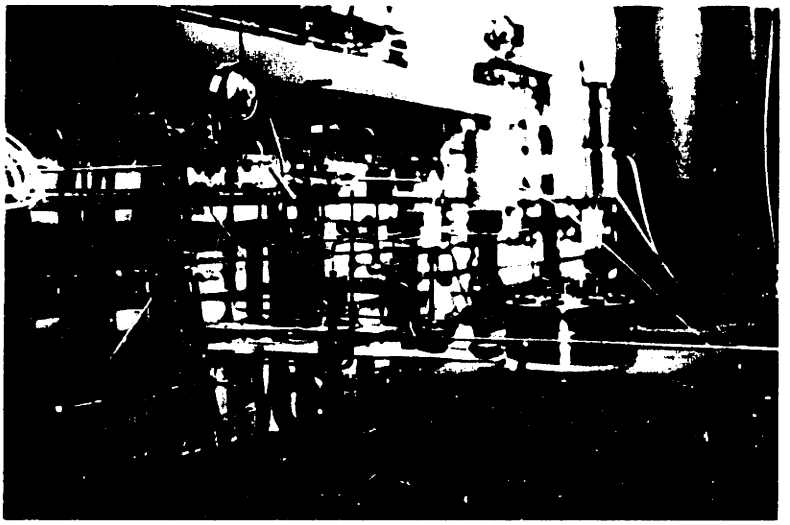

Figure 5.10 Autoclave Mounted for Use in SCC Experiments

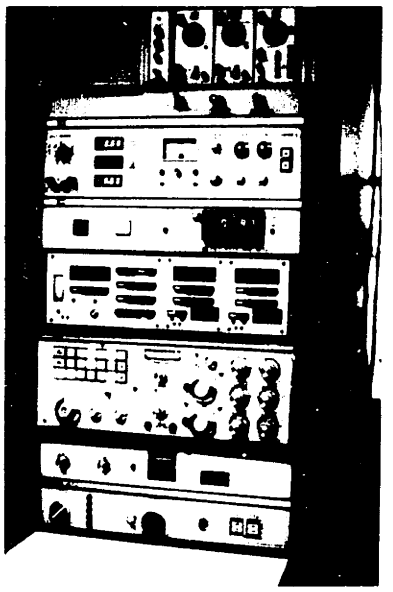

Figure 5.11 Fatigue Machine Control System

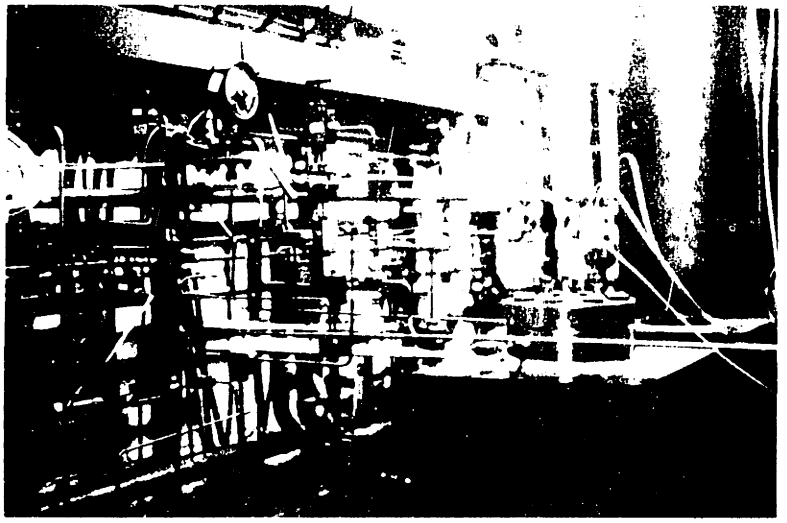

Figure 5.10 Autoclave Mounted for Use in SCC Experiments

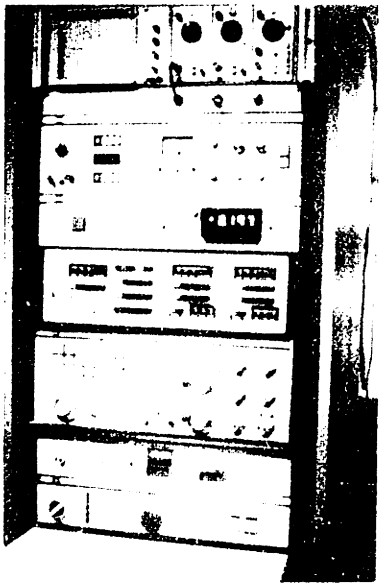

Figure 5.11 Fatigue Machine Control System

the system and the long time constant of the system. By using this technique specimen temperature variations of less than 1°C are achieved.

In addition to the temperature control thermocouples, three other thermocouples are installed in each autoclave, two for temperature distribution monitoring and one for temerature limiting. The two monitoring thermocouples are located in the center of the lower and upper third of the autoclave respectively. These two thermocouples along with the specimen thermocouple provide the ability to monitor temperature gradients within the autoclave. The temperature limiting thermocouple is used to limit the peak solution temperature to a level below the saturation temperature for the operating pressure and is connected to an independent controller located in series with the heater supply from the main temperature controller.

Autoclave system pressure is monitored by a pressure gauge attached to and non-isolable from each autoclave. Maximum pressure is limited by rupture disks set at 17.2 MPa. The ruptive disk relief path is from the autoclave through the non-regenerative heat exchanger to a drain, thus insuring against the hazard of a steam leak.

5.7 Servohydraulic Fatigue System

The servohydraulic fatigue system consists of a closed loop servohydraulic fatigue machine with associated controls and a specimen loading system. Figures 5.11 and 5.12 show

the fatigue machine with the autoclave mounted in the load frame. The loading system has an upper load capability of 89 kilonewtons and a maximum cyclic frequency of 5 Hz when used with the autoclave system.

The specimen loading system, pictured in Figure 5.13 and illustrated in line form in Figure 5.14, provides for electrical insulation of the specimen from the loading system. The loading system consists of: (1) a lower pull rod and grip, (2) an upper pull rod and grip, and (3) a reaction cage. The autoclave is mounted upside down on a specially designed load frame (see Figure 5.12) with the lower pull rod entering the autoclave through a teflon seal in the autoclave head. All other penetrations into the autoclave are also through the head, which is mounted upside down on the loading frame. The upper pull rod is suspended from a reaction cage which is comprised of four rods and an upper plate (see Figure 5.14). The suspension mechanism for the upper pull rod will not support a compressive force, thus preventing the specimen load from going compressive during a test. The use of a reaction cage design for specimen loading allows the elimination of the upper pull rod penetration into the autoclave. With this penetration eliminated, the accessibility of the specimen is greatly improved since the autoclave body can be removed without disturbing the loading train.

Specimen isolation is achieved through a system of ceramic sleeves and washers, illustrated by Figure 5.15, in

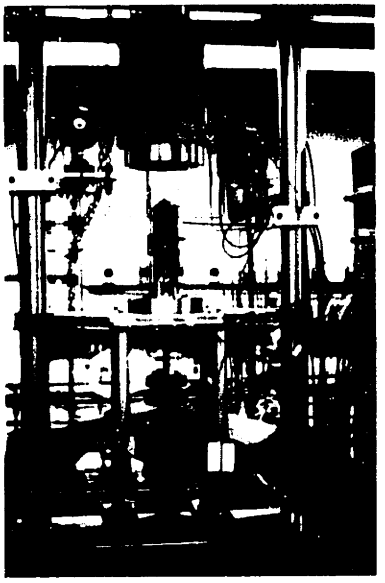

Figure 5.12 Fatigue Machine Load Frame with Autoclave Installed

Figure 5.13 Specimen Loading System

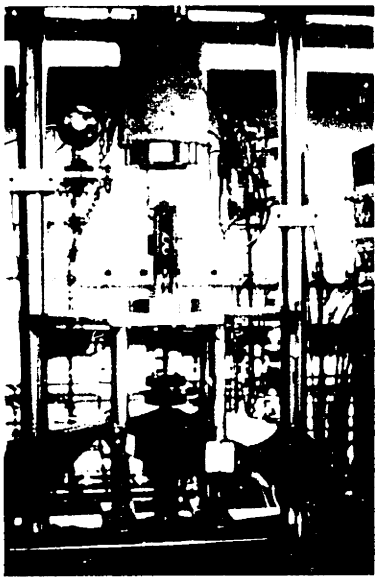

Figure 5.12 Fatigue Machine Load Frame with Autoclave Installed

Figure 5.13 Specimen Loading System

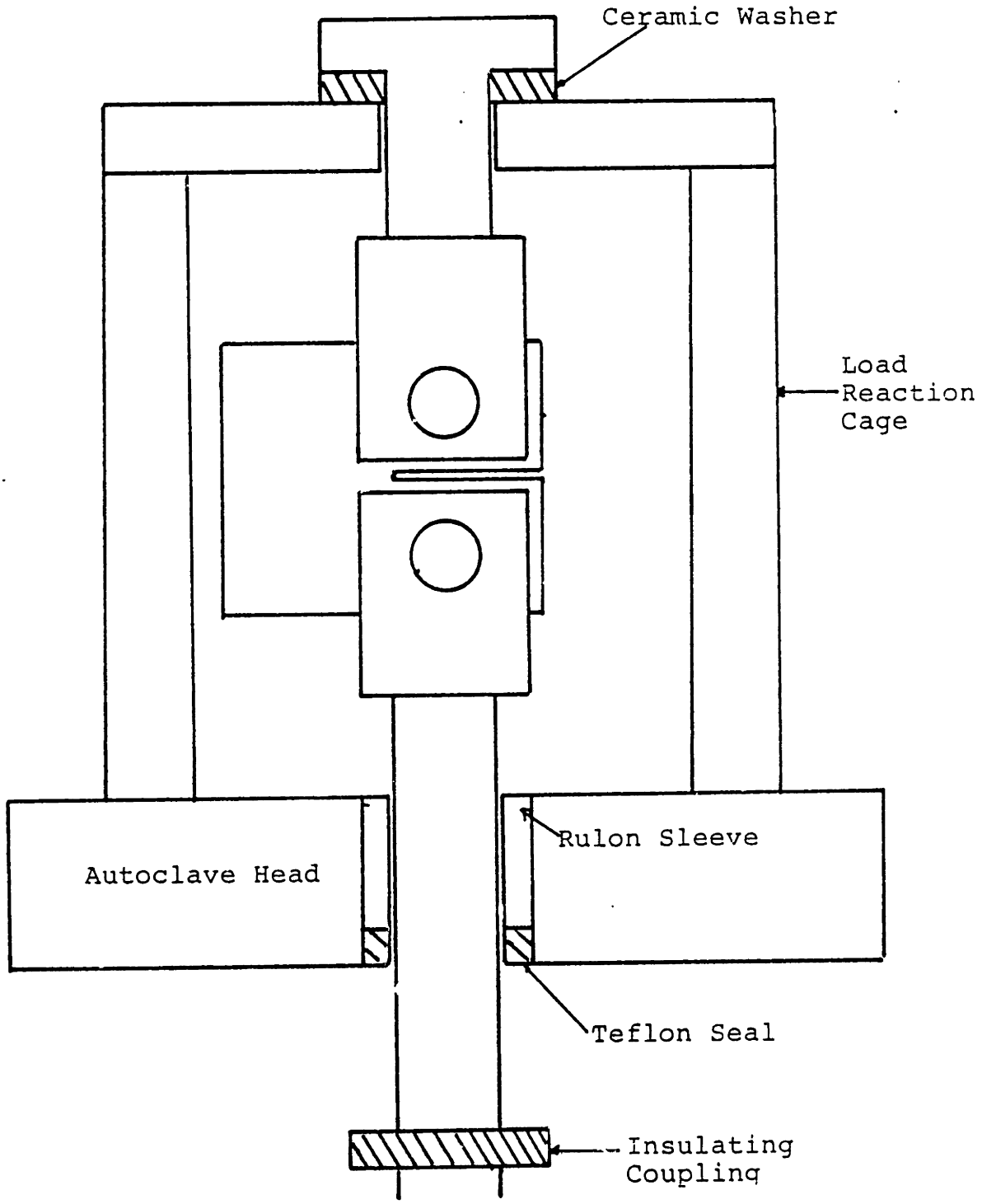

Figure 5.14 Specimen Loading System-Line Diagram

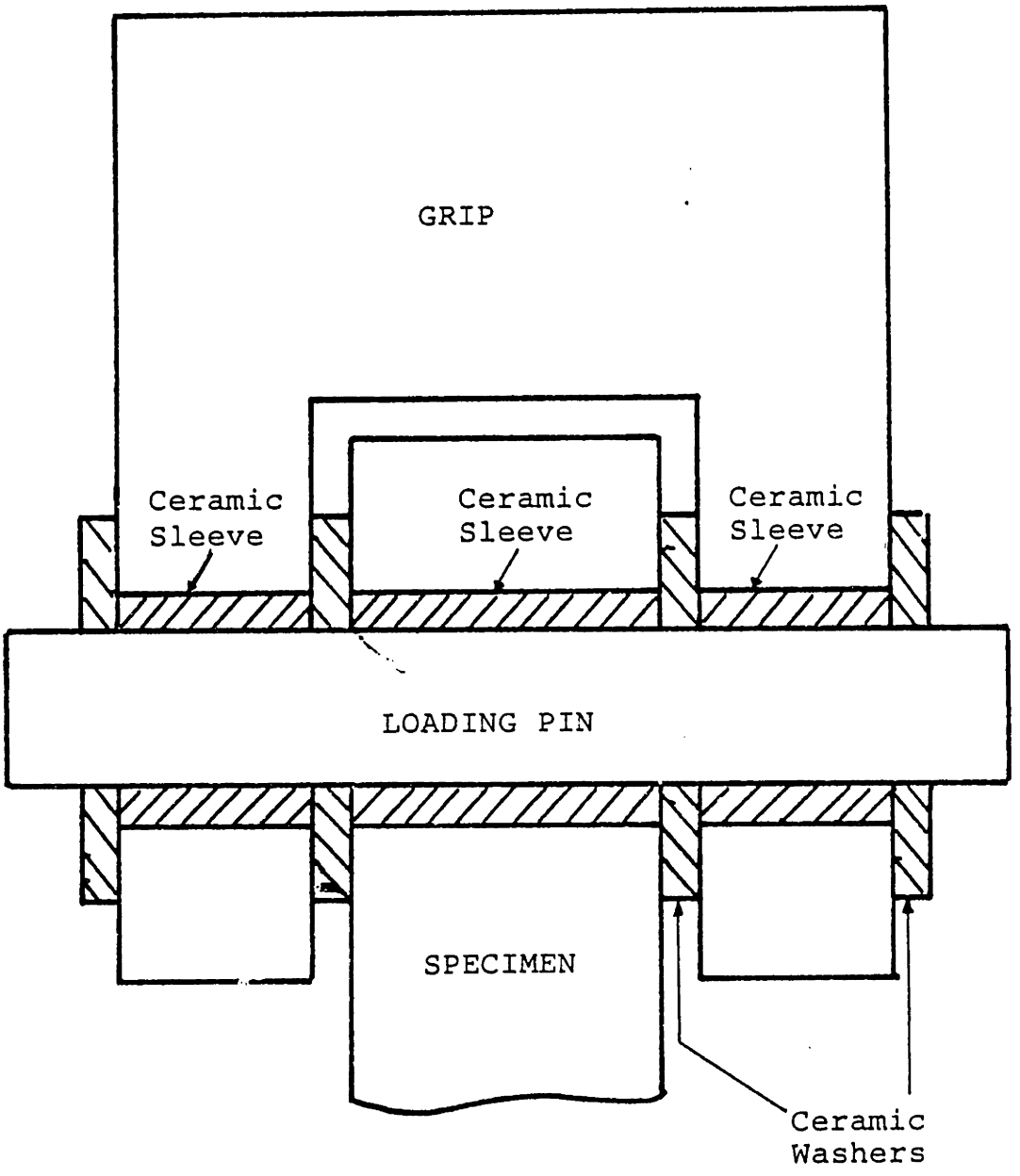

Figure 5.15 Specimen Isolation System

conjunction with an isolating coupling located on the lower pull rod external to the autoclave. The specimen is isolated from the loading grips through the use of ceramic sleeves on the loading pins and ceramic washers on the pins between the specimen sides and the grips. Further isolation is achieved by suspending the upper pull rod from a ceramic washer and the use of the lower pull rod insulating coupling. The teflon seal provides electrical insulation of the lower pull rod from the autoclave head at the feed through point. The accuracy of the machining of the ceramic insulators was found to be critical to the overall durability of the isolation system.

5.8 Crack Opening Displacement Measuring System

The accurate measurement of crack opening displacement (COD) is central to the determination of fatigue crack growth rates by the compliance technique used for this study and will be discussed in detail later. Because of the critical nature of this measurement, it was decided to measure COD by attaching a measuring device directly to the specimen in the envirnoment. The device chosed was a Shaevitz Model 100XS-ZTR high temperature linear variable differential transformer (LVDT). The linear displacement range of this device is 2.54 mm. The precision of the LVDT was determined in situ and is discussed in section 6.0.

In practice the LVDT is attached directly to the specimen front fact using a special mounting device. The mount-

ing device is insulated from the specimen as illustrated by the line diagram in Figure 5.16. Mounting screws are made from the same material as the specimens. The LVDT was not obtainable with a titanium case, so the entire device was gold plated. Figure 5.17 shows a picture of the LVDT mounted in the system.

5.9 Safety and Control System

The insurance of safety, both in terms of system as well as personal protection was a primary consideration in the design of the autoclave system. Safety personnel from the Institute were consulted throughout the entire design and construction process. The purpose of the safety system is three fold: (1) protection of laboratory personnel from high temperature steam and corrosive substances in the event of a system failure, (2) the protection of laboratory and other personnel from high velocity objects in the event of a system failure, and (3) the protection of the system itself in the event of a fault in a single component or the loss of electrical power.

Laboratory personnel protection is achieved through the use of carefully thought out design and the judicious use of shielding. Laboratory personnel are separated from almost all of the high pressure piping by placing other equipment between operating personnel and high pressure piping. In addition, the amount of high temperature, high pressure piping is minimized and located only in the imme-

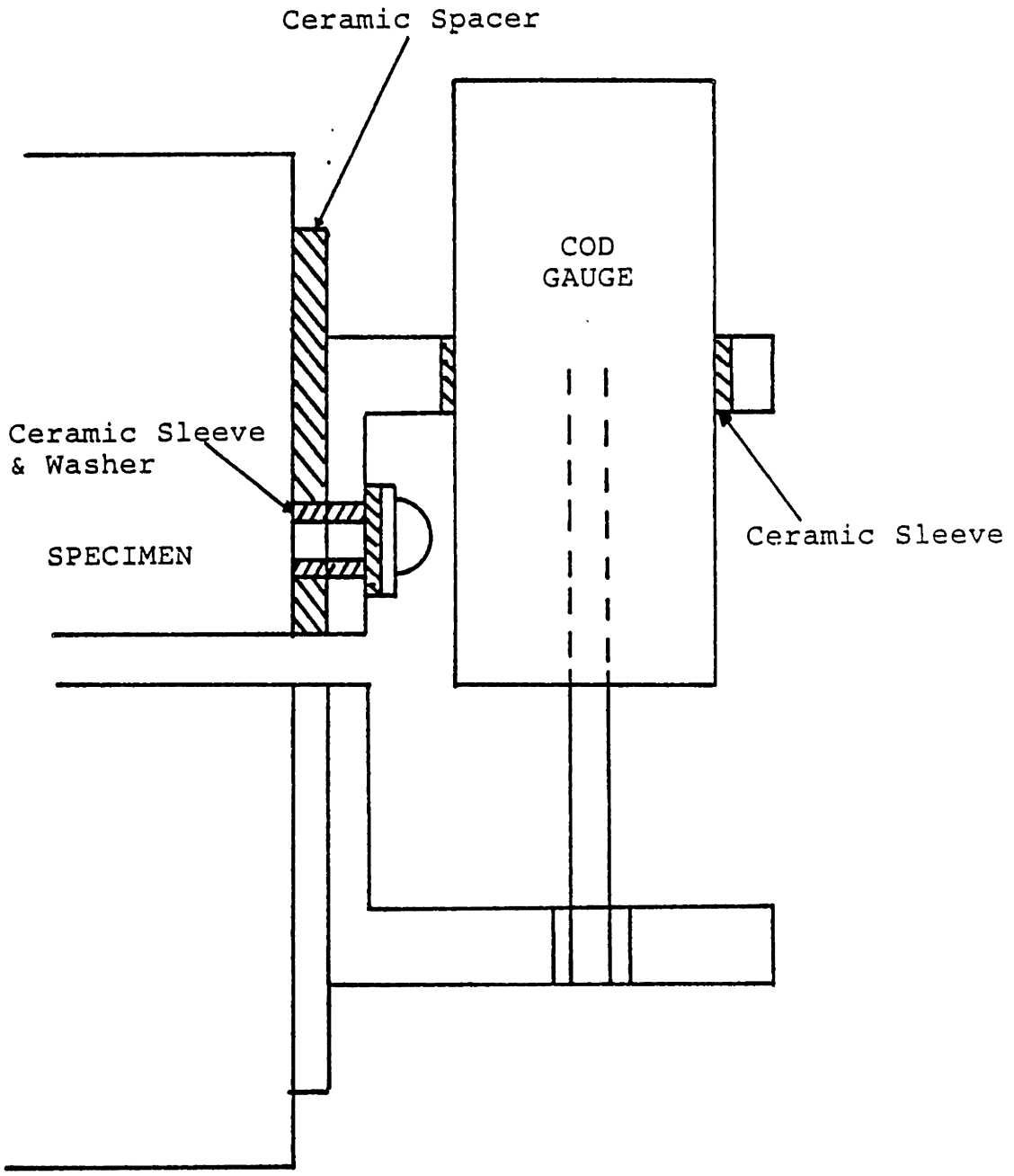

Figure 5.16 Crack Opening Displacement Mounting System-Line Diagram

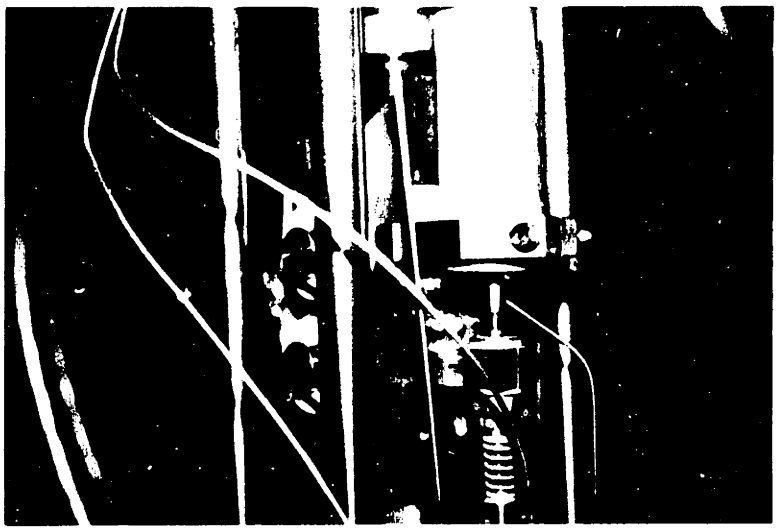

Figure 5.17 COD Gauge Mounted to Specimen

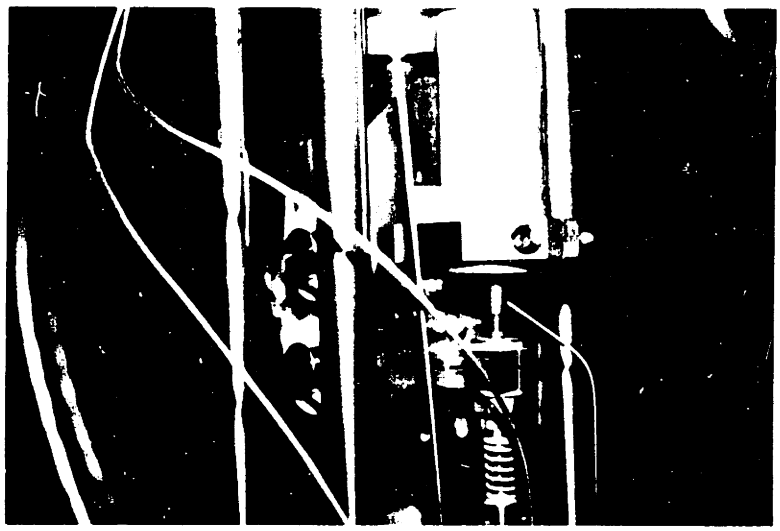

Figure 5.17 COD Gauge Mounted to Specimen

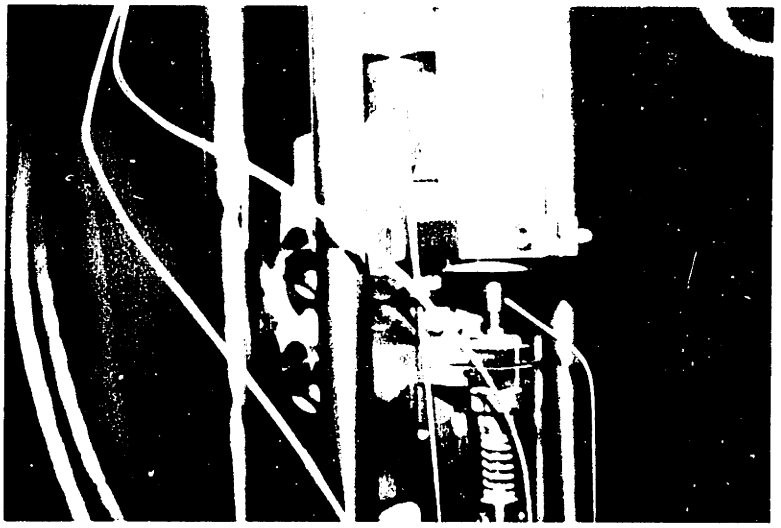

Figure 5.17 COD Gauge Mounted to Specimen

diate vicinity of the autoclaves. Laboratory personnel operate the system from the front while all potentially dangerous piping is routed behind. Protection from an autoclave failure is achieved through the use of shielding around the autoclave during operation.

Additional protection for non-laboratory personnel is provided through laboratory modifications to preclude accidental laboratory entry and to inhibit high velocity object egress. Access is controlled through the use of a staircase from above the laboratory and the elimination of entrances from outside hallways. Shielding has been provided for all doors and windows in the laboratory.

The autoclave system itself is protected by an extensive safety system. Protection is provided against the following events: (1) system overpressure, (2) system high temperature, (3) system low temperature, (4) excessive pulsation damper bellows differential pressure, (5) loss of system electrical power, (6) excessive specimen load, and (7) excessive load train displacement.

System over pressure is protected against in four independent ways. First, the high pressure pump has an internal relief valve set at 12.4 MPa; second, a pressure switch on the discharge of the high pressure pump is set to shut the pump off at 13.8 MPa; third, each autoclave has a pressure switch incorporated into its pressure gauge which will denergize the external heater at 13.8 MPa; and fourth, each autoclave is protected by its own rupture disk which

is set at 17.2 MPa. Relief valves and rupture disks cannot be isolated.

System high temperature is protected against in two ways: (1) each controller is designed to turn itself off if a thermocouple becomes open, and (2) each autoclave heater will be shut off independently if the temperature exceeds 305°C or the system pressure exceeds 13.8 MPa.

System low pressure protection is necessary to prevent the solution from flashing to steam. Accordingly, pressure switches on each autoclave are set to shut off the external heater is the system pressure goes below 9.6 MPa.

The titanium bellows which is part of the high pressure pump pulsation damper is custom made and expensive. If the pressure differential across the bellows exceeds approximately 0.5 MPa, rupture is likely to occur. To prevent this occurance an air operated valve is present in the solution side line to the device. The valve is actuated by a pressure switch at the high pressure pump discharge and is set to isolate the pulsation damper if the system pressure decreases to 0.5 MPa below the gas side pressure. The isolation valve is also designed to fail shut upon loss of laboratory power.

In the event of a loss of laboratory power, the entire system is designed to shut itself down automatically and not restart unless operator action is taken, upon the restoration of power. Automatic shut down is achieved through the use of air operated valves which fail shut upon loss of power. These valves act to prevent immediate depressurization of

the system and the flashing of the solution to steam. Instead, the system is allowed to cool down slowly at pressure. Safety relays prevent restoration of power to control circuits when power is restored.

Excessive load or displacement is protected against by electrical interlocks which are part of the fatigue machine control circuits. Limits on displacement and load can be set to shut off the fatigue machine if an alarm condition exists. In addition, mechanical stops have been installed in the load frame which are capable of physically preventing abnormally large actuator motion.

Figure 5.18 shows the control panel for the safety and control system.

6.0 Experimental Procedures and Analytical Methods

6.1 Introduction

As discussed earlier, the ultimate goal of the research program was to obtain fatigue crack growth data for Alloy-600 in high purity water at 288°C, as a function of thermal treatment. However, this final result is the last step in a process involving many coupled steps. Each one of these steps is accomplished with more or less difficulty and each step contributes a certain amount of noise to the analysis. The extraction of meaningful information from the data is not a trivial task when working under these conditions and great care must be taken not to derive more meaning from the data than is justified.

As the experimental program developed and the overall system was designed, built and checked out, it became apparent that a detailed error or uncertainty analysis would be necessary in order that the expected degree of confidence on the da/dn vs ΔK be established. A complete uncertainty analysis of the overall system was conducted and represents the first such attempt for this type of experimental investigation. In this section the experimental techniques used in the program will be discussed. From this discussion we will proceed with a detailed description of each step in the analysis. The section will conclude with a detailed description and discussion of the error analysis and specific restrictions due to the use of linear elastic fracture mechanics in describing the results.

6.2 General Experimental Procedures

The measurement of fatigue crack growth rates in an autoclave system, such as the one used for this program, must be accomplished using indirect methods. The direct physical measurement of crack length is not possible, making it necessary to infer crack length through the measurement of some other parameter. The two most popular methods of infering crack length are measuring the electrical potential drop across the section of the specimen which contains the moving crack and the measurement of the elastic compliance of the uncracked specimen ligament. Both of these techniques have their own unique problems with the end result that the overall accuracy of the two techniques are comparable. For this program the compliance technique for the measurement of crack length was chosen due to its relative simplicity and the fact that the measured parameters, load and displacement, were considered of a more fundamental nature and more easily measured, at least in principal.

The general procedure for the determination of fatigue crack growth rates consists of the following basic steps: (1) measure specimen elastic compliance vs number of fatigue cycles, (2) convert this data into crack length vs number of fatigue cycles using an appropriate correlation between elastic compliance and crack length, (3) establish the stress intensity factor for each compliance measurement using an appropriate correlation between crack length, load, and specimen characteristics, (4) differentiate the crack length vs number of cycles data to derive a value of da, the increment in crack length, for a given increment in dn, the

number of fatigue cycles, (5) combine the da/dn data with the computed values of the stress intensity factor range, ΔK, to obtain an estimate of the dependence of fatigue crack growth rate on the stress intensity factor range.

The final result, as one can see, is heavily dependent on each of the preceeding steps with the first step being the most critical. Also, the processing of the raw data necessitates the sequential use of several empirical correlations and the application of some form of numerical analysis in the differentiation step. The upshot of this is that errors introduced at one point in the analysis are likely to influence all subsequent calculations. This fact highlights the necessity for establishing an estimate of the overall confidence that can be placed on the final results. In the following sections we will discuss in detail each of the above mentioned steps.

6.3 The Compliance Method of Measuring Crack Length

The use of elastic compliance for the measurement of crack length has an advantage in that its calculation requires the measurement of only two fundamental quantities, load and displacement. Once these quantities have been determined, the elastic compliance can be determined using the following relationship:

$$C = BE \frac{dv}{dp} \qquad 6.0$$

where

C is the normalized elastic compliance

B is the specimen thickness

E is the material elastic modulus

$\frac{dv}{dp}$ is the slope of the crack mouth opening displacement vs load curve

Once the compliance is calculated, the crack length can be determined through the use of an experimentally derived correlation between crack length and compliance or one of several theoretically derived correlations available in the literature [14,15].

Theoretical relationships between crack length and compliance have been derived for several crack mouth opening displacement measurement locations. [14] Figure 6.1 shows a typical compliance vs crack length relationship. In general, experimental and theoretical compliance vs crack lengths agree quite well, usually within one percent when the experimental calibration curve is derived under carefully controlled conditions. Also, when conditions are carefully controlled, both load and crack mouth opening displacement can be measured with sufficient accuracy to allow acceptable accuracy in the prediction of crack length. However, when compliance measurements are made under actual experimental conditions, the potential for error increases significantly. The source of this error, as will be discussed later, lies in a substantial degradation in the precision of displacement measurement.

6.4 Specimen Design and Compliance Calibration

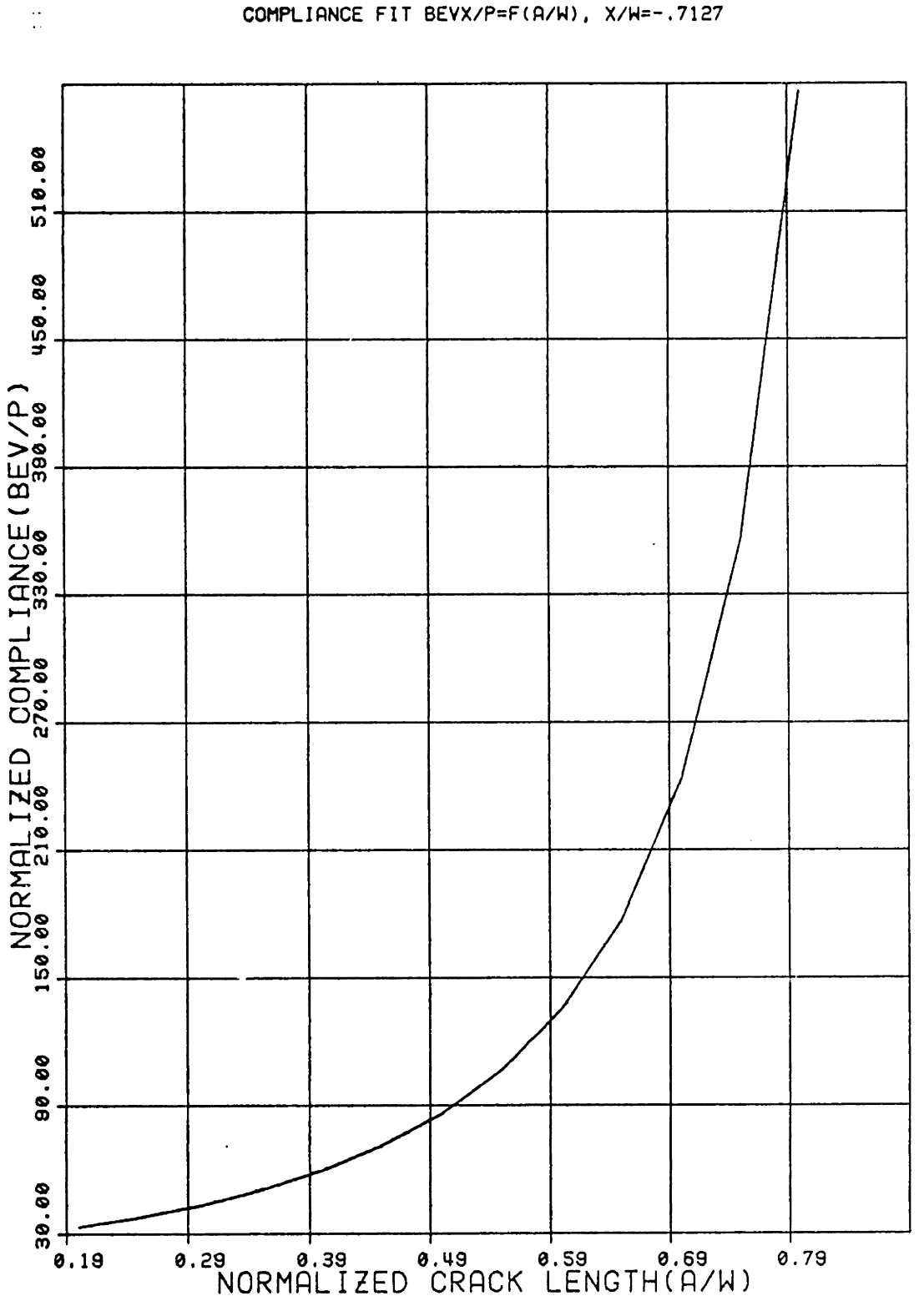

Figure 6.1 Typical Compliance vs Crack Length Relationship

Figure 6.2 shows the specimen geometry used in the experimental program. The specimen type is of the compact tension (CT) design with dimensions conforming to the recommendations of ASTM E647-78T, "Tentative Test Method for Constant-Load-Amplitude Fatigue Crack Growth Rates Above 10^{-8} m/cycle". The specimen width (W) is 50.8 cm and thickness (B) is 12.7 cm. Electrical isolation of the specimen from the loading system necessitated the following deviations from the recommended design:

(1) Specimen pin holes were enlarged from 1.27 cm to 1.524 cm in diameter to allow the insertion of a ceramic bushing between the loading pin and the specimen.

(2) Ceramic washers were used to insure that the sample sides did not contact the grips at any time.

(3) The COD gauge was insulated from the specimen through the use of ceramic standoffs.

As pointed out earlier, theoretical compliance vs crack length relationships exist in the literature for several specimen designs, including the general design used in this program. However, the specimen modifications mentioned above and the unique measurement point locations for COD required that a set of compliance calibrations be derived for our particular design. The compliance calibration process consisted of three areas of analysis: (1) an investigation of the potential effect of the ceramic insulating sleeve around

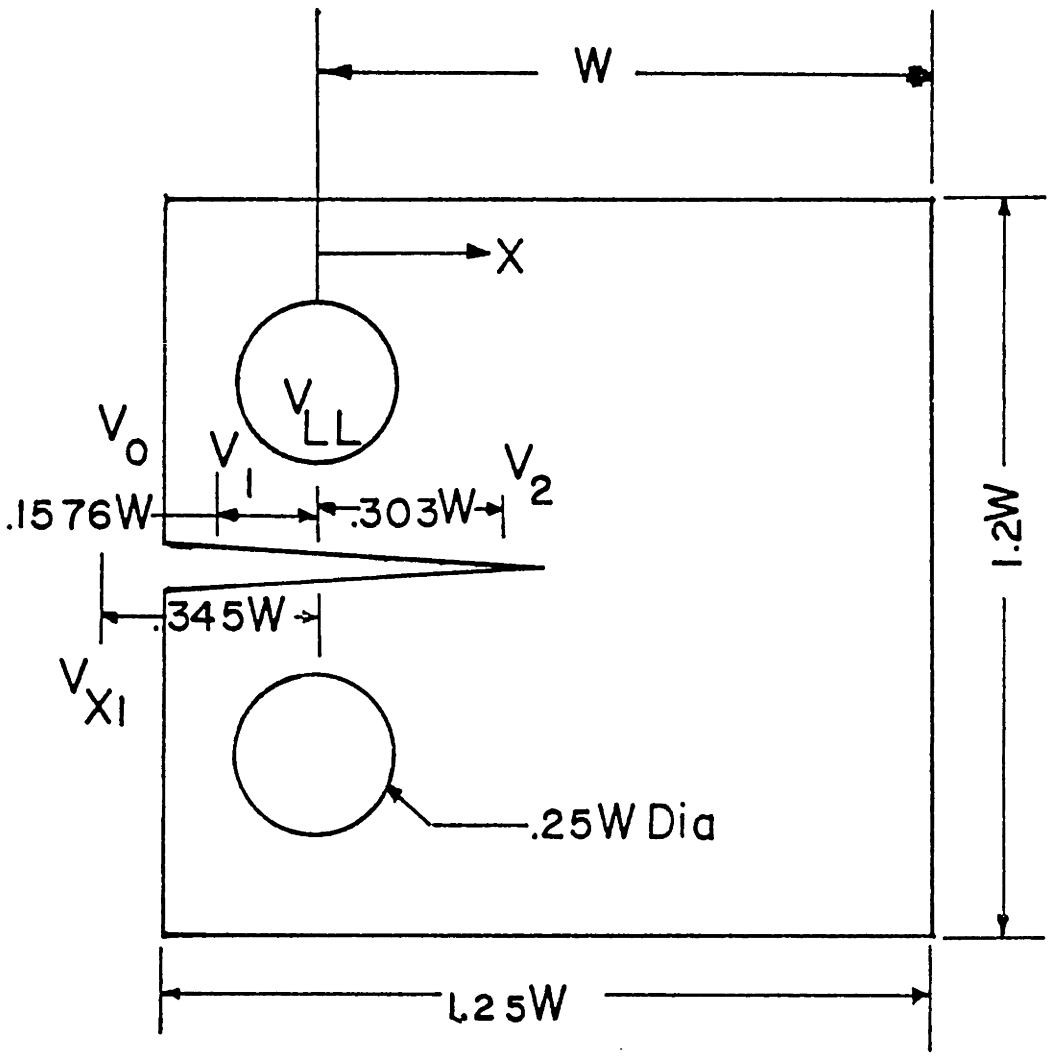

Figure 6.2 Fatigue Crack Growth Specimen Dimensions.

Figure 6.4 Compact Tension Specimen Showing Compliance Measurement Point Locations

the loading pins, (2) the derivation of theoretical compliance vs crack length relationships for our specific COD measurement locations, and (3) the actual experimental confirmation of the theoretically derived compliance calibration.

6.4.1 The Effect of Pin Loading Geometry

The crack opening displacement for a given nominal specimen load depends on the stress distribution around the crack tip and indeed throughout the entire specimen. The load is transferred from the load train to the specimen by the specimen pins and this laod transfer provides the source of the stress distribution within the specimen. Newman [16] has investigated the effect of pin loading on crack opening displacement for the general compact specimen design used in this program. He found that the COD, measured at the load line (point L in Figure 6.2) was a function both of the location of the loading holes and the type of fit for the loading pins. Figure 6.3 and Table 6.1 show data from Newman's paper showing the effect of pin fit on measured compliance. The normalized complienace values listed in Table 6.1 and illustrated in Figure 6.3 are for pins which meet the specifications recommended in ASTM E647-78T, described above. The theoretical compliance relationships used for this study were for the condition of loose fitting pins. Figure 6.3 illustrates the importance of this condition being met.

The case of a round pin surrounded by a ceramic sleeve

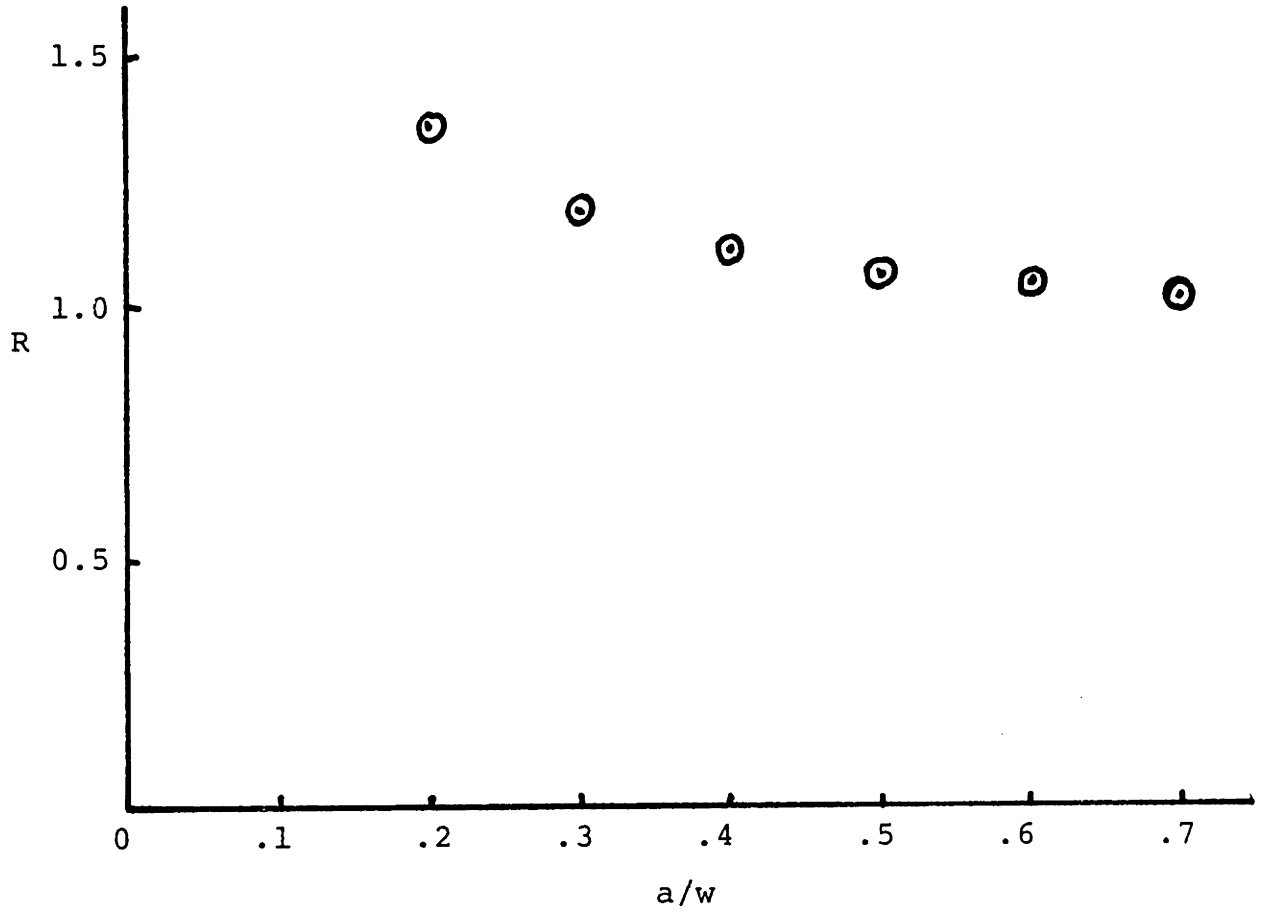

Figure 6.3 Effect of Pin Fit on Measured Compliance

Table 6.1

Effect of Pin Fit on Measured Compliance For Compact Tension Specimen

	a/w .2	.2	.4	.5	.6	.7	.8
EV/P (Loose Pins)	8.6	12.1	17.7	26.9	44.4	80.5	190
EVP (Tight Pins)	6.3	10.1	16.0	25.1	41.8	78.6	189
$R\left(\frac{\text{EV/P Loose}}{\text{EV/P Tight}}\right)$	1.365	1.198	1.106	1.071	1.062	1.024	1.005

has not been analyzed. Based on the above discussed data it was felt that there could be a significant affect on any theoretical compliance analysis used. Since the methematical analysis involved in determining if such an effect is significant is very complicated, involving sophisticated boundary collocation techniques, Newman kindly agreed to perform some preliminary analysis. He calculated the ratio of the displacement predicted for 12.7 mm diameter pins, the size used for this study and the size recommended by the standard, and the displacement predicted for 15.24 diameter pins, the size which simulates the presence of a 1.27 mm thick sleeve around the pin. The assumption was that the latter case was for a loose fitting 15.24 mm diameter pin. The analysis was performed for normalized crack lengths, a/w, of 0.45, 0.65, and 0.8, where a is the crack length measured from the load line and w is the specimen width measured from the load line. Table 6.2 shows the results of Newman's analysis.

Table 6.2

Effect of Pin Size on Predicted
COD Displacements

Normalized Crack Length (a/w)	Displacement for 15.24 mm pin/Displacement for 12.6 mm pin
0.45	1.157
0.65	1.057
0.80	1.003

These results indicate that, if the insulators used in this study amount to the use of a larger diameter, loose fitting pin, new theoretical compliance relationships would have to be developed. If, however, the insulators were tight fitting in the specimen and the pins were loose fitting in the insulators, the analysis showed that there should be no effect. The actual conditions which exist in practice had to be determined experimentally.

6.4.2 Theoretical Compliance vs Crack Length Correlations

As discussed earlier, the crack mouth opening displacement for the compliance measurements was measured using an LVDT attached to the specimen front face. For measurement purposes the exact point of measurement coincided with the center of the core of the LVDT. As illustrated in Figure 6.4, this point is some distance, X, from the actual load line of the specimen. For this study different values of X were used depending on the type of test being conducted. For air tests where specimen isolation from the LVDT was not necessary, the value for X was 34.93 mm yielding a dimensionless distance, X/W, of -.6877. For high temperature tests, the addition of the insulating spacer increased the distance, X, to 36.205 mm for an X/W value of -.7127. For some of the compliance calibration work a clip gauge was used that resulted in a measurement point location 14.43 mm from the load line which yielded a value of X/W of -.284. The compliance calibration correlation for each of these

measurement points was not available, so they were derived theoretically and checked experimentally. In this section we will discuss the derivation of these relationships. The derivation is after that of Hudak et al. [17] and relies heavily on the work of Newman [18] and Wilson [19].

The goal of the analysis is to derive an expression relating compliance to crack length for any arbitrary measurement point a distance X from the load line. The general equations given by Saxena [14] are:

$$\frac{BEV_x}{P} = \left(1 - \frac{X/W}{a/w}\right)\left[\frac{1 + a/w}{1 - a/w}\right]^2 \left\{b_0 + b_1\left(\frac{a}{w}\right) + b_2\left(\frac{a}{w}\right)^2 + b_3\left(\frac{a}{w}\right)^3 \ldots\ldots b_n\left(\frac{a}{w}\right)^n\right\} \quad 6.1$$

OR

$$\frac{a}{w} = C_0 + C_1(U_x) + C_2(U_x)^2 + C_3(U_x)^3 + \ldots\ldots C_n(C_x)^n \quad 6.2$$

where

$$U_x = \frac{1}{\left[\frac{BEV_x}{P}\right]^{1/2} + 1} \quad 6.3$$

where, referring to Figure 6.4

$\frac{a}{w}$ is the dimensionless crack length

$\frac{X}{W}$ is the dimensionless measurement point

$b_0, b_1, b_2 \ldots b_n$ are coefficients determined by regression analysis

B is the specimen thickness

E is the specimen Young's Modulus

P is the specimen load

V_x is the specimen displacement measured at point X

$\frac{BEV_x}{P}$ is the normalized compliance

$C_0, C_1 \ldots C_n$ are constants determined by regression analysis

A second relationship, given by Saxena et al. [14], for the compliance is

$$\frac{BEV_x}{P} = \left[\frac{Xo/W - X/W}{Xo/W + .25}\right] \frac{BEV_o}{P} \qquad 6.4$$

where BEV_o/P is the compliance at location O in Figure 6.4 and

$$\frac{Xo}{W} = \frac{.0924}{1 - V_1/V_0} - 0.25 \qquad 6.5$$

for $.2 \leq a/w \leq .8$ and

$$\frac{Xo}{W} = 0.16 + 0.84\ (a/w) \qquad 6.6$$

for $.8 < a/w \leq 1.0$, where

V_1, V_0 are the displacments measured at points 0, and 1 in Figure 6.4

Table 6.3, derived from reference 14 shows values for V_1/V_0, and other parameters used in the analysis. Xo/W is the axis of rotation for a compact tension specimen with a crack length a. Equation 6.5 is from the work of Newman [18] and

Table 6.3

Compliance and Axis of Rotation X_0/W as a Function of Crack Length for the Compact Tension Specimen

	X/W				
	-0.25	0.1576	0		
a/w	$\frac{BEV_0}{P}$	$\frac{BEV_1}{P}$	$\frac{BEV_L}{P}$	$\frac{X_0}{W}$	$\frac{V_1}{V_0}$
0.20	17.69	14.61	8.6	.2807	.8259
0.25	20.91	17.58	11.18	.0032	.8407
0.30	24.90	21.24	14.28	.3782	.8530
0.35	29.89	25.78	18.09	.4220	.8625
0.40	3[illegible].18	31.51	22.86	.4658	.8709
0.45	44.23	38.83	28.96	.5068	.8779
0.50	54.76	48.44	36.99	.5506	.8846
0.55	69.00	61.44	47.90	.5933	.8904
0.60	89.04	79.78	63.35	.6385	.8960
0.65	118.70	107.00	86.36	.6874	.9014
0.70	165.70	150.00	122.80	.7366	.9053
0.75	245.40	223.50	185.40	.7853	.9108
0.80	397.00	363.10	304.60	.8320	.9146
0.85	743.80	682.65	578.36	.8740	.9178
0.90	1768.20	1628.06	1389.07	.9160	.9207
0.95	7505.50	6931.40	5952.20	.9580	.9235
0.975	30976.40	28647.50	24675.30	.9790	.9248

equation 6.6 is from the work of Saxena [14]. The values given in Table 6.3 are for a condition of plane stress. Plane strain displacements are obtained by multiplying the plane strain displacements by the factor

$$FK = [(1 + K)\ (7-K)]\ /\ 16 \qquad 6.7$$

where

$K = 3-4\ \nu$ for the condition of plane strain where

ν is Poisson's Ratio

The equation for BEV_o/P is given by Saxena [14] and is

$$\frac{BEV_o}{P} = \left[1 + \frac{.25}{a/w}\right]\left[\frac{1+a/w}{1-a/w}\right]^2 \left\{g_0 + g_1\ (a/w) + g_2(a/w)^2 + g_3\ (a/w)^3 + g_4\ (a/w)^4 + g_5\ (a/w)^5\right\} \qquad 6.8$$

where

$g_0 = 1.61369$

$g_1 = 12.6778$

$g_2 = -14.2311$

$g_3 = -16.6102$

$g_4 = 35.0499$

$g_5 = -14.4943$

The procedure for determining a compliance relationship for any arbitrary measurement point location consists of: (1) use equations 6.4 - 6.7 to determine values for BEV_x/P at intervals given by Table 6.2, (2) use the calculated values of BEV_x/P and the known corresponding values of a/w and build a set of n equations with n unknowns, the coef-

ficients in equation 6.1 or 6.2 as desired, (3) use regression analysis to determine the coefficients.

The above procedure was computerized in a computer program which is included as Appendix 1. Table 6.4 lists the coefficients for the constants in equation 6.2 derived for the three measurement point locations for conditions of plane stress and plane strain with a Poisson's ratio of .33.

The derived correlations for crack length vs compliance were used as the starting point for the analysis of the raw COD data vs cycles in the experimental program. However, before this could be done the theoretical correlations were experimentally verified.

6.4.3 Experimental Verification of Compliance Correlations

Experimental verification of the derived compliance correlations was necessary for two reasons. First, as discussed in Section 6.4.1, the effect of the pin insulators was unknown. Second, if the derived correlation could be verified, much time would be saved in not having to derive one experimentally.

Experimental verification of the compliance correlations was performed in two ways. First, specimens with carefully machined slits were obtained. These slits simulated crack lengths of 10.16 mm, 20.32 mm, and 27.94 mm. Compliance for these specimens was checked at two measurement point locations. Table 6.5 shows the results. The measurements

Table 6.4

Regression Coefficients For Crack

Length vs Compliance Correlations

	C_0	C_1	C_2	C_3	C_4	C_5
-.284 (Plane Stress)	1.00108	-4.74449	19.32309	-254.68884	1335.15337	-2428.85428
-.6877 (Plane Stress)	1.00193	-5.62504	34.28127	-588.14257	3891.76752	-9436.57846
-.6877 (Plane Strain)	1.00198	-5.32030	30.86903	-506.50484	3183.21000	-7341.32704
-.7127 (Plane Stress)	1.00198	-5.6765	35.29286	-613.00796	4104.7746	-10089.75854
-.7127 (Plane Strain)	1.00203	-5.36899	31.78308	-527.88138	3357.30518	-7849.47499

Table 6.5

Measured vs Calculated Compliance

Data For Machined Cracks

X/W	a/w	Measured Compliance	Theoretical Compliance	Δ(%)
-.7127	.55	108.9	106.9	+1.9
-.7127	.40	59.5	59.6	-0.17
-.7127	.20	33.6	33.1	+1.5
-.284	.55	72.5	71.8	+.97
-.284	.40	36.6	37.9	-3.4
-.284	.20	18.4	18.8	-2.1

Table 6.6

Measured Compliance and a/w Values

For Beach Marked Specimens

Compliance	$\overline{a/w}$
35.7	.2855
38.1	.2917
38.7	.2928
40.3	.3237
46.9	.3659
49.9	.3862
60.1	.4338
63.1	.4485

were performed at 288°C in the autoclave system. The results scatter randomly about the theoretical curve with a general trend of larger differences at lower values of a/w. This is consistent with the results of the error propagation analysis which will be discussed later.

The second method of verification consisted of beach marking specimens during actual testing and measuring the crack lengths after the test. Specimens were beach marked by alternating between a high and a low mean stress during a test while maintaining the maximum stress constant. Specimens were broken open after testing and crack lengths measured using a three point average. Table 6.6 shows the results of this exercise. In this case the interpretation of the results is more difficult. Figure 6.5 shows the individual compliance-crack length pairs plotted against the theoretical curve. However, the fact that the crack fronts were not straight made it difficult to define which crack length was being measured. This highlights a significant advantage and, at the same time, a significant problem with using compliance techniques to infer crack length. First, what we are really measuring the compliance for is an equivalent through thickness straight crack. The state of stress can crudely be described as one of plane stress at the surface and plane strain in the interior. The gradient from plane stress to plane strain is unknown but will most certainly influence the compliance. For our case the crack fronts were characterized by a rather sharp curvature at

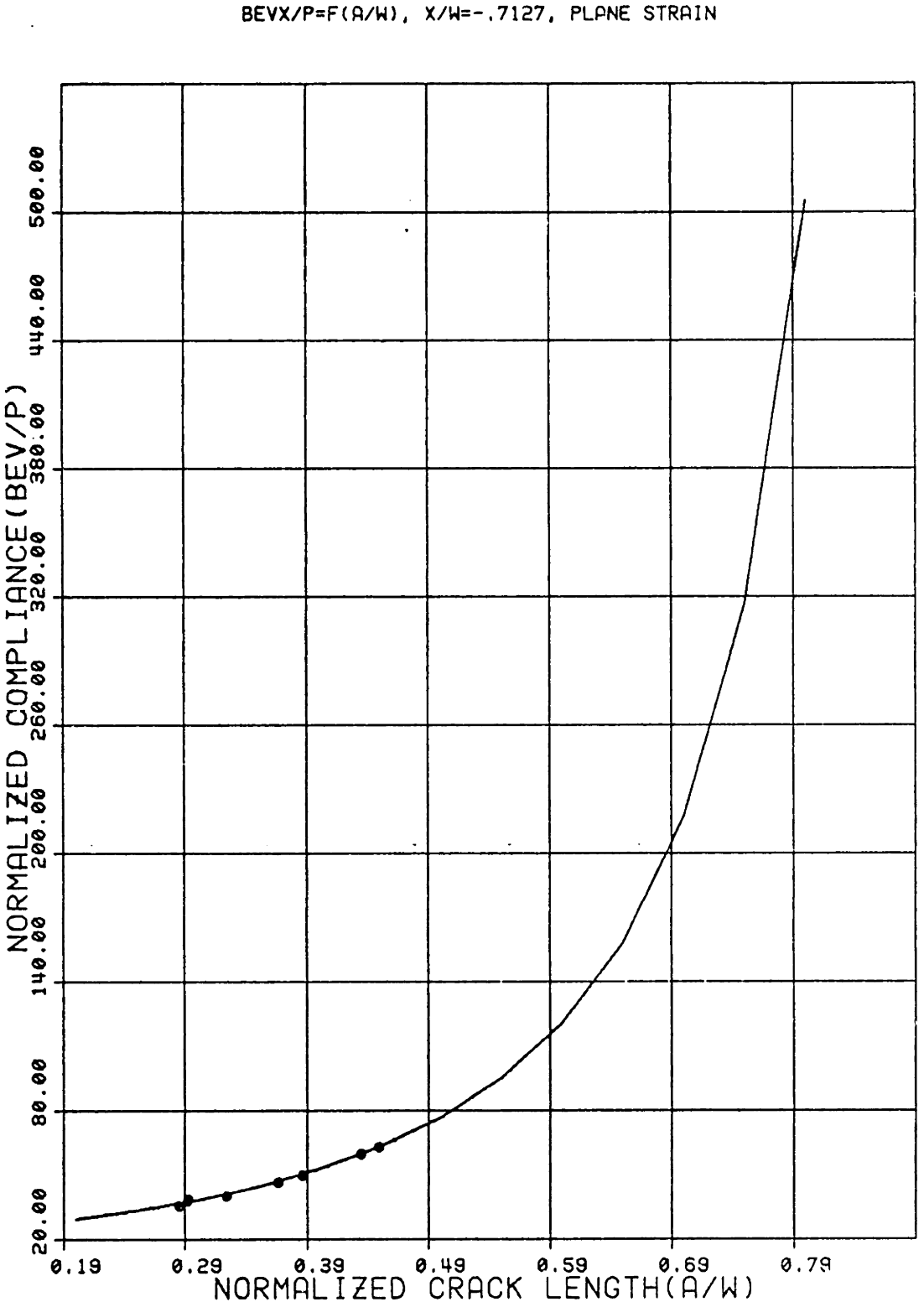

Figure 6.5 Compliance Calibration Data Plotted for Beach Marked Specimens

each surface which straightened out after approximately 10% of the specimen thickness. Thus we would expect that the theoretical compliance relationship applicable in this case would be one for plane strain conditions. This is indeed the case.

Based on the results of the compliance calibration exercises, the conclusion was drawn that the theoretical compliance relationships were adequate for the measurement of crack length. Also, the analysis indicated that the insulating sleeves were acting as if they were part of the specimen. Thus the theoretical analysis for the standard, non-sleeved, specimen design is adequate for our case.

6.5 Error Propagation and Uncertainty Analysis

In principal, the measurement of compliance is a simple matter, requiring the simultaneous measurement of specimen load and an appropriate crack mouth opening displacement. In practice, the measurement of these parameters in an autoclave at high temperatures and pressures is difficult to do with a high degree of accuracy. This fact became apparent early in the experimental program and caused some concern. The reason for this concern is illustrated by Figure 6.1. For values of a/w between 0.2 and 0.45, the slope of the compliance vs a/w curve is very shallow. In this range of crack lengths, a small error in measured compliance can result in a very large error in a/w. This a/w range is precisely the range where the experimental program was

limited to without violating restrictions due to linear elastic fracture mechanics constraints. In this section we will discuss the detailed uncertainty analysis which was conducted and became an integral and indispensable part of the overall program.

6.5.1 Importance of Uncertainty Estimates

The crack length data generated in the experimental program was used to construct a relationship between the crack tip stress intensity factor, K, and the rate of crack growth per cycle, da/dn. The crack tip stress intensity factor is a function of crack length, load, and materials parameters. The simplest and most direct technique for determining da/dn is to simply measure the change in crack length for a selected number of fatigue cycles. To obtain statistically meaningful data, crack length measurements must be made at intervals which insure that a significant (i.e., measurable) change in crack length has occurred. On the other hand, crack length measurements must be made at small enough intervals to insure that the crack tip stress intensity factor has remained essentially constant over the interval. To insure that the above requirements are met, the ASTM guidelines for this type of testing recommend the following restrictions on crack length measurement intervals:

> Crack length should be measured at the following intervals:
>
> $$\Delta a \leq 0.02W \text{ for } .25 \leq a/w \leq .6$$
> $$\Delta a \leq 0.01W \text{ for } a/w > .6$$

The minimum Δa should be 0.25 mm or ten times the crack length measurement precision, which ever is greater

In the case of the compliance technique, the crack length is not directly measured and the important parameter is the calculated compliance. Figure 6.1 illustrates the fact that the required measurement precision for a given change in crack length will be a function of the instantaneous crack length. This is particularly true in the crack length range of 10-30 mm (a/w from .2 - .6) when the slope of the compliance-crack length curve is the shallowest. Ballinger [20] has evaluated the precision requirements for compliance measurement in order that the ASTM guidelines be met. Table 6.7 shows the results of his analysis.

Table 6.7

Required Compliance Measurement Precision to Meet ASTM-E647-78T Requirements [20]

Normalized Crack Length (a/w)	Approximate Compliance (BEV_x/P)	Required Precision of Compliance Measurement as per ASTM-E647-78T
.2	32.6	0.4%
.3	42.7	0.5%
.4	58.8	0.7%
.5	85.5	0.8%
.6	134.0	1.0%
.7	241.0	1.2%
.8	600.0	2.3%

From an inspection of Figure 6.1 and Table 6.7 it is obvious that, even under the most carefully controlled conditions, these requirements are not likely to be met.

The above discussion highlights a potentially serious problem. Since the ASTM recommendations cannot be met, what degree of confidence can be placed on data generated using the compliance technique? The question also might be asked whether the ASTM recommendations are appropriate for indirect crack length measurement techniques.

The answer to the first question is central to determining the appropriateness of using this type of crack growth data to predict component life. If the degree of confidence is unknown for a data set, then component life prediction using that data set is impossible. The answer to the second question requires careful analysis of the whole procedure used in fatigue crack growth rate testing using compliance techniques.

Because of the questions raised in the preceeding discussion and because, in a more direct sense, the answers to the above questions would determine the usefulness of data generated in this program, a full and detailed analysis was performed in an attempt to establish an estimate for the uncertainty in the fatigue crack growth rate data generated in this program.

Apart from the obvious purpose of establishing confidence limits on experimental data, the process of estimating the uncertainty in the overall results can provide

important additional information. A full and as accurate an uncertainty analysis as possible can provide information concerning sources of error which can help in the design of an experiment in the beginning, as well as help in the interpretation of data at the end. Uncertainty analysis can also provide the basis for a consistency check between what one thinks his potential error is and what it actually turns out to be. A well designed uncertainty analysis will provide an estimate for the expected uncertainty in data generated during a given experiment before the experiment is performed. Scatter in the actual experimental data should be consistent with the estimated uncertainty. If this is not the case, the experimenter has either overlooked a potential source of error or the experimental results are being influenced by something which is not related to the experimental technique. The latter result is generally the objective of the program in the first place and an uncertainty analysis can determine what is a real effect and what is not. The following sections will deal first with the general techniques for error propagation and uncertainty analysis and finish with an overall analysis for the experimental procedures and systems used in this investigation.

6.5.2 General Uncertainty Analysis

A well constructed experimental analysis program consists of several major parts which are linked together. The link is the uncertainty or error analysis. In general, the

experiment provides the investigator with values of two or more independent variables, and several parameters which characterize the experimental setup. Using this information the dependent variable is calculated using a mathematical relationship. The dependent variable will exhibit some degree of scatter as a result of scatter in the independent variables. The scatter which results from scatter in the independent variable may not be the only source of scatter. Other sources may include materials variability or effects not included in the analysis. An uncertainty analysis of the experimental system provides for a consistency check on the overall analysis. If errors are estimated for the independent variables and parameters, they can be propagated through the relationship between the independent variables and the dependent variable. The result will be an estimate of the overall uncertainty in the dependent variable. This uncertainty estimate should be in general agreement with the overall scatter in the calculated dependent variable. If this is true, then the experiment is at least internally consistent. If this is not true, then something is wrong. Either the independent variable uncertainty estimates are incorrect or some other outside influence is operative.

The basic equations for propagation of errors are given by Benington [21] for a dependent variable (Z) which is calculated from the measurement of several indepdndent variables. $(X_1, X_2, \ldots X_i, \ldots X_n)$

$$Z = F\ (X_1, X_2, \ldots X_n) \qquad 6.9$$

The variance in Z is defined as follows:

$$\text{Var}\ (Z) = \sum_{i,j=1}^{n} \left(\frac{\partial f}{\partial x_i}\Big|_a\right)\left(\frac{\partial f}{\partial x_j}\Big|_a\right) \sigma_{x_i x_j} \qquad 6.10$$

$\sigma_{x_i x_j}$ is the covariance between variables i and j and is defined as

$$\sigma_{x_i x_j} = \left\langle (x_i - \langle x_i \rangle)\ \ (x_j - \langle x_j \rangle) \right\rangle \qquad 6.11$$

variables or groups of variables enclosed by < > are the average or expected value for these variables. When i = j $\sigma_{x_i x_j}$ is defined as σ_x^2 and is the variance of the variable x_i,

$$\sigma_{x_i x_j} = \sigma_x^2 \quad \text{if } i = j \qquad 6.12$$

The terms $\frac{\partial f}{\partial x_i}\Big|_a$ and $\frac{\partial f}{\partial x_j}\Big|_a$ are the partial derivatives of z with respect to the variables x_i and x_j respectively and are evaluated at the average value for the respective variables, that is:

$$A = F\ (\langle x_1 \rangle\ ,\ \langle x_2 \rangle\ ,\ \ldots\ \langle x_i \rangle\ ,\ \ldots\ \langle x_n \rangle) \qquad 6.13$$

The above equations are completely general with the only assumptions being that the function Z can be expanded in a Taylor series about the average values and that the first two terms of the expansion are the only ones that are significant. In a practical sense, this requires that the function Z be a smooth function.

An error propagation analysis for a given experiment consists of applying equations 6.9 - 6.13 to the system of

equations describing the experiment. As is done here the dependent variable for one part of the analysis becomes the independent variable for the next stage. Errors are thus propagated until uncertainty estimates are obtained on the primary dependent variable.

6.5.3 Uncertainty in Fatigue Crack Growth Rate Data

6.5.3.1 Uncertainty in Compliance Measurement

For a standard compact tension specimen the elastic compliance is defined as:

$$C - BE\frac{dv}{dp} = \frac{BEKS}{P} \qquad 6.14$$

where

C = the specimen normalized compliance

B = the specimen thickness (mm)

E = Young's Modulus (MPa)

$\frac{dv}{dp}$ = the slope of the load displacement curve

K = the calibration constant for the LVDT with units of volts/mm

S = the increment in crack opening displacement (mm)

P = the load increment for the measured displacement (newtons)

The combination of variables $\frac{KS}{P}$ are the experimental equivalent to dv/dp. When equation 6.10 is applied to equation 6.14, with some simplification, the following equations results:

$$\text{Var}\ (C) = \overbrace{\left(\frac{\partial C}{\partial B}\right)^2 \sigma_B^2}^{1} + \overbrace{\left(\frac{\partial C}{\partial E}\right)^2 \sigma_E^2}^{2} + \overbrace{\left(\frac{\partial C}{\partial K}\right)^2 \sigma_K^2}^{3} + \overbrace{\left(\frac{\partial C}{\partial S}\right)^2 \sigma_S^2}^{4}$$
$$+ \overbrace{\left(\frac{\partial C}{\partial P}\right)^2 \sigma_P^2}^{5} + \overbrace{2\left(\frac{\partial C}{\partial S}\right)\left(\frac{\partial C}{\partial P}\right) \sigma_{S,P}}^{6} \qquad 6.15$$

where:

Term 1 represents the contribution from the variance in the specimen thickness.

$$\left(\frac{\partial C}{\partial B}\right)^2 \sigma_B^2 = \left(\frac{EKS}{P}\right)^2 \sigma_B^2 \qquad 6.16$$

σ_B^2 is the variance in the specimen thickness

Term 2 represents the contribution from the variance in the Young's Modulus.

$$\left(\frac{\partial C}{\partial E}\right)^2 \sigma_E^2 = \left(\frac{BKS}{P}\right)^2 \sigma_E^2 \qquad 6.17$$

σ_E^2 is the variance in the Young's Modulus

Term 3 represents the contribution from the variance in the calibration constant for the LVDT used to measure crack opening displacement.

$$\left(\frac{\partial C}{\partial K}\right)^2 \sigma_K^2 = \left(\frac{BES}{P}\right)^2 \sigma_K^2 \qquad 6.18$$

σ_K^2 is the variance in the LVDT calibration constant

Term 4 represents the contribution from the variance in the measured change in crack opening displacement for a given change in load during a compliance measurement.

$$\left(\frac{\partial C}{\partial S}\right)^2 \sigma_S^2 = \left(\frac{BEK}{P}\right)^2 \sigma_S^2 \qquad 6.19$$

σ_S^2 is the variance in the crack opening displacement measurement

Term 5 represents the contribution from the variance in the load measurement during a compliance measurement.

$$\left(\frac{\partial C}{\partial P}\right)^2 \sigma_P^2 = \left(\frac{BEKS}{P^2}\right)^2 \sigma_P^2 \qquad 6.20$$

σ_P^2 is the variance in the load measurement

Term 6 represents the contribution from the possible covariance between the load measurement errors and displacement measurement errors. By the nature of the compliance measurement, any load pulsations will result in displacement pulsations. These errors can thus be expected to be correlated.

$$2\left(\frac{\partial C}{\partial S}\right)\left(\frac{\partial C}{\partial P}\right) \sigma_{S,P} = -2\left(\frac{BEK}{P}\right)^2 \left(\frac{S}{P}\right) \sigma_{S,P} \qquad 6.21$$

$\sigma_{S,P}$ is the covariance between the load measurement and crack opening displacement as defined by equation 6.11

The S,P covariance is assumed to be the only source of covariance. This is not an unreasonable assumption due to the independence of the other terms in the analysis.

The solution to equation 6.15 requires that a realistic estimate be made for the values of σ_B^2, σ_E^2, σ_S^2, σ_P^2, and $\sigma_{S,P}$. The square root of any of these quantities represents the standard deviation (uncertainty) in the quantity.

The uncertainty in B will, in general, have little influence on the overall uncertainty. An accurate estimate for σ_B^2 is, however, easy to obtain by measuring several (10) specimens.

Uncertainty in E can have a significant effect on the

overall results. The value for E that should be used is that for the test conditions. An actual measured value for E is the most desirable. If this is not available, an attempt should be made to input a realistic value for the uncertainty in E at test conditions.

Uncertainties in the absolute load measurement should include effects of friction, instrument calibration errors, load train misalignment, etc., for the test conditions of interest. Uncertainties in P have a significant effect on the contribution of errors in P_{min} for the load range of interest and thus will effect errors in the stress intensity factor range.

The LVDT used for displacement measurement should be calibrated at test conditions. This has been found to be the most significant source of overall error in a test system.[20] Special effort should thus be expended in obtaining an accurate estimate for this variable. An assumption that an air value for K will be the same as that at test conditions is not valid. The interactions between system temperature, pressure, and flow fluctuations on specimen load are complex and can effect the stability of the load loop in the servohydraulic machine.

The uncertainty in crack mouth opening displacement can be estimated for each compliance measurement by repeating the measurement several (10) times and calculating a standard deviation. The value for σ_S should be measured for each increment in crack length since it will generally be a

function of crack length.

The S-P covariance represents the degree of correlation between displacement and load. A load fluctuation during a measurement of displacement will influence the latter. Notice in equation 6.21 that S-P covariance enters as a negative value and will reduce overall uncertainty. However, since the value of σ_K usually dominates, the value input for $\sigma_{S,P}$ has little effect on the outcome. Since fluctuations in load come about due to fluctuations in system pressure, $\sigma_{S,P}$ is zero for air measurements.

6.5.3.2 Uncertainty in Crack Length

Once an estimate for the uncertainty in compliance is obtained, the compliance and its uncertainty can be used as independent variables in the analysis of the associated uncertainty in crack length. However, before this can be done, a compliance calibration curve which relates crack length with compliance must be generated. Compliance calibration curves can be derived either theoretically or empirically. Theoretical crack length vs compliance relationships exist for specimens of the same design used for most crack growth analysis [14]. In general, experimental and theoretical compliance-crack length relationships agree quite well, usually within five percent when the experimental calibration curve is derived under carefully controlled conditions. For purposes of this analysis, the relationship between compliance and crack length is assumed to be without

error. This is a significant assumption and can be expected to artifically reduce the calculated error. A second assumption which must be made is that the crack length implied in this analysis corresponds to an equivalent through thickness straight crack, corresponding to the measured crack length. The following analysis uses a relationship derived for a normalized COD measurement location of -.6877 which, with a/w of 50.8 mm, corresponds to a point 34.93 mm from the load line towards the front of the specimen.

With the above assumptions, the following relationship can be written relating normalized crack length (a/w) with normalized compliance, C.

$$a/w = f(C) \tag{6.22}$$

$$a/w = A_0 + A_1U + A_2U^2 + A_3U^3 + A_4U^4 + A_5U^5 \tag{6.23}$$

$$U = \frac{1}{\sqrt{C} + 1} \tag{6.24}$$

where for the case of x/w = -.6877

$A_0 = 1.00193$

$A_1 = -5.62504$

$A_2 = 34.28127$

$A_3 = -588.14257$

$A_4 = 3891.76752$

$A_5 = -9436.57846$

when equation 6.10 is applied to equation 6.23 the result is:

$$\text{var}\left(\frac{a}{w}\right) = \left(\frac{\partial F}{\partial C}\right)^2 \sigma_C^2 \qquad 6.25$$

σ_C^2 is the variance in the compliance value

Evaluating the partial derivative of equation 6.23 with respect to C:

$$\frac{\partial F}{\partial C} = E_\phi \left(\frac{\partial U}{\partial C}\right) + E_1 \left(\frac{\partial U}{\partial C}\right) U + E_2 \left(\frac{\partial U}{\partial C}\right) U^2 + E_3 \left(\frac{\partial U}{\partial C}\right) U^3 + E_4 \left(\frac{\partial U}{\partial C}\right) U^4 \qquad 6.26$$

$$\frac{\partial U}{\partial C} = \frac{1}{2\sqrt{C}\left(\sqrt{C}+1\right)^2} \qquad 6.27$$

$E_\phi = -5.62504$

$E_1 = 68.5734$

$E_2 = -1764.42771$

$E_3 = 15567.07008$

$E_4 = -47182.8923$

6.5.3.3 Uncertainty in Stress Intensity Factor

Once the uncertainty in crack length is determined it can be used in the calculation of the uncertainty in the stress intensity factor range. The stress intensity factor relationship used for this analysis is that derived by Newman [16].

$$K = Y\ (B,\ P,\ W,\ a/w) \tag{6.28}$$

$$K = \frac{P}{B\ W}\ F\ (a/w) \tag{6.29}$$

where

B = the specimen thickness (mm)

P = the specimen load (newtons)

W = the specimen width (mm)

$$F\ (a/w) = B_0 + B_1\ (\frac{a}{w}) + B_2\ (\frac{a}{w})^2 + B_3\ (\frac{a}{w})^3 + B_4\ (\frac{a}{w})^4 + B_5\ (\frac{a}{w})^5 + B_6\ (\frac{a}{w})^6 \tag{6.30}$$

$B_0 = 4.55$

$B_1 = -40.32$

$B_2 = 414.7$

$B_3 = -1698.0$

$B_4 = 3781.0$

$B_5 = -4287.0$

$B_6 = 2017.0$

The relationship for the stress intensity factor range is

$$\Delta K = K_{max} - K_{min} \tag{6.31}$$

$$\Delta K = \frac{P_{max}}{B\sqrt{W}}\ F\ (a/w) - \frac{P_{min}}{B\sqrt{W}}\ F\ (a/w) \tag{6.32}$$

When equation 6.10 is applied to equation 6.32, the following equation is obtained:

$$\text{Var}(\Delta K) = \overbrace{\left(\frac{\partial F}{\partial B}\right)^2 \sigma_B^2}^{1} + \overbrace{\left(\frac{\partial F}{\partial W}\right)^2 \sigma_W^2}^{2} + \overbrace{\left(\frac{\partial F}{\partial P_{max}}\right)^2 \sigma_{P_{max}}^2}^{3} + \overbrace{\left(\frac{\partial F}{\partial P_{min}}\right)^2 \sigma_{P_{min}}^2}^{4} + \overbrace{\left(\frac{\partial F}{\partial a/w}\right)^2 \sigma_{a/w}^2}^{5} \qquad 6.33$$

Term 1 is the contribution to the variance from the variance in specimen thickness

$$\left(\frac{\partial F}{\partial B}\right) = \frac{F(a/w)}{B^2\sqrt{W}} \quad (P_{min} - P_{max}) \qquad 6.34$$

σ_B^2 is the variance in the specimen thickness

Term 2 is the contribution to the variance from the variance in specimen width

$$\left(\frac{\partial F}{\partial W}\right) = \frac{F(a/w)}{2\ BW^{3/2}} \quad (P_{min} - P_{max}) \qquad 6.35$$

σ_W^2 is the variance in the specimen width

Term 3 is the contribution to the variance from the variance in P_{max}

$$\left(\frac{\partial F}{\partial P_{max}}\right) = \frac{F(a/w)}{B\sqrt{W}} \qquad 6.36$$

$\sigma_{P_{max}}^2$ is the variance in the maximum specimen load (P_{max})

Term 4 is the contribution to the variance from the variance in P_{min}

$$\left(\frac{\partial F}{\partial P_{min}}\right) = -\frac{F(a/w)}{B\sqrt{W}} \qquad 6.37$$

$\sigma^2_{P_{min}}$ is the variance in the minimum specimen load (P_{min})

Term 5 is the contribution to the variance from the variance in a/w

$$\frac{\partial F}{\partial a/w} = \frac{(P_{max} - P_{min})}{B\sqrt{W}} \left[C_0 + C_1(a/w) + C_2(a/w)^2 + C_3(a/w)^3 + C_4(a/w)^4 + C_5(a/w)^5 \right] \qquad 6.38$$

where

$C_0 = -40.32$

$C_1 = 829.4$

$C_2 = -5094.0$

$C_3 = 15124.0$

$C_4 = -21435.0$

$C_5 = 12102.0$

$\sigma^2_{a/w}$ is the variance in a/w calculated in equation 6.25

6.5.3.4 Uncertainty in da/dn vs ΔK

The final step in the analysis is to use the uncertainty in ΔK calculated in equation 6.33, along with an estimate of the uncertainty in da/dn to present the data. At this point in the analysis a problem arises. What we want to determine ultimately are the answers to the following questions: (1) Given a mean ΔK, what is the probable spread about that mean

that we can expect? and (2) At the mean value of ΔK, what is the mean value of da/dn and what is the probable spread of da/dn about the mean?

The analysis presented thus far allows us to answer question 1. The answer to question 2 can be estimated using two approaches. Each of these approaches has its limitations but the results from each can also be instructive.

The first approach that can be taken is to obtain a relationship between da/dn and ΔK using data reduction techniques such as those recommended in ASTM E647-78T, "Tentative Test Method for Constant-Load-Amplitude Fatigue Crack Growth Rates Above 10^{-8} m/cycle". Using these procedures, raw crack length vs cycles data is reduced to da/dn data by using either a point by point secant differentiation technique or a seven point polynomial fitting technique. Once this is done, the da/dn data can be fit to an appropriate functional form relating it to ΔK. A common relationship for the range of crack growth rates in this program is

$$\frac{da}{dn} = C\Delta K^n \qquad 6.39$$

which is of the functional form

$$Y = AX^B \qquad 6.40$$

The da/dn vs ΔK data can be fit to an equation of the form 6.40 by the method of least squares with the exponent B and the coefficient A calculated according to the relationships

$$B = \frac{\sum_{j=1}^{n}(\ln X_j)(\ln Y_j) - \frac{\left(\sum_{j=1}^{n}\ln X_j\right)\left(\sum_{j=1}^{n}\ln Y_j\right)}{n}}{\sum_{j=1}^{n}(\ln X_j)^2 - \frac{\left(\sum_{j=1}^{n}\ln X_j\right)^2}{n}} \qquad 6.41$$

$$A = \exp\left[\frac{\sum_{j=1}^{n}\ln Y_j}{n} - B\,\frac{\sum_{j=1}^{n}\ln X_j}{n}\right] \qquad 6.42$$

with a goodness of fit parameter defined as:

$$R^2 = \frac{\left[\sum_{j=1}^{n}(\ln X_j)(\ln Y_j) - \frac{\left(\sum_{j=1}^{n}\ln X_j\right)\left(\sum_{j=1}^{n}\ln Y_j\right)}{n}\right]^2}{\left[\sum_{j=1}^{n}(\ln X_j)^2 - \frac{\left(\sum_{j=1}^{n}\ln X_j\right)^2}{n}\right]\left[\sum_{j=1}^{n}(\ln Y_j)^2 - \frac{\left(\sum_{j=1}^{n}\ln Y_j\right)^2}{n}\right]} \qquad 6.43$$

where n is the number of data points.

If the fit to equation 6.39 is very good, as defined by a goodness of fit parameter greater than 0.999, equation 6.39 can be differentiated and used in the following relationship for the variance in da/dn,

$$\text{var}\left(\frac{da}{dn}\right) = \left(\frac{\partial f}{\partial \Delta K}\right)^2 \sigma^2_{\Delta K} \qquad 6.44$$

where

$$f(\Delta K) = C\Delta K^n$$

$$\frac{\partial f}{\partial \Delta K} = \left[Cn\Delta K^{n-1}\right]^2 \qquad 6.45$$

$\sigma^2_{\Delta K}$ is the variance in ΔK at the point of interest as calculated by equation 6.33.

The advantage of using this technique is that it provides us with a continuous mathematical relationship for the uncertainty in da/dn. A serious disadvantage of this method is that it does not provide us with an independent determination of the uncertainty in da/dn and does not provide us with any information concerning possible dependency on experimental or other variables, save ΔK. Also, the strong dependence upon the exponent n requires that the fit to the data be extremely good.

A second and more fundamental approach to the problem is to attempt an estimate in the error on Δa independently, realizing that Δn is a constant without error.

Starting with equation 6.22, we can write an expression for the increment in crack length

$$\Delta\left(\frac{a}{w}\right) = f(c_1) - f(C_0) = f(C_0, C_1) \qquad 6.46$$

where C_1, C_0 are the compliances at the end and beginning of a measurement interval

and an expression can be then written for the variance in $\Delta\left(\frac{a}{w}\right)$ by applying equation 6.10 to equation 6.46.

$$\text{Var}\left[\Delta\left(\frac{a}{w}\right)\right] = \left[\frac{\partial f(C_0,C_1)}{\partial C_1}\bigg|_{C_1}\right]^2 \sigma^2_{C_1} + \left[\frac{\partial f(C_0,C_1)}{\partial C_0}\bigg|_{C_0}\right]^2 \sigma^2_{C_0}$$

$$+ 2\left[\frac{\partial f(C_0,C_1)}{\partial C_1}\bigg|_{C_1}\right]\left[\frac{\partial f(C_0,C_1)}{\partial C_0}\bigg|_{C_0}\right]\sigma^2_{C_0C_1}$$

6.47

The first two terms represent the errors in crack length at the beginning and end of a measurement interval. The third term represents the correlation or covariance between the errors at the measurement interval end points. This term enters as a subtractive for positively correlated errors.

The advantage of this method is that the estimated error in Δa is independent of the functional form used for the da/dn vs ΔK relationship and that the error estimate exhibits what we intuitively feel are the right functional dependencies. That is, the error depends on the error in crack length at the end points of the measurement interval and, due to the shape of the compliance vs crack length curve, the length of the measurement interval. However, while this method may be more fundamentally pleasing, the actual evaluation of equation 6.47 requires us to obtain an estimate of $\sigma_{C_0C_1}$, the correlation coefficient between the errors at the measurement interval end points. The determination of $\sigma_{C_0C_1}$ requires that the uncertainty in the compliance vs crack length correlation be known or can be determined. In addition, to determine the sign of the correlation the distribution of the errors must be known. A proper analysis to determine this information would require thay many, probably hundreds, of specimens be processed and broken open at intervals over the entire a/w range in order that a statistically significant number of independent data point pairs of compliance and crack length values be obtained. This analysis was beyond the capability, in terms of both

time and specimens available, for this program.

In spite of the shortfalls discussed above, an estimate of the uncertainty in da/dn for a given ΔK can be determined by both techniques and, if we are careful in the interpretation of the results, valuable information can be obtained.

6.5.4 Estimates of Uncertainties for System and Physical Parameters

The actual determination of an estimate of the uncertainty in the data requires that estimates be obtained for the variances in the input parameters for the experiment. This section presents these results.

6.5.4.1 Uncertainties in Specimen Thickness (B)

The uncertainty in the specimen thickness was found to be ± .0127 mm based on the measurement of several tens of specimens.

6.5.4.2 Uncertainty in Specimen Load (P)

Uncertainties in specimen load arise due to several factors. The design of the system pressurization system makes use of a positive displacement reciprocating pump and a back pressure regulator. The nature of the pump operation results in a system pressure fluctuation with a frequency corresponding to the speed of rotation of the pump. The pressure pulsations are damped out to the max-

imum extent possible by using a pulsation damper on the pump discharge. In spite of this, there is a finite pressure fluctuation which results in a load fluctuation on the specimen which is not fully compensated for by the fatigue machine electronics. Load fluctuations were observed to be approximately 90 Newtons for most test conditions due to system pressure fluctuations.

Another source of load uncertainty is due to friction between pullrods and autoclave seals, as well as load train misalignment. System design tends to minimize load train misalignment. This condition was confirmed by the fact that the fatigue cracks remained in the plane perpendicular to the load line and the front and back surfaces of the crack remained aligned. Load uncertainties due to seal friction was estimated to be ±112 N by recording load fluctuations during actuator movement without a specimen installed.

A final source of load uncertainty is due to load cell calibration errors and load zeroing errors prior to a test. Based on the manufacturers specifications and an experience with the test procedures, an estimate for this type of error of ± 20.1 N was determined.

The total load uncertainty was calculated from the above and found to be 222.4 N.

6.5.4.3 Uncertainties in LVDT Calibration Constant

As estimate of the uncertainty in the LVDT calibration was obtained by calibrating the LVDT using a capacitance

gauge as a standard with an accuracy of ± .0005 mm. The LVDT was calibrated under operating conditions by attaching the LVDT to a set of specially machined fixtures in the autoclave and attaching the capacitance gauge to the fatigue machine actuator outside the autoclave. The LVDT was calibrated over a 0.5 mm interval in steps of .025 mm at room temperature in an and at operating pressure and temperature in high purity water. For room temperature conditions, the LVDT calibration constant was found to be .0509 ± .0021 mm/volt. For operating conditions, the LVDT calibration constant was found to be .0521 ± .0035 mm/volt. For comparison purposes, the LVDT was calibrated under carefully controlled conditions on a bench calibration fixture. For these conditions, the calibration constant was found to be .05087 ± .0007 mm/volt. The difference between the three uncertainties is due to the increasing amount of system influence as we proceed from the bench to the fatigue machine system with no pumping pressure and friction fluctuations and from there to operating conditions of temperature and pressure. The result is a five fold increase in the measurement uncertainty.

6.5.4.4 Uncertainty in COD Displacement Measurement

For this investigation compliance was determined at selected cyclic intervals by suspending the test and manually determining the slope of the load vs displacement

curve during specimen unloading. This required the measurement of load and displacement at a minimum of two points so that a slope could be determined. As a check on the linearity of the unloading load vs displacement curve four load/displacement pairs were recorded. For each compliance determination a minimum of four compliance measurements were made. A standard deviation for each compliance determination was thus calculated and input as part of the raw data. An average value for this uncertainty was found to be of the order of ± .0056 volt with larger values occurring at low a/w values and smaller values occurring at larger a/w values.

6.5.4.5 Uncertainty in Specimen Width

An average uncertainty in specimen width was found to be ± .127 mm.

6.5.4.6 Uncertainty in Elastic Modulus

The value of the elastic modulus used for the elevated temperature work was determined from the modulus at room temperature by recording compliance values for the specimens used in the compliance calibration checks at both room temperature and operating temperature. The assumption was made that the difference in compliance between the two temperatures was due to a change in elastic modulus. A new modulus was then calculated by forcing the two compliances to be equal by adjusting the modulus. This is

admittedly a round about and somewhat crude procedure and because of this, the uncertainty assigned to the modulus was increased by 30% for elevated temperature operation. The value used for the elevated temperature elastic modulus was determined to be $1.89 \times 10^5 \pm 1.034 \times 10^4$ MPa.

6.5.5 Uncertainty Analysis Implementation and Evaluation

The overall error analysis discussed in this section was incorporated into a data analysis computer program called UCRAK. The programming details have been incorporated into a reference data analysis document [22].

An evaluation of the correctness, or at least the applicability, of the overall analysis was performed as part of the experimental program. A check on the absolute correctness of the analysis was impossible but several things could be done to at least insure that the analysis was not incorrect. First, at least two data points for measured crack length and compliance were available for each test. After each test a check could be made by measuring the crack length at the beginning and end of the test. These measured values should be consistent with the values predicted by the analysis. A second check was performed by conducting a set of artificial tests using data generated by Monte Carlo techniques. This analysis was performed on actual experimental data and will be discussed as part of section seven.

Before continuing, a few general comments are in order concerning the general results of the uncertainty analysis. First, the dominating factor in the uncertainty in crack length turned out to be the uncertainty in the LVDT calibration constant. Second, in evaluating the estimated uncertainty in Δa (equation 6.47), the covariance term is of pivotal importance. The implications of these two findings will be discussed in Section 7.

6.6 Linear Elastic Fracture Mechanics Considerations

The analysis of fatigue crack growth data using Linear Elastic Fracture Mechanics, (LEFM), techniques places certain restrictions on the specimen design, configuration in terms of size, and section stresses. [23] The fundamental requirement is that the stresses in the specimen remain predominantly elastic at all times. This means that the plastic zone ahead of the propagating crack must be small compared to the uncracked ligament. This places restrictions on specimen overall size and useful range of crack lengths.

A second consideration, due to the use of the compliance method for crack length measurement, is that the entire system remain elastic during a compliance measurement. This places a restriction on the maximum load achieved during a compliance measurement.

A third consideration is based on eliminating the possibility of specimen buckling and minimizing crack front curvature or "tunneling". These considerations place re-

strictions on specimen dimensions.

6.6.1 Specimen Size Requirements

The recommended size requirements, based on the above considerations, are discussed in ASTM E647-78T, "Tentative Test Method for Constant-Load-Amplitude Fatigue Crack Growth Rates Above 10^{-8} m/cycle", and are as follows:

> The recommended thickness (B) for a compact tension specimen should be in the range $W/20 \leq B \leq W/4$ where W is the specimen width measured from the load line.
>
> The uncracked ligament (W-a) should be equal to or greater than $(4/\pi)\ (K_{max} / \sigma_{ys})^2$ where σ_{ys} is the 0.2% offset yield strength of the test material, K_{max} is the maximum crack tip stress intensity factor achieved, and a is the crack length measured from the load line.

The specimens used for the experimental investigation had dimensions:

$B = 12.7$ mm

$W = 50.8$ mm

$W/4 = 12.7$ mm

these dimensions are consistant with the first requirement above.

Table 6.8 shows the maximum allowable values for crack

Table 6.8

Recommended Maximum Valid Crack Lengths For Program Test Conditions

K_{max} (MPa $\sqrt{m}$)	A_{max} (mm) 288°C	A_{max} (mm) 25°C
10	47.77	49.48
15	43.98	47.82
20	38.68	45.51
25	31.86	42.53
30	23.53	38.90
35	13.68	34.60
40	2.32	29.64
45	---	24.02
50	---	1.77
55	---	---

length (a) as a function of K_{max} for the two test temperatures used in the program. Referring to Table 4.4, the 0.2% offset yield stress at 25 and 288°C are 310 and 205 MPa, respectively. As in evident from Table 6.8, the usable range of crack length is very restricted for the combination of specimen dimensions and mechanical properties used in this investigation.

Recognizing that the specimen size requirements listed above may be a limiting factor for many high toughness materials, ASTM E647-78T provides for a mechanism by which valid data may still be obtained, providing an additional constraint is satisfied. This requirement is expressed in the following equation.

$$V_{max} \leq \frac{2\Delta V}{1-R} \qquad 6.48$$

where

V_{max} is the maximum specimen deflection during a test

ΔV is the deflection range

R is the stress ratio and is equal to the minimum load divided by the maximum load during a test

The requirement described by equation 6.48 is discussed at length in ASTM E647-78T. During a fatigue crack growth test with a high toughness material, the average crack opening displacement range increases with increasing crack length. However, with tough materials there may be an increasing

contribution to the total deflection due to plastic deflection. While the displacement range, $V_{max} - V_{min}$, changes as expected the value for V_{min} also increases for the same minimum load. Thus, the measured total deflection exceeds the elastically calculated total deflection. However, while the total displacements differ, experience has shown that the displacement ranges, measured and calculated, remain essentially constant as long as equation 6.48 is satisfied. The procedure suggests that data generated for conditions which do not satisfy this equation should be flagged, but still reported. These recommendations were followed for this investigation.

7.0 Results and Discussion

The experimental program was conducted in accordance with the guidelines defined in Task one. Fatigue crack growth rate tests were conducted on the Alloy-600 material in two meatllurgical conditions: (1) mill annealed plus a 700°C age for 2 hours and (2) mill annealed plus a 700°C age for 120 hours. Tests were conducted at room temperature in air and at 288°C in high purity low oxygen water. In addition to the above tests, a test was run using the 120 hour aged material at 288°C in high purity air saturated water. An additional test was conducted on the as received material in air at room temperature. For purposes of this discussion, the material that has been aged for 2 hours at 700°C will be termed "sensitized" material and that aged for 120 hours at 700°C will be termed "desensitized" material.

The data for each test was processed using the prog-cedures developed in Task three. For most of the specimens crack length was measured on broken specimens after testing, using a traveling microscope. Fractography was performed on selected broken specimens using the Scanning Electron Microscope (SEM).

As a further check on the validity of the uncertainty analysis procedures developed in Task three, a Monte Carlo analysis was conducted using the experimental uncertainties and data for one of the high temperature tests.

7.1 Results

7.1.1 Results: Crack Length vs Number of Cycles

Figures 7.1 - 7.8 show the calculated crack length vs elapsed cycles for the tests run in the program. Also shown on these plots are the measured crack lengths at the beginning and end of tests for specimens which could be measured. An intermediate measurement was possible for sample MA2-3 (Figure 7.3) due to an interrupted test. Table 7.1 shows the measured and calculated crack lengths. Crack lengths were measured on broken specimen fracture surfaces using a three point average. The plotted spread represents the maximum and minimum.

7.1.2 Monte Carlo Analysis of Crack Length Measurements

The general agreement between the calculated uncertainties on crack length and actual measurements support the appropriateness of the general analytical technique. However, the actual experimental verification of the mathematical analysis would require the testing and measurement of many more specimens than were available for this investigation. In an attempt to further confirm the mathematical analysis used for data reduction, one of the tests, MA2-3, was simulated using data generated by Monte Carlo techniques. Simulation data sets were generated by assuming that the input data measured for sample MA2-3 could be characterized by a set of mean values, represented by the measured mean, and by

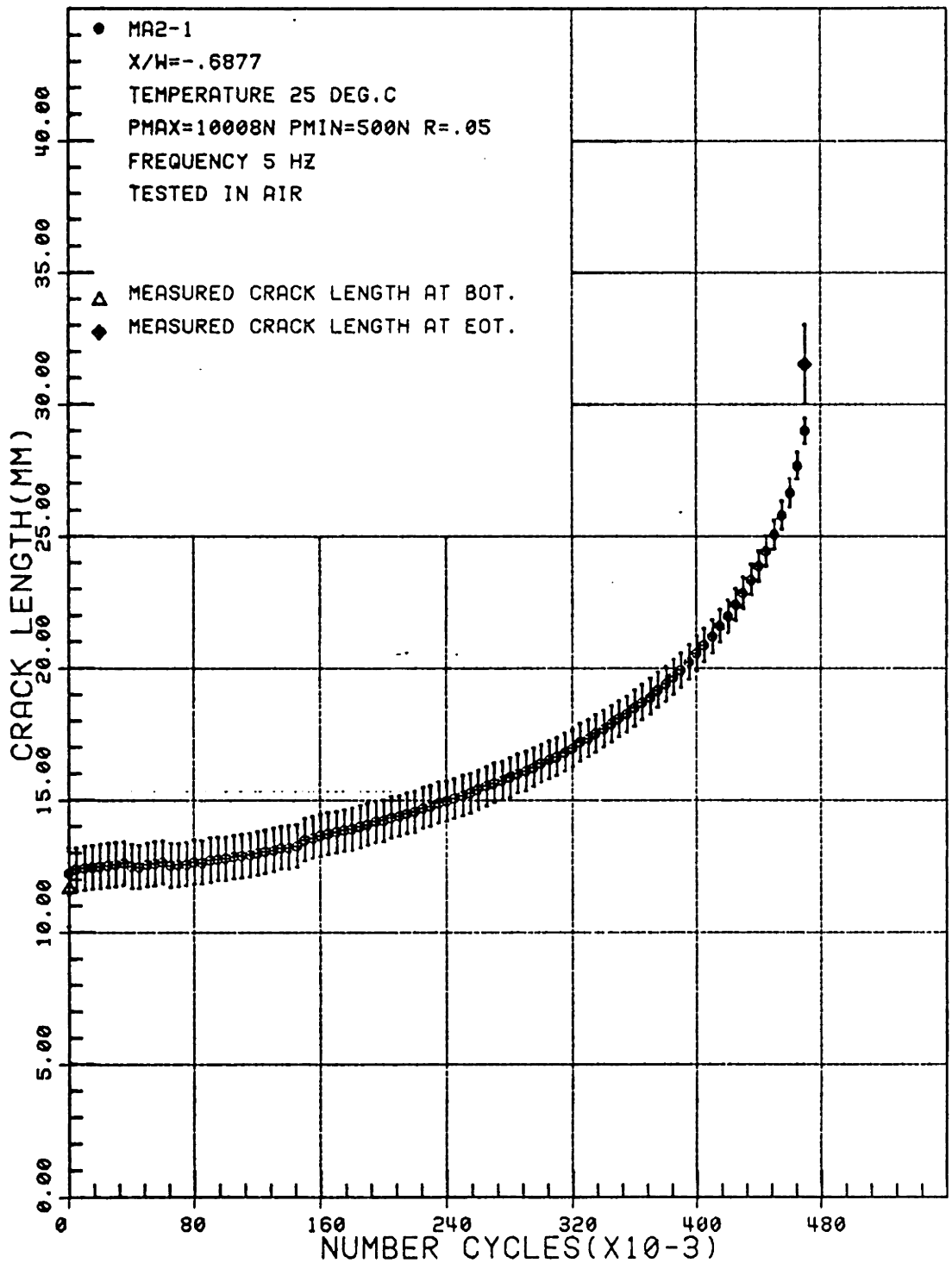

FIGURE 7.1 CRACK LENGTH VS NUMBER OF CYCLES FOR SAMPLE MA2-1. SENSITIZED, TESTED IN AIR.

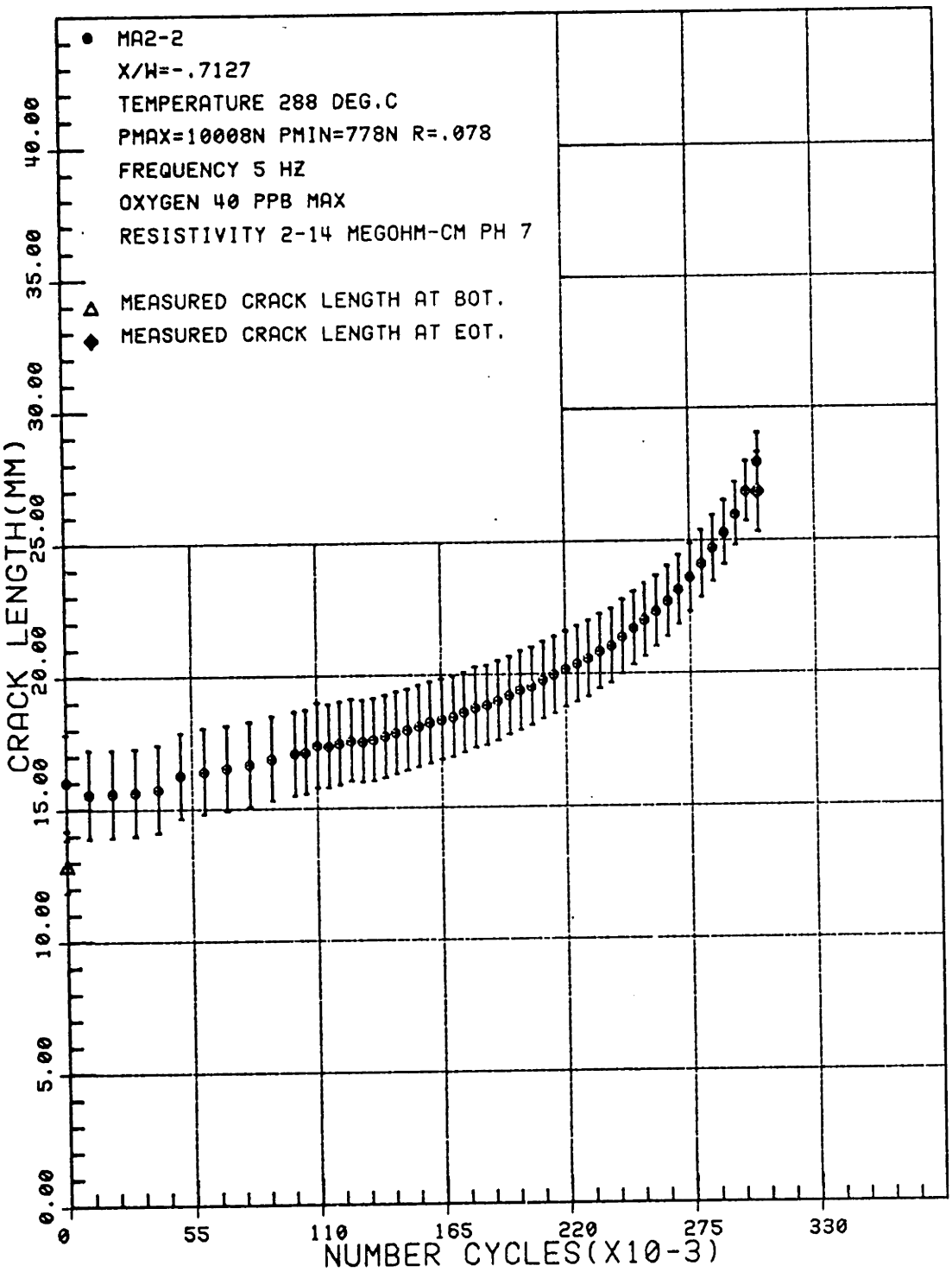

FIGURE 7.2 CRACK LENGTH VS NUMBER OF CYCLES FOR SAMPLE MA2-2. SENSITIZED, TESTED IN HIGH PURITY,DEOXYGENATED WATER AT 288 DEG.C

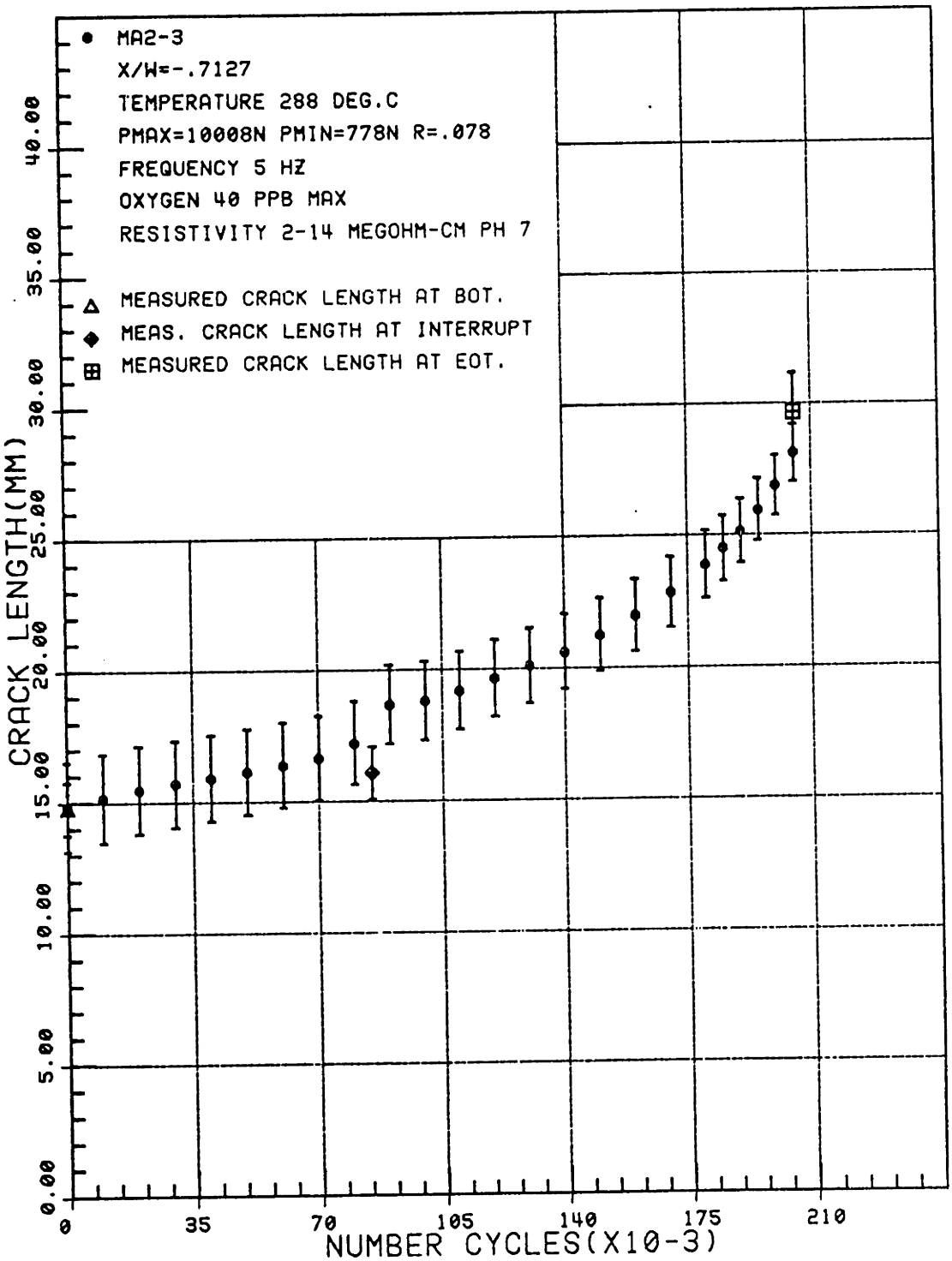

FIGURE 7.3 CRACK LENGTH VS NUMBER OF CYCLES FOR SAMPLE MA2-3. SENSITIZED, TESTED IN HIGH PURITY DEOXYGENATED WATER AT 288 DEG.C

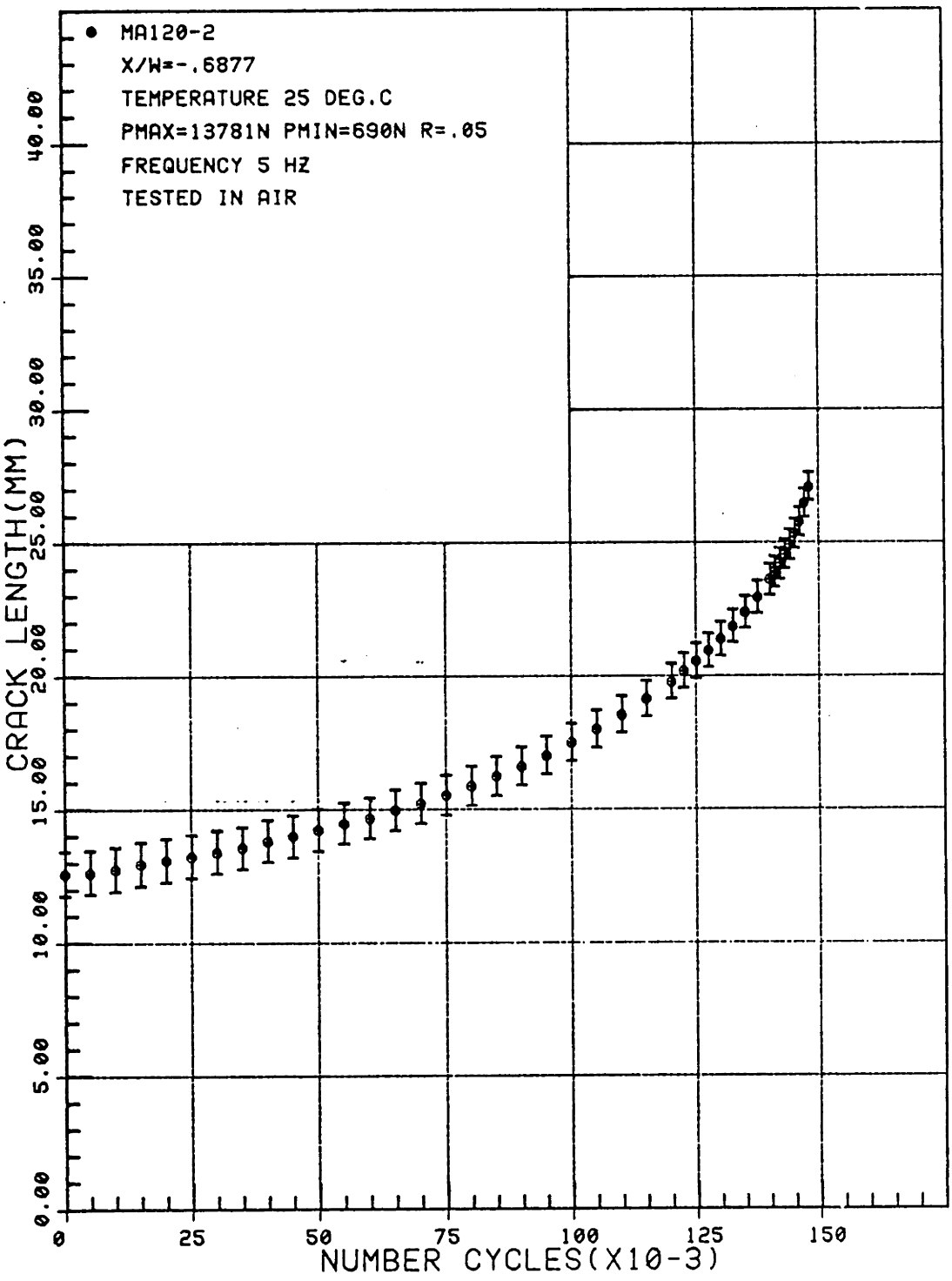

FIGURE 7.4 CRACK LENGTH VS NUMBER OF CYCLES FOR SAMPLE MA120-2. DESENSITIZED, TESTED IN AIR AT 25 DEG.C.

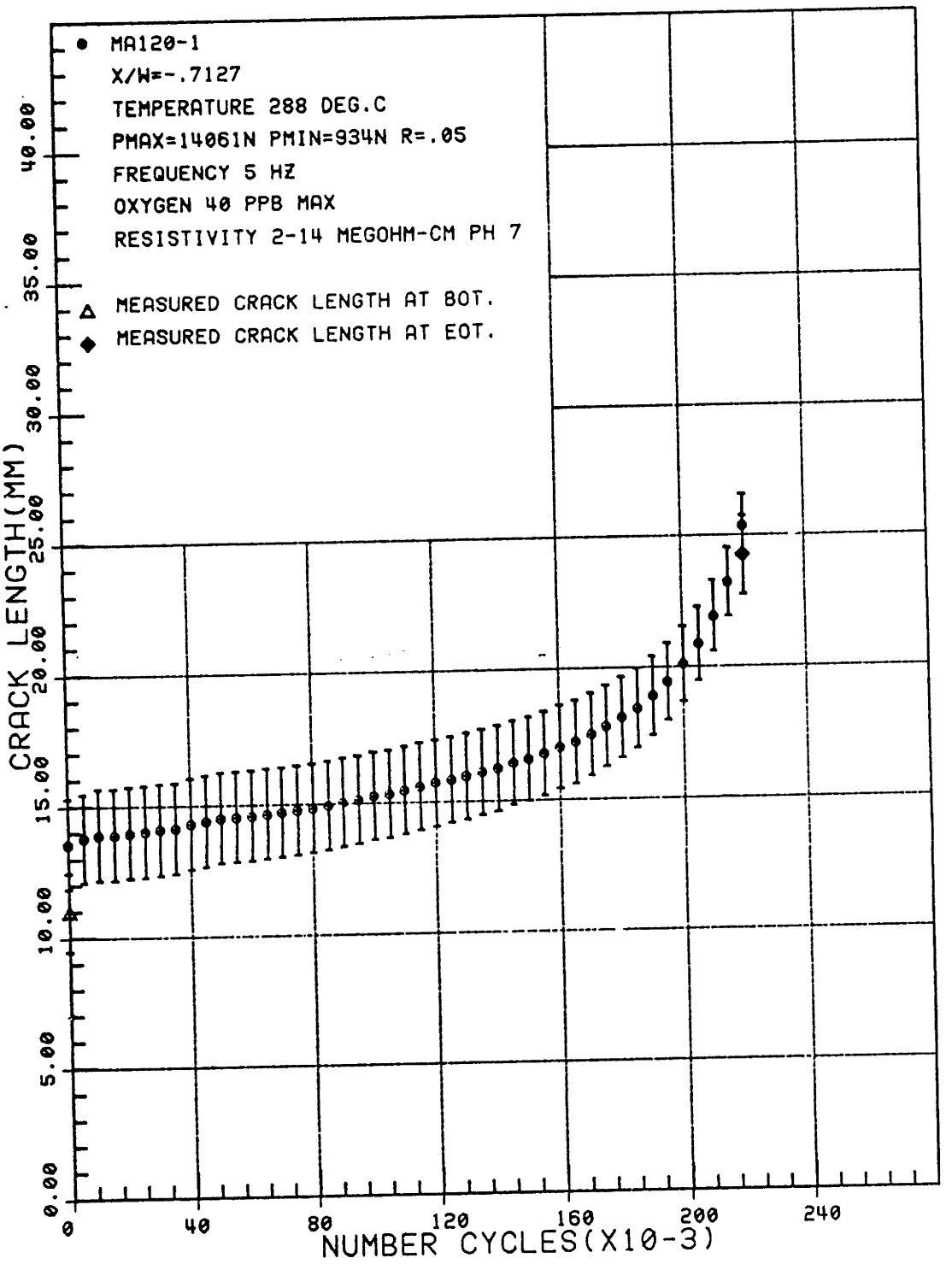

FIGURE 7.5 CRACK LENGTH VS NUMBER OF CYCLES FOR SAMPLE MA120-1. DESENSITIZED, TESTED IN HIGH PURITY DEOXYGENATED WATER AT 288 DEG.C.

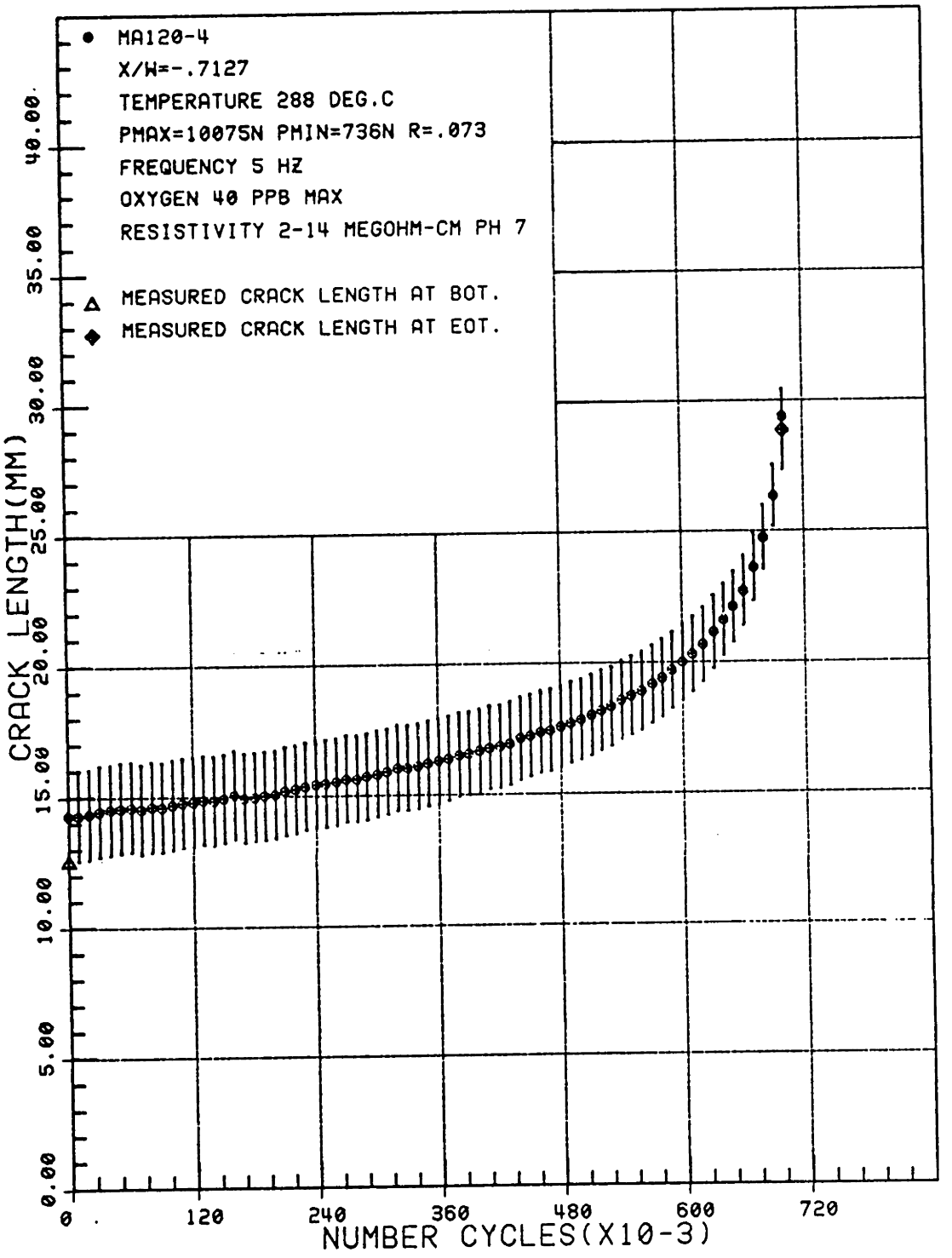

FIGURE 7.6 CRACK LENGTH VS NUMBER OF CYCLES FOR SAMPLE MA120-4. DESENSITIZED, TESTED IN HIGH PURITY DEOXYGENATED WATER AT 288 DEG.C

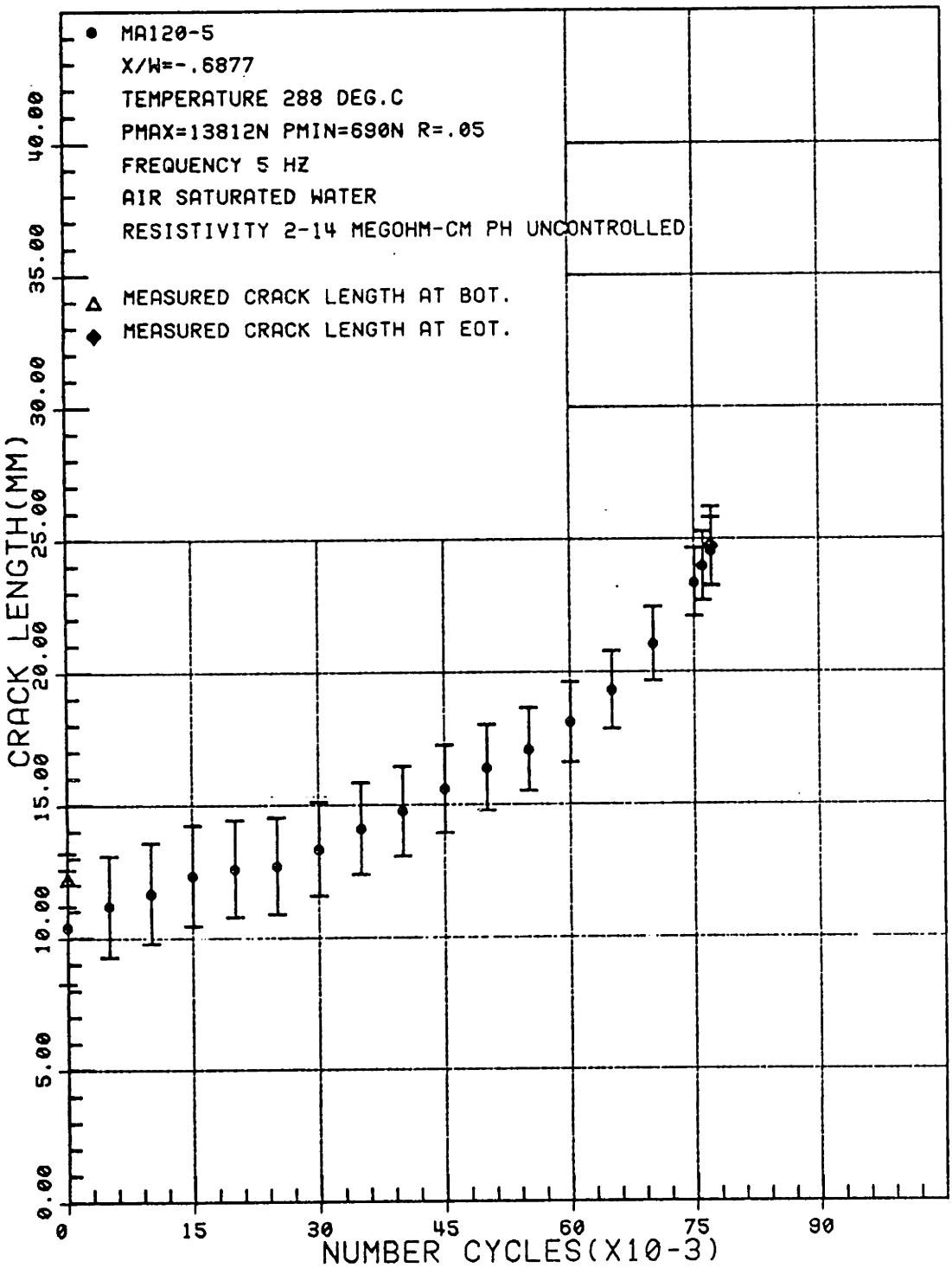

FIGURE 7.7 CRACK LENGTH VS NUMBER OF CYCLES FOR SAMPLE MA120-5. DESENSITIZED, TESTED IN HIGH PURITY AIR SATURATED WATER AT 288 DEG.C.

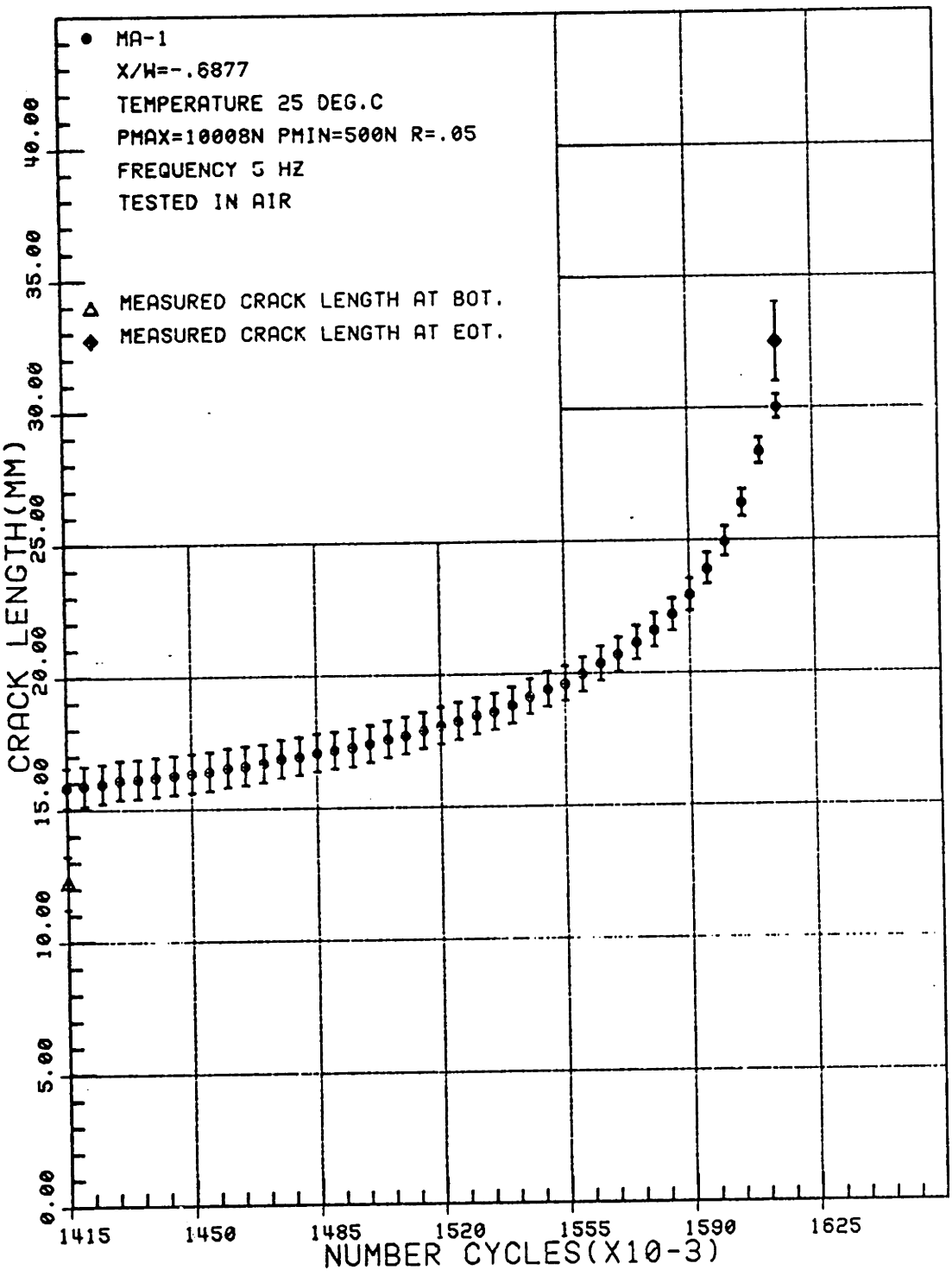

FIGURE 7.8 CRACK LENGTH VS NUMBER OF CYCLES FOR SAMPLE MA-1 MILL ANNEALED. TESTED IN AIR AT 25 DEG.C.

Table 7.1

Measured and Calculated

Crack Length Data

Sample Number	Measured BOT (mm) [1]	Calculated BOT (mm)	Measured EOT (mm) [2]	Calculated EOT (mm)
MA2-1	11.7 ± 1.5	12.2 ± .8	31.5 ± 1.5	28.9 ± .5
MA2-2	12.9 ± 1.5	16.0 ± 2	26.8 ± 1.5	27.9 ± 1.1
MA2-3	14.8 ± 1.0	14.8 ± 1.7	29.6 ± 1.5	28.1 ± 1.1
MA2-3*	16.0 ± 1.0	16.6 ± 1.6		
MA120-1	11.0 ± 1.0	13.6 ± 1.7	24.2 ± 1.5	25.4 ± 1.2
MA120-2	Not Measured			
MA120-4	12.6 ± 1.0	14.3 ± 1.7	28.8 ± 1.5	29.3 ± 1.0
MA120-5	12.2 ± 1.0	10.4 ± 2.0	24.7 ± 1.5	24.5 ± 1.3
MA-1	12.2 ± 1.0	11.2 ± .9	32.5 ± 1.5	30.0 ± .4

1 Beginning of Test

2 End of Test

* Intermediate Point From Interrupted Test

a gausian distribution about each mean value, characterized by the measured values of the input data variances. Table 7.2 lists the base values for the relevant primary data. Column 2 of Table 7.3 shows the base values for the COD measurements during the test.

With the assumption of gausian errors discussed above, ten sets of data were generated using a gausian random number generator to sample each variable. The ten data sets thus produced were then analyzed using the same analytical techniques as were used in the real data but with zero uncertainty assumed. The resulting data consisted of ten sets of crack length vs cycles information. These data were then compared with the actual measured data and calculated uncertainties. The results of this analysis are plotted in Figure 7.9. Table 7.3 and 7.4 show the values for the input used.

7.1.3 Crack Growth Rate Data

The crack length data presented above were reduced using the analytical techniques described in Section 6. The results are presented in Figures 7.10 - 7.25. Figures 7.10 - 7.15 show the results for the material aged for 2 hours at 700°C. Figures 7.16 - 7.21 show the results for the material aged for 120 hours at 700°C. Figures 7.22 - 7.25 show results for additional tests not included in the original test matrix. Figures 7.22 - 7.23 show results for the as received mill annealed material and Figures 7.24 - 7.25 show

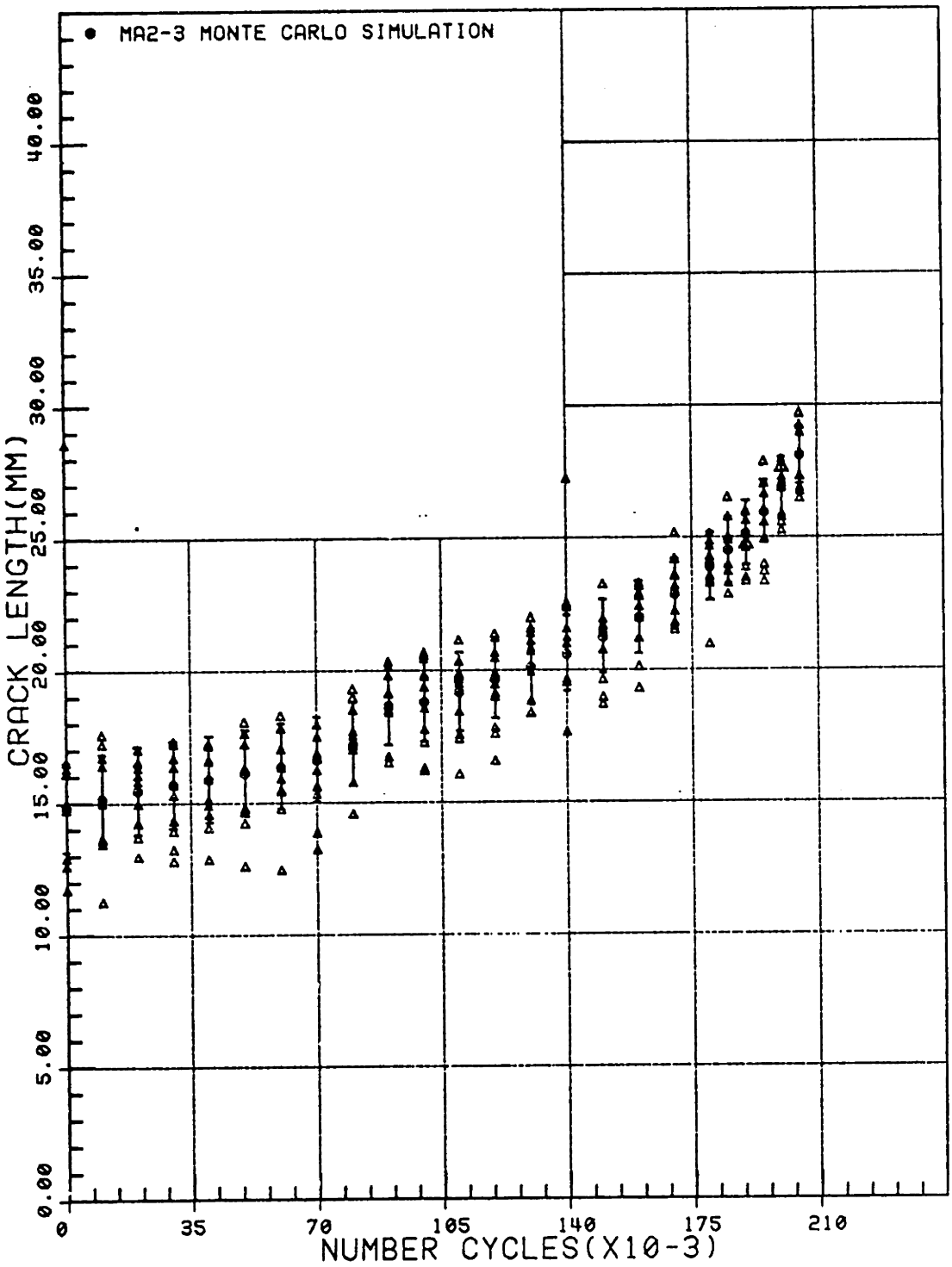

FIGURE 7.9 RESULTS OF MONTE CARLO SIMULATION OF SAMPLE MA2-3.

Table 7.2

Base Values of Primary Data
For Monte Carlo Simulation
of Sample MA2-3

Parameter	Mean Value	Uncertainty
Sample ID	MA2-3	
COD Gauge Constant	.05207 mm/volt	.00355 mm/volt
Specimen Thickness	11.68 mm	.0127 mm
Specimen Width	50.8 mm	.127 mm
Elastic Modulus	1.89655×10^5 MPa	10342 MPa
Load Uncertainty		222 N
Maximum Test Load	10008 N	222 N
Mimimum Test Load	778 N	222 N

Table 7.3

COD Measurements Used For Monte Carlo

Simulation of Sample MA2-3

# Cycles	Base DCOD (Volts)	Base UDCOD (Volts)	#1 DCOD (Volts)	#2 DCOD (Volts)	#3 DCOD (Volts)	#4 DCOD (Volts)
0.0	1.7433	0.0030	1.7414	1.7391	1.7411	1.7438
10000.0	1.7762	0.0034	1.7726	1.7780	1.7798	1.7788
20000.0	1.8080	0.0056	1.8073	1.8105	1.8037	1.8119
30000.0	1.8327	0.0017	1.8326	1.8330	1.8318	1.8330
40000.0	1.8555	0.0041	1.8553	1.8504	1.8597	1.8575
50000.0	1.8810	0.0014	1.8817	1.8819	1.8823	1.8790
60000.0	1.9090	0.0022	1.9090	1.9076	1.9066	1.9089
70000.0	1.9402	0.0015	1.9412	1.9377	1.9394	1.9414
80000.0	2.0085	0.0047	2.0079	2.0104	2.0037	2.0032
90000.0	2.2007	0.0025	2.2032	2.1998	2.1973	2.2003
100000.0	2.2197	0.0019	2.2192	2.2181	2.2193	2.2201
110000.0	2.2735	0.0059	2.2780	2.2726	2.2788	2.2650
120000.0	2.3420	0.0042	2.3394	2.3434	2.3531	2.3417
130000.0	2.4177	0.0061	2.4133	2.4145	2.4225	2.4198
140000.0	2.5017	0.0037	2.5022	2.5102	2.5042	2.5075
150000.0	2.6153	0.0038	2.6088	2.6138	2.6146	2.6188
160000.0	2.7500	0.0022	2.7485	2.7492	2.7498	2.7510
170000.0	2.9278	0.0029	2.9310	2.9238	2.9224	2.9292
180000.0	3.1658	0.0075	3.1665	3.1730	3.1477	3.1645
185000.0	3.3183	0.0090	3.3194	3.3110	3.3125	3.3156
190000.0	3.4903	0.0038	3.4933	3.4953	3.4906	3.4870
195000.0	3.7215	0.0083	3.7367	3.7257	3.7253	3.7214
200000.0	4.0215	0.0055	4.0161	4.0231	4.0211	4.0211
205000.0	4.4707	0.0056	4.4789	4.4684	4.4676	4.4716

Table 7.3
(Cont.)

# Cycles	#5 DCOD (Volts)	#6 DCOD (Volts)	#7 DCOD (Volts)	#8 DCOD (Volts)	#9 DCOD (Volts)	#10 DCOD (Volts)
0.0	1.7429	1.7449	1.7440	1.7408	1.7477	1.7453
10000.0	1.7782	1.7792	1.7771	1.7739	1.7744	1.7694
20000.0	1.8102	1.8107	1.8086	1.8059	1.7968	1.8095
30000.0	1.8326	1.8300	1.8353	1.8360	1.8325	1.8342
40000.0	1.8593	1.8616	1.8557	1.8618	1.8554	1.8586
50000.0	1.8800	1.8832	1.8800	1.8804	1.8800	1.8825
60000.0	1.9074	1.9054	1.9114	1.9079	1.9072	1.9113
70000.0	1.9416	1.9402	1.9387	1.9393	1.9424	1.9424
80000.0	2.0056	2.0044	2.0090	2.0103	2.0138	2.0147
90000.0	2.2014	2.1968	2.1982	2.1998	2.2013	2.2015
100000.0	2.2212	2.2226	2.2213	2.2227	2.2217	2.2207
110000.0	2.2616	2.2713	2.2783	2.2823	2.2746	2.2744
120000.0	3.3439	2.3481	2.3388	2.3472	2.3348	2.3401
130000.0	2.4333	2.4294	2.4144	2.4178	2.4069	2.4205
140000.0	2.5041	2.5026	2.5023	2.4986	2.4992	2.5015
150000.0	2.6230	2.6082	2.6193	2.6183	2.6122	2.6215
160000.0	2.7528	2.7459	2.7531	2.7474	2.7535	2.7506
170000.0	2.9240	2.9303	2.9255	2.9235	2.9328	2.9267
180000.0	3.1667	3.1595	3.1617	3.1822	3.1694	3.1624
185000.0	3.3060	3.3287	3.3188	3.3096	3.3242	3.3155
190000.0	3.4944	3.4924	3.4882	3.4879	3.4959	3.4891
195000.0	3.7333	3.7205	3.7408	3.7325	3.7233	3.7264
200000.0	4.0183	4.0295	4.0215	4.0146	4.0065	4.0211
205000.0	4.4706	4.4641	4.4649	4.4673	4.4772	4.4680

Table 7.4

Monte Carlo Generated Input Parameters For

Simulations of Sample MA2-3

Test #	COD Gauge Constant (mm/volt)	Specimen Thickness (mm)	Specimen Width (mm)	Elastic Modulus (MPa)	Maximum Load (N)	Minimum Load (N)
1	.05263	11.682	50.82	190513	9979	749
2	.04760	11.664	50.64	199428	10130	900
3	.05171	11.678	50.79	173061	9802	518
4	.05264	11.682	50.82	159879	9606	406
5	.05267	11.682	50.82	201054	10301	1071
6	.04927	11.670	50.69	184976	9944	714
7	.05573	11.693	50.93	176782	10680	1450
8	.05470	11.689	50.89	189120	9928	699
9	.05445	11.690	50.88	197681	10260	1030
10	.05194	11.679	50.79	200979	9869	639

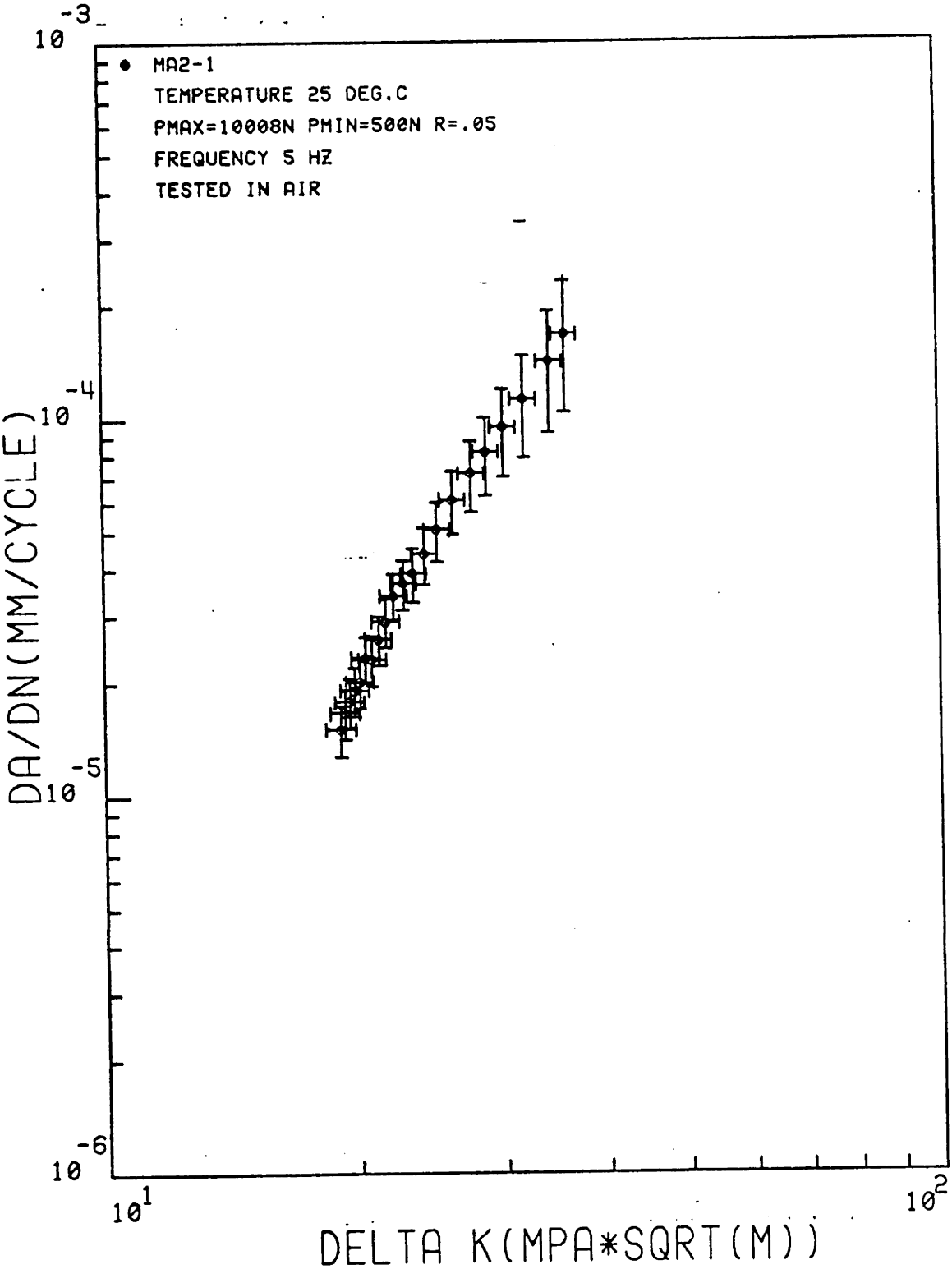

FIGURE 7.10 CRACK GROWTH RATE DATA FOR SAMPLE MA2-1, SENSITIZED. TESTED IN AIR AT 25 DEG.C. ERROR IN DA/DN BASED ON REGRESSION FIT TO PARIS LAW.

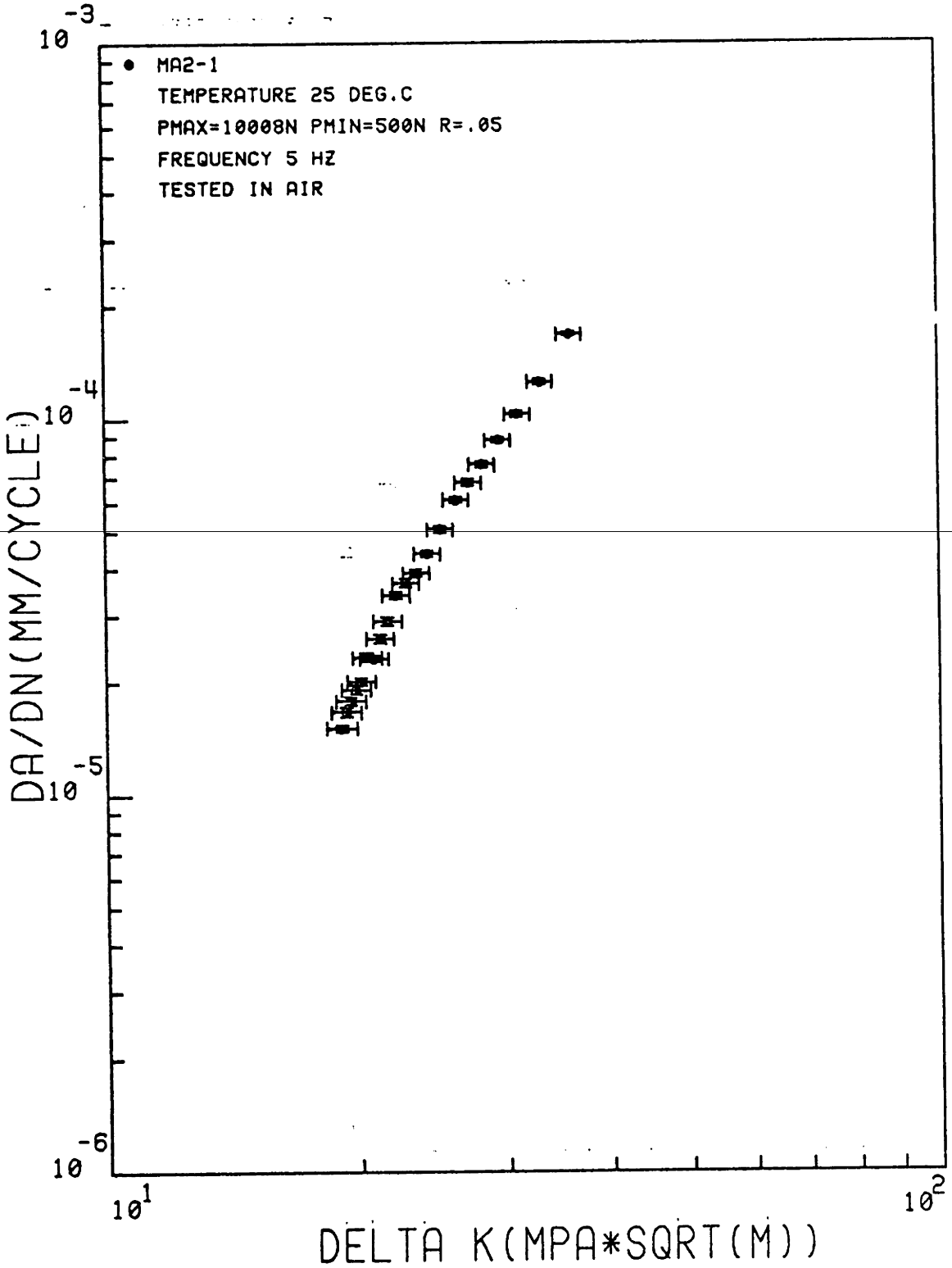

FIGURE 7.11 CRACK GROWTH RATE DATA FOR SAMPLE MA2-1, SENSITIZED. TESTED IN AIR AT 25 DEG.C. ERROR IN DA/DN BASED ON ERRORS IN CRACK LENGTH INTERVAL.

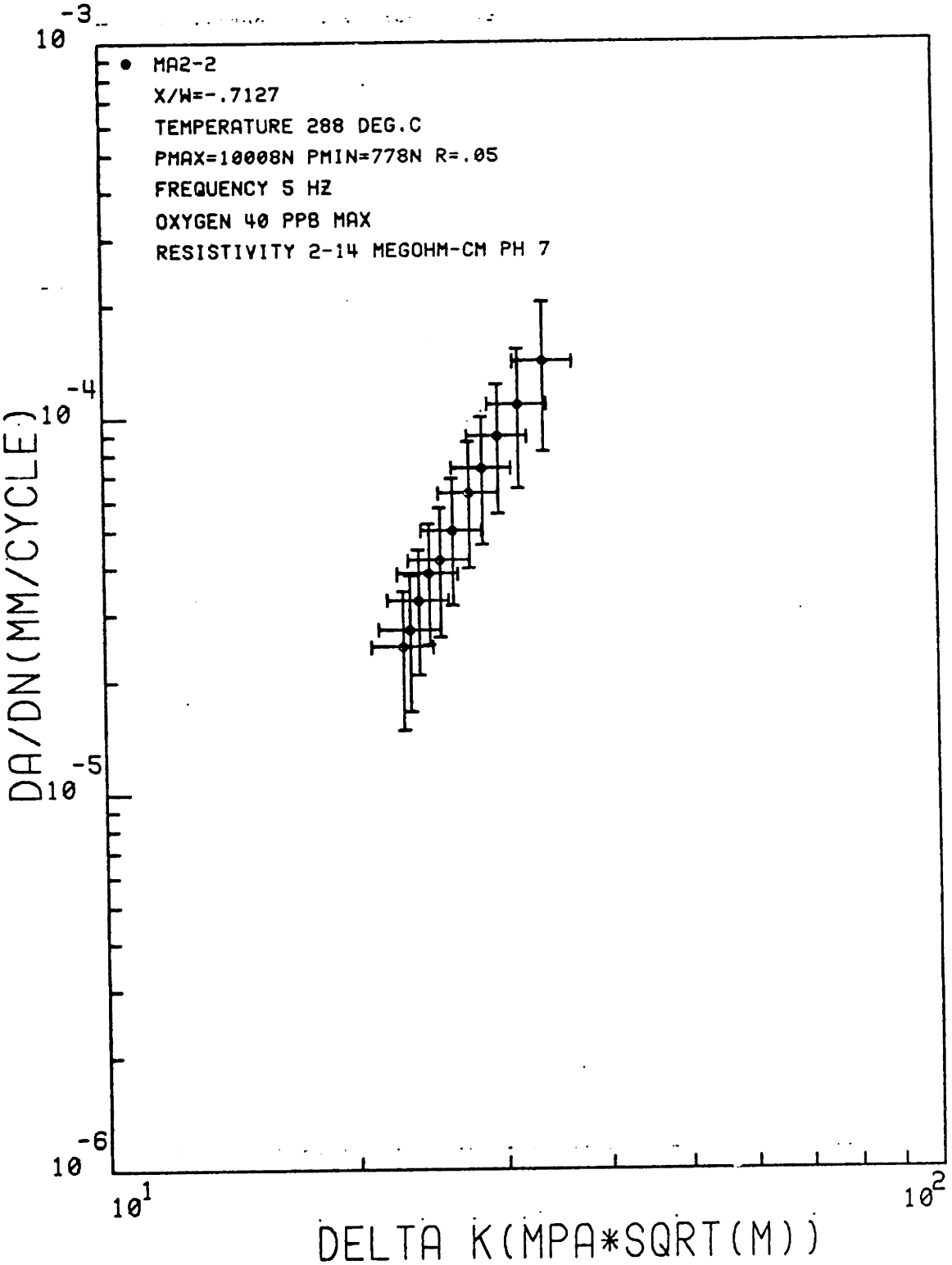

FIGURE 7.12 CRACK GROWTH RATE DATA FOR SAMPLE MA2-2, SENSITIZED. TESTED IN HIGH PURITY DEOXYGENATED WATER AT 288 DEG.C. ERROR IN DA/DN BASED ON REGRESSION FIT TO PARIS LAW.

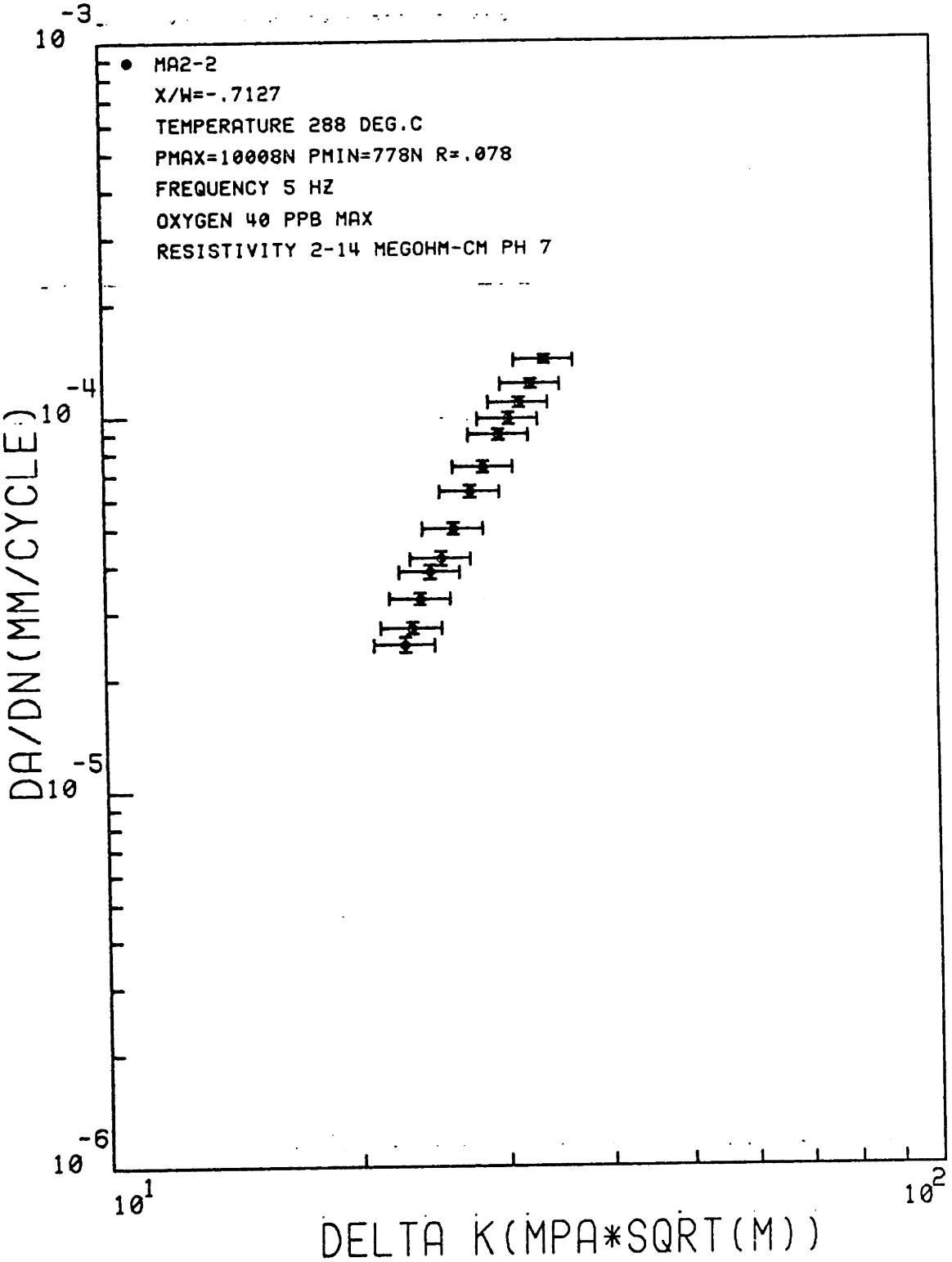

FIGURE 7.13 CRACK GROWTH RATE DATA FOR SAMPLE MA2-2, SENSITIZED. TESTED IN HIGH PURITY DEOXYGENATED WATER AT 288 DEG.C. ERROR IN DA/DN BASED ON ERRORS IN CRACK LENGTH INTERVAL.

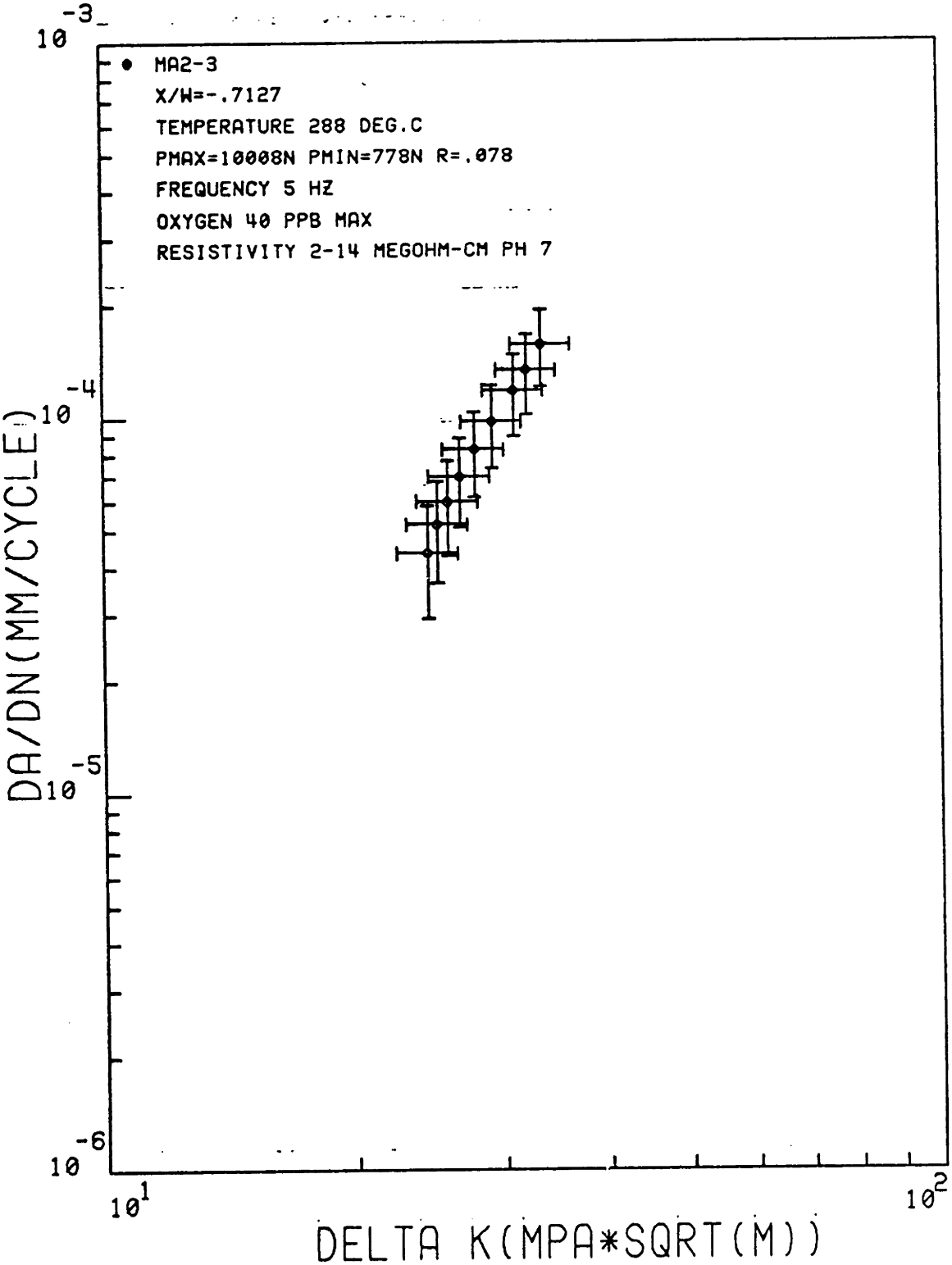

FIGURE 7.14 CRACK GROWTH RATE DATA FOR SAMPLE MA2-3, SENSITIZED. TESTED IN HIGH PURITY DEOXYGENATED WATER AT 288 DEG.C. ERROR IN DA/DN BASED ON REGRESSION FIT TO PARIS LAW.

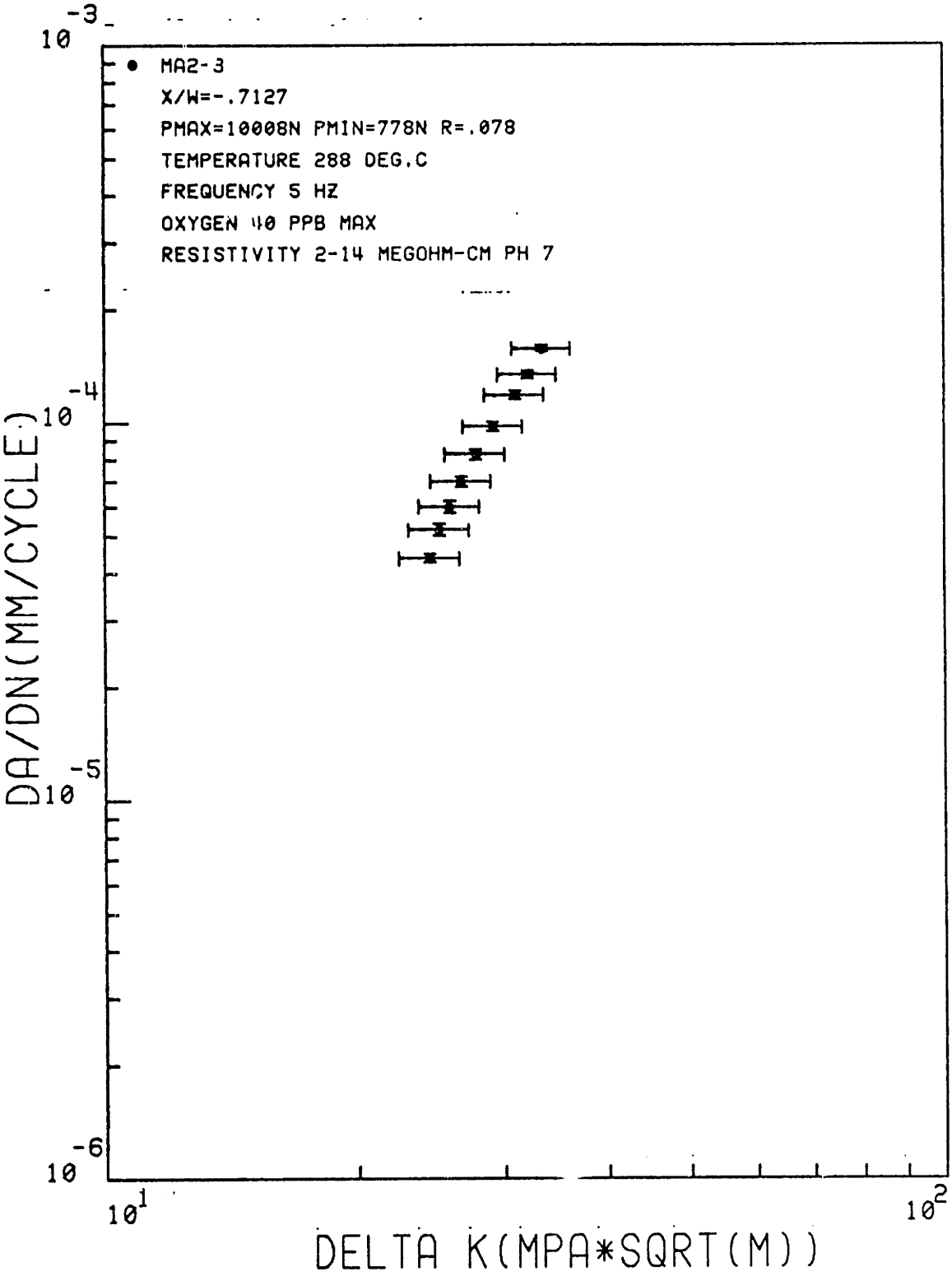

FIGURE 7.15 CRACK GROWTH RATE DATA FOR SAMPLE MA2-3, SENSITIZED. TESTED IN HIGH PURITY DEOXYGENATED WATER AT 288 DEG.C. ERROR IN DA/DN BASED ON ERRORS IN CRACK LENGTH INTERVAL.

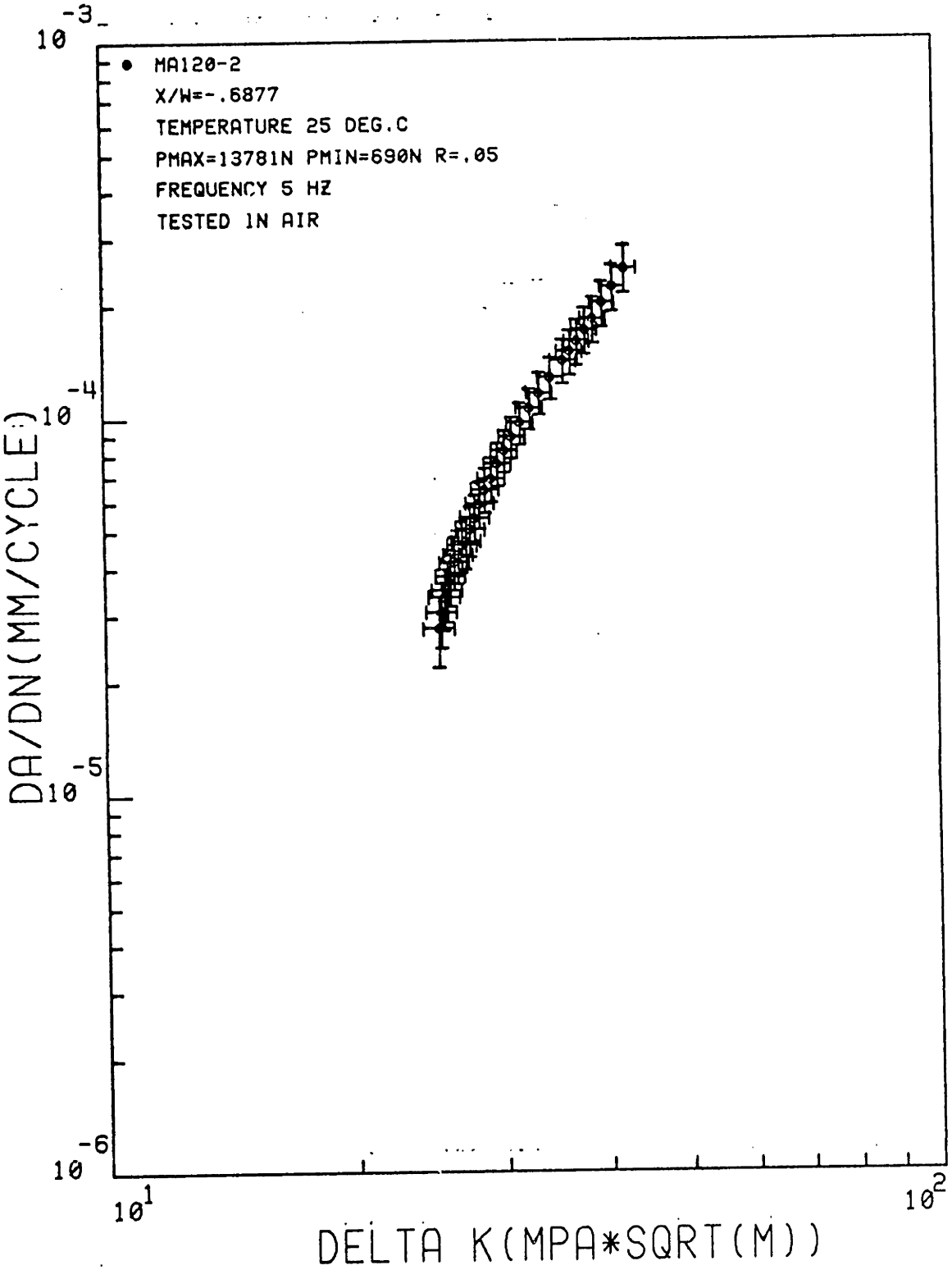

FIGURE 7.16 CRACK GROWTH RATE DATA FOR SAMPLE MA120-2 DESENSITIZED. TESTED IN AIR AT 25 DEG.C. ERROR IN DA/DN BASED ON REGRESSION FIT TO PARIS LAW.

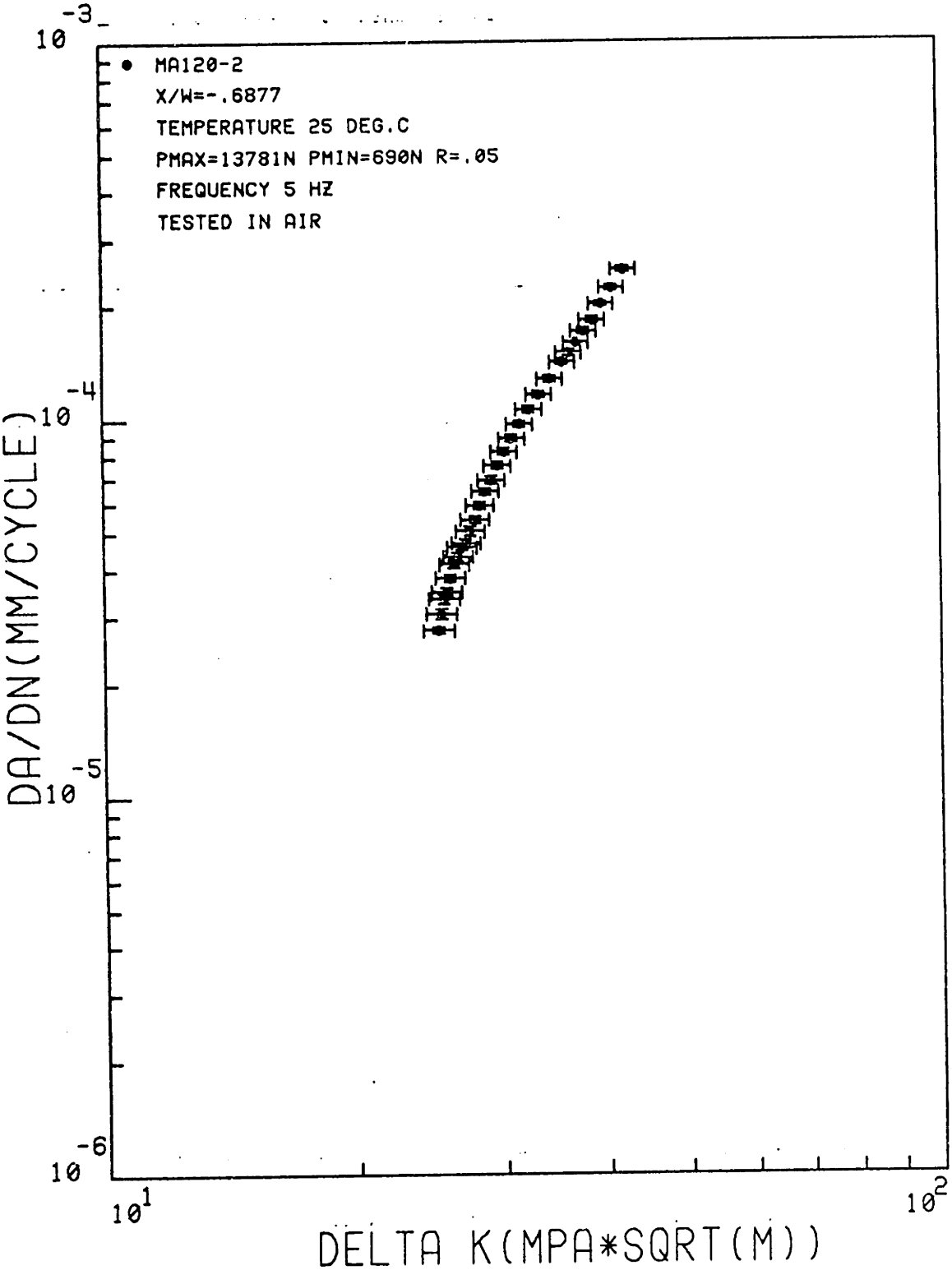

FIGURE 7.17 CRACK GROWTH RATE DATA FOR SAMPLE MA120-2 DESENSITIZED. TESTED IN AIR AT 25 DEG.C. ERROR IN DA/DN BASED ON ERRORS IN CRACK LENGTH INTERVAL.

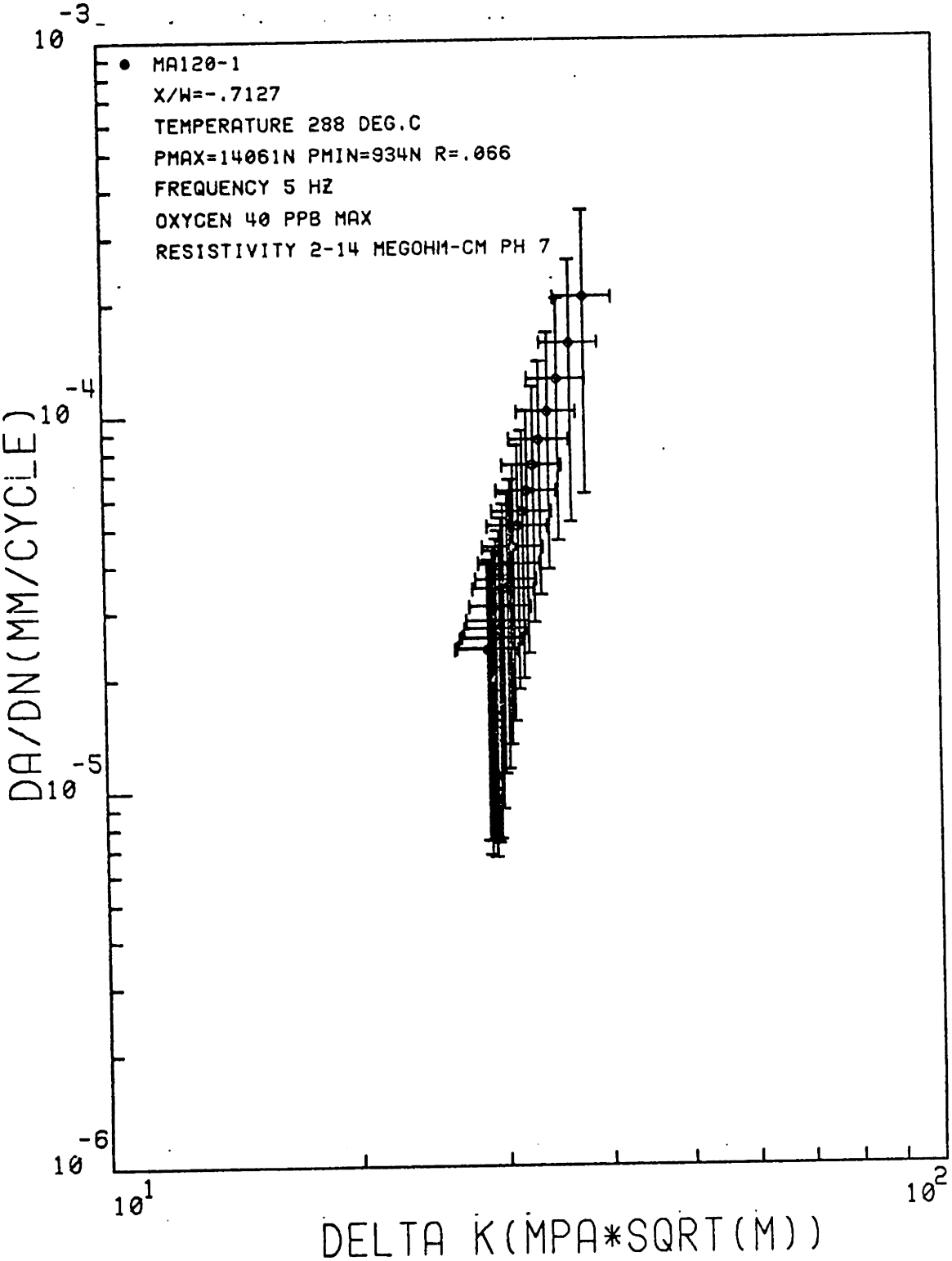

FIGURE 7.18 CRACK GROWTH RATE DATA FOR SAMPLE MA120-1, DESENSITIZED TESTED IN HIGH PURITY DEOXYGENATED WATER AT 288 DEG.C. ERROR IN DA/DN BASED ON REGRESSION FIT TO PARIS LAW.

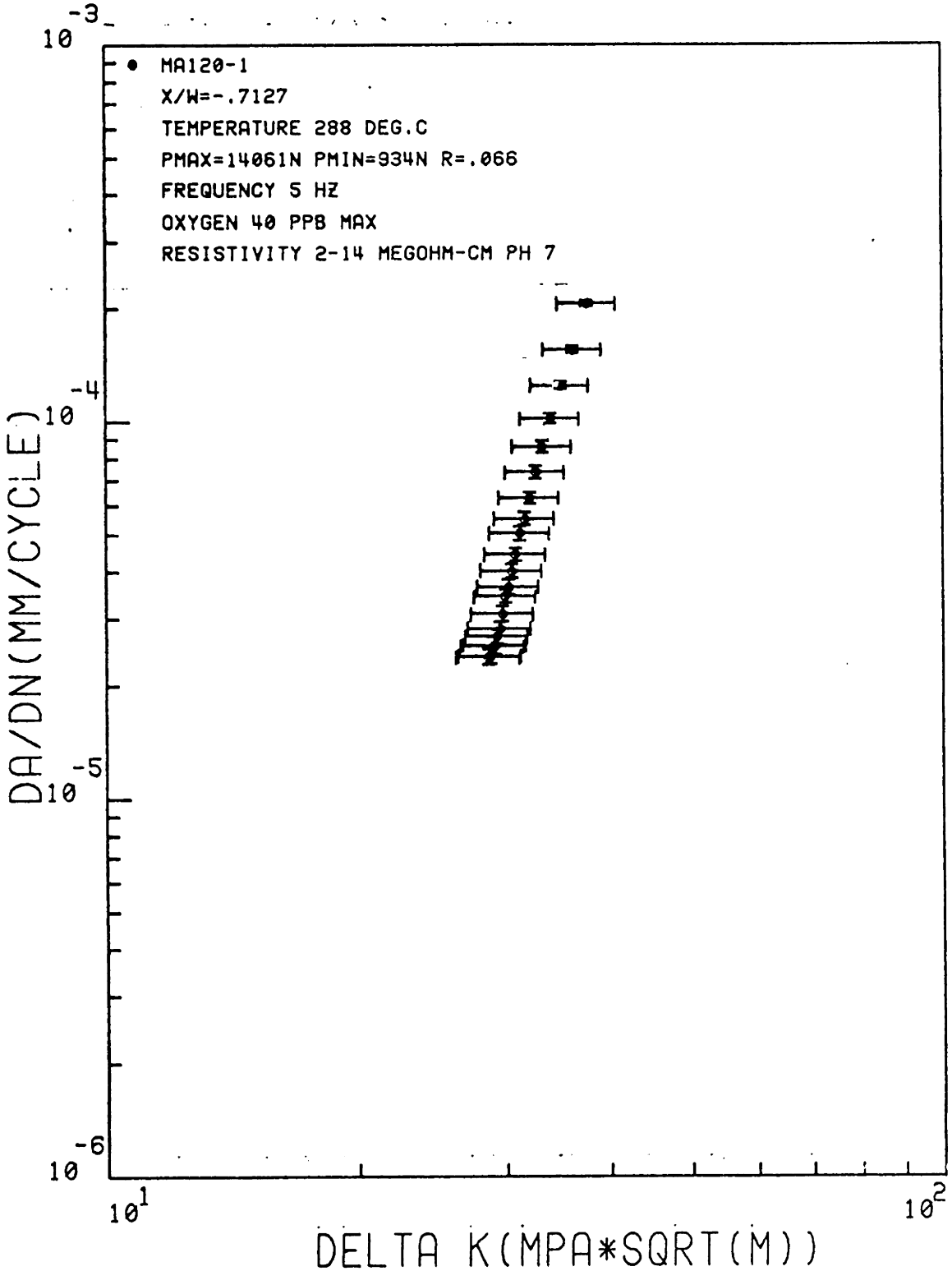

FIGURE 7.19 CRACK GROWTH RATE DATA FOR SAMPLE MA120-1, DESENSITIZED. TESTED IN HIGH PURITY DEOXYGENATED WATER AT 288 DEG.C. ERROR IN DA/DN BASED ON ERRORS IN CRACK LENGTH INTERVAL.

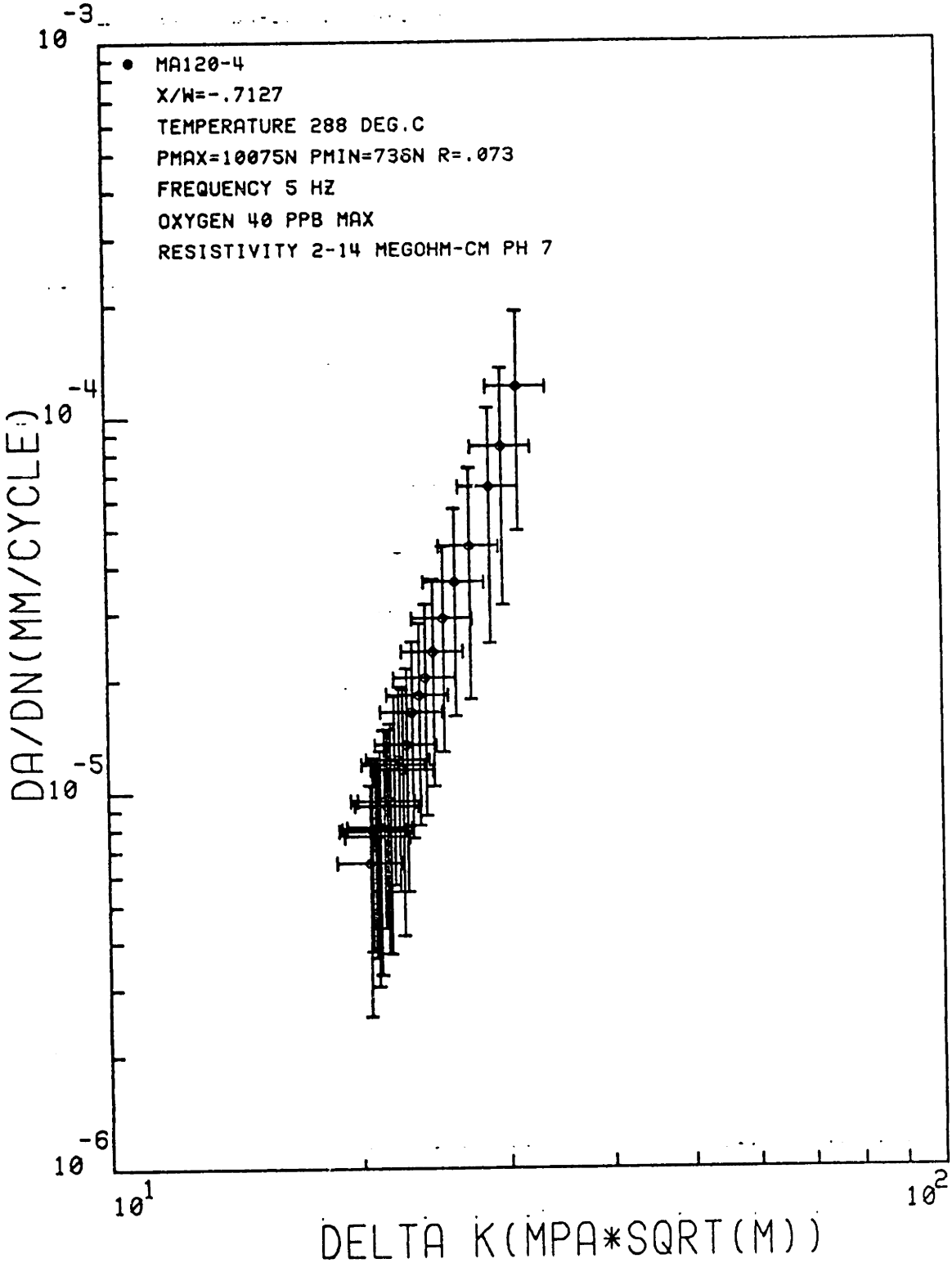

FIGURE 7.20 CRACK GROWTH RATE DATA FOR SAMPLE MA120-4, DESENSITIZED. TESTED IN HIGH PURITY DEOXYEGNATED WATER AT 288 DEG.C. ERROR IN DA/DN BASED ON REGRESSION FIT TO PARIS LAW.

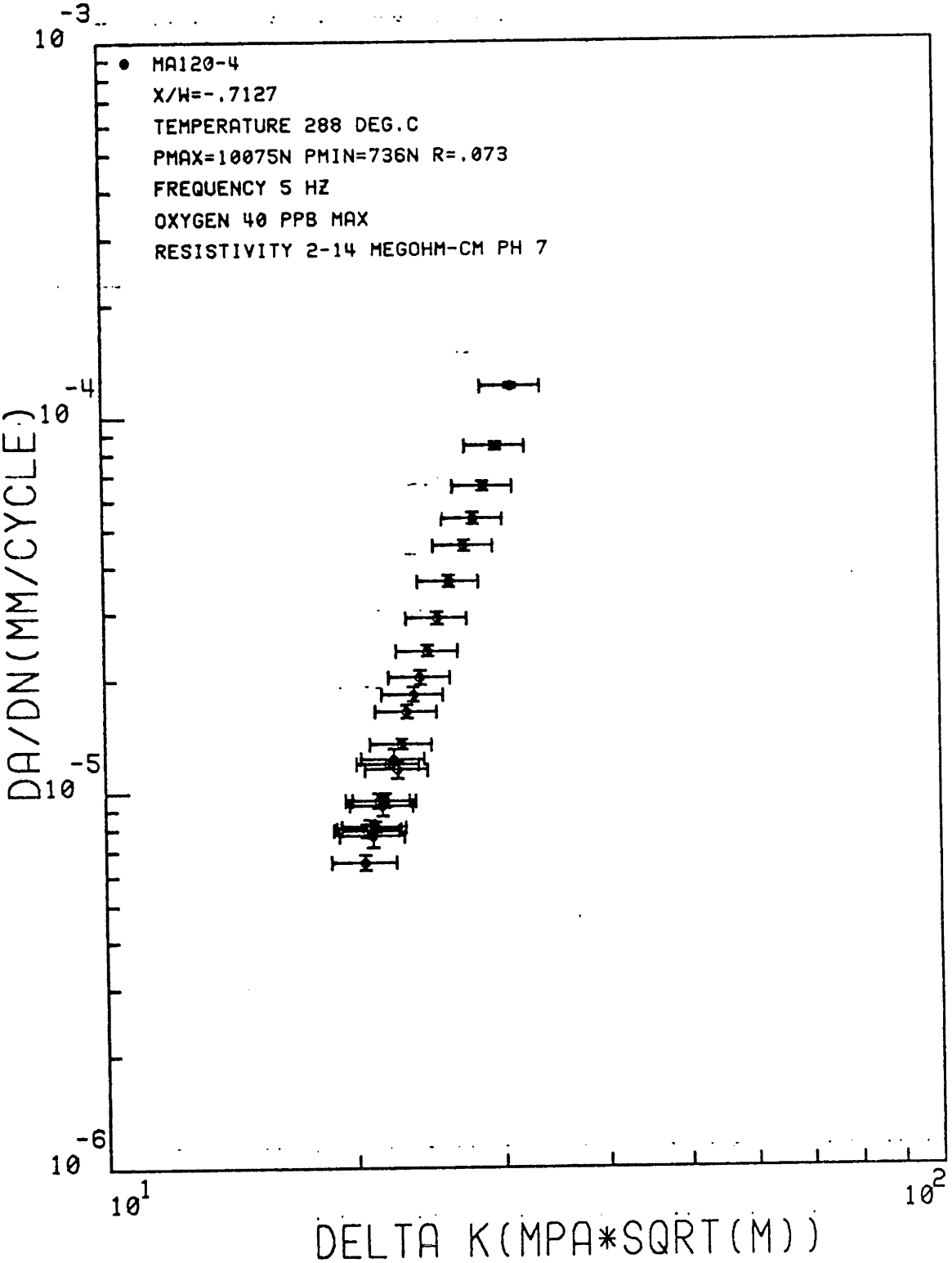

FIGURE 7.21 CRACK GROWTH RATE DATA FOR SAMPLE MA120-4, DESENSITIZED. TESTED IN HIGH PURITY DEOXYGENATED WATER AT 288 DEG.C. ERROR IN DA/DN BASED ON ERRORS IN CRACK LENGTH INTERVAL.

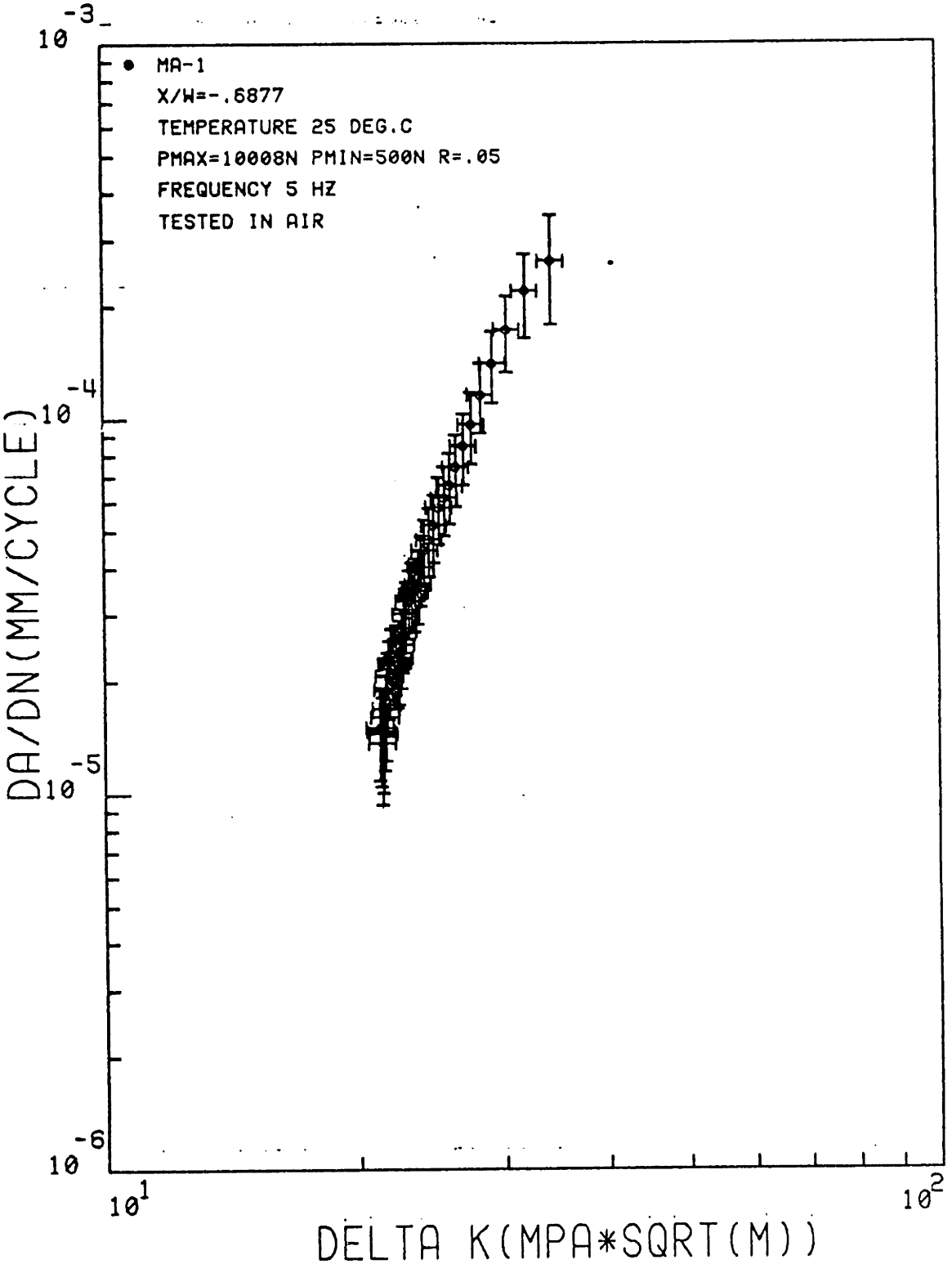

FIGURE 7.22 CRACK GROWTH RATE DATA FOR SAMPLE MA-1, MILL ANNEALED. TESTED IN AIR AT 25 DEG.C. ERROR IN DA/DN BASED ON REGRESSION FIT TO PARIS LAW.

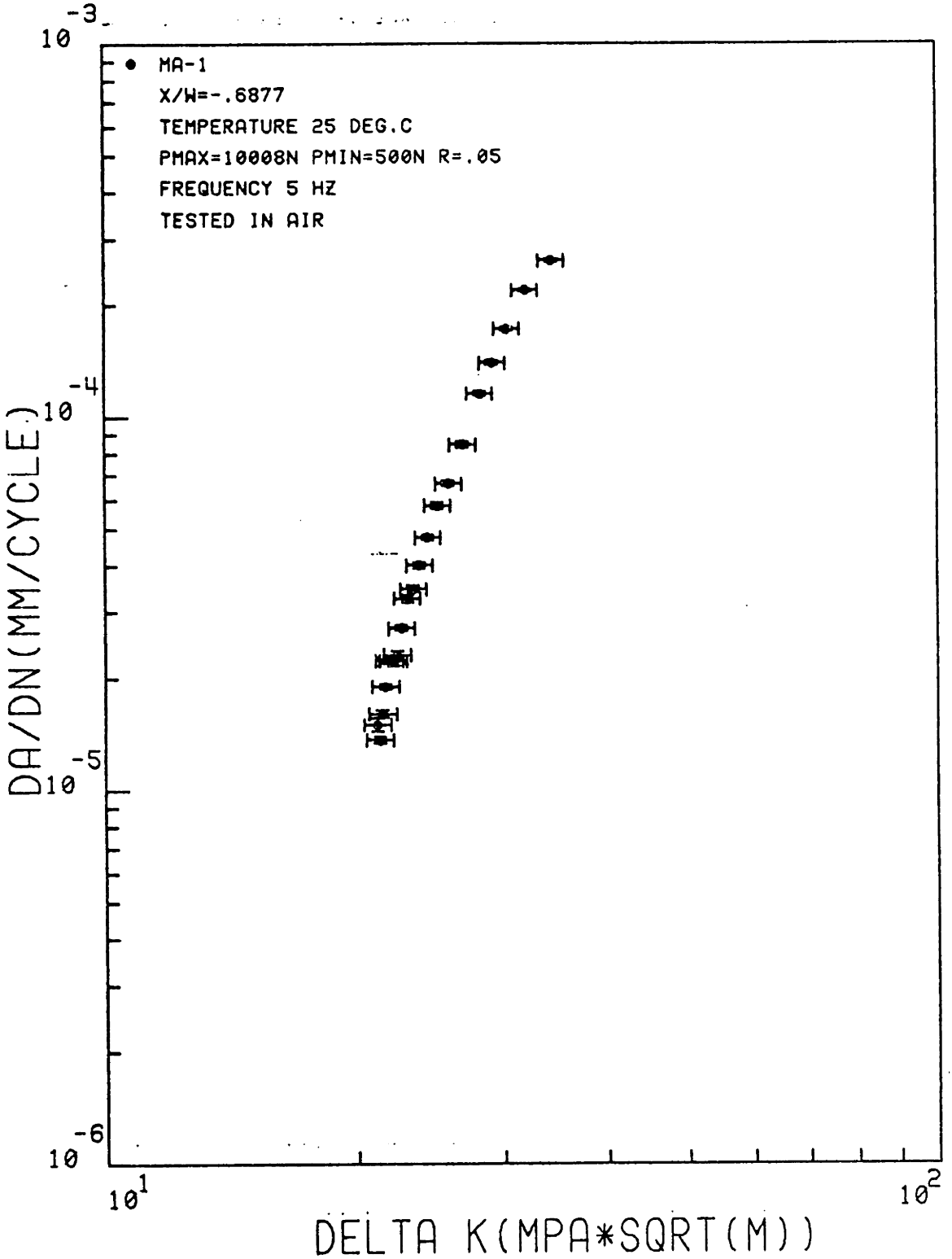

FIGURE 7.23 CRACK GROWTH RATE DATA FOR SAMPLE MA-1, MILL ANNEALED. TESTED IN AIR AT 25 DEG.C. ERROR IN DA/DN BASED ON ERRORS IN CRACK LENGTH INTERVAL.

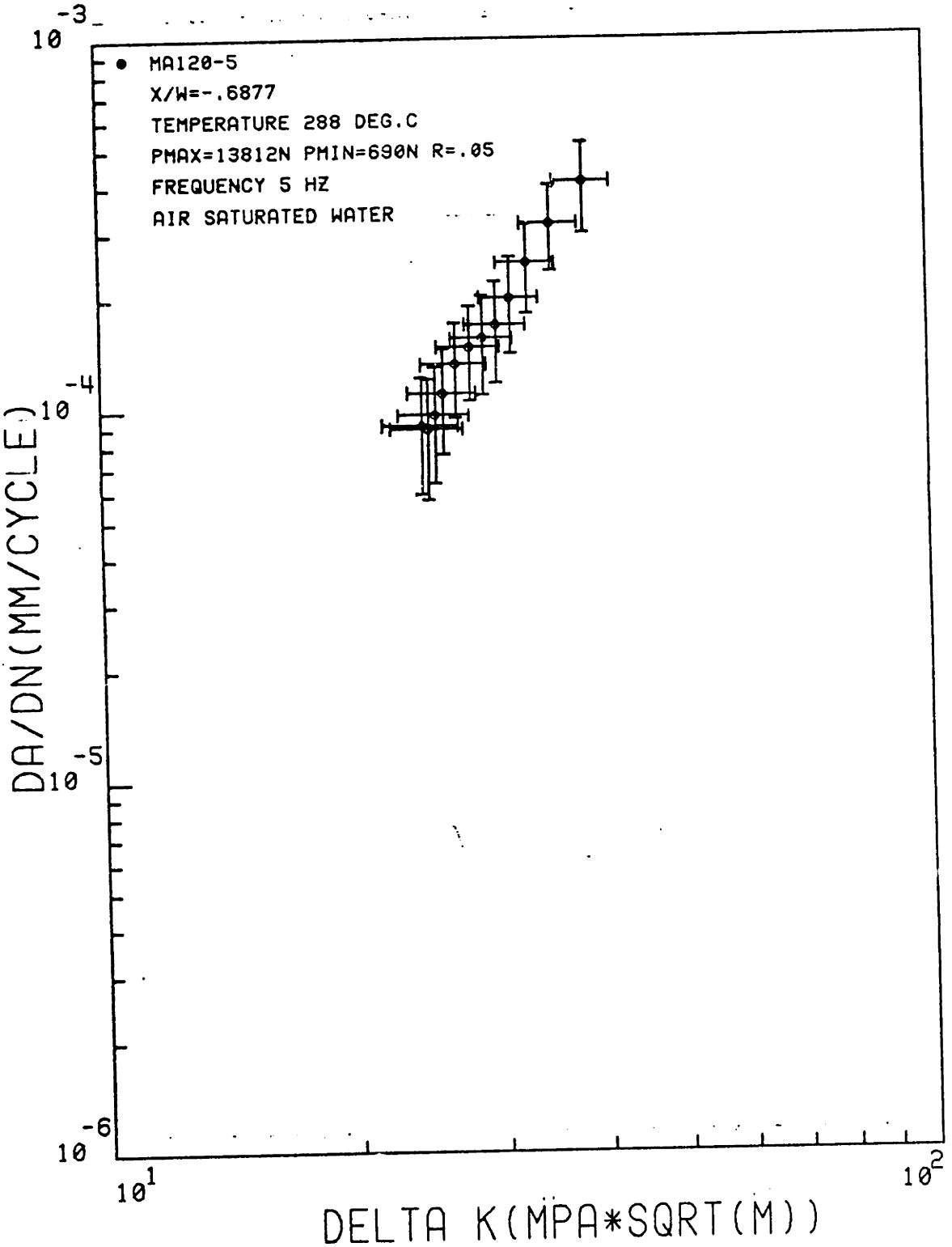

FIGURE 7.24 CRACK GROWTH RATE DATA FOR SAMPLE MA120-5, DESENSITIZED. TESTED IN HIGH PURITY AIR SATURATED WATER AT 288 DEG.C. ERROR IN DA/DN BASED ON REGRESSION FIT TO PARIS LAW

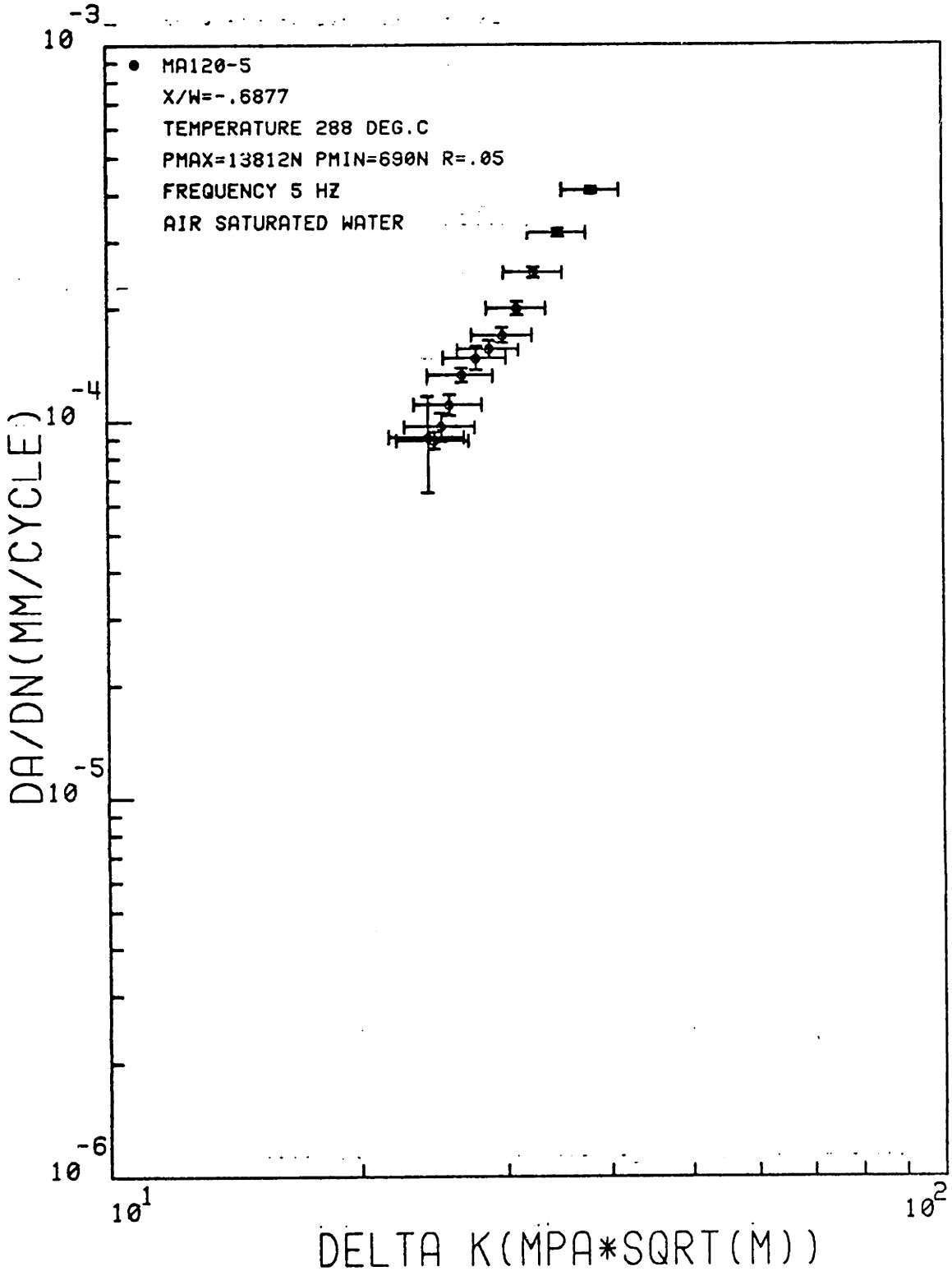

FIGURE 7.25 CRACK GROWTH RATE DATA FOR SAMPLE MA120-5, DESENSITIZED. TESTED IN HIGH PURITY AIR SATURATED WATER AT 288 DEG.C. ERROR IN DA/DN BASED ON ERRORS IN CRACK LENGTH INTERVAL.

results for a sample aged at 700°C for 120 hours and tested in high purity air saturated water.

The crack growth rate data for each test is plotted in two ways. The first plot for each sample shows error bars on crack growth rate calculated using equation 6.44 based on a regression fit of the data to an equation of the form derived using equations 6.39 - 6.43. The second plot for each sample shows error bars based on analysis using equation 6.47 and assuming a correlation of 95% between errors at the end points of each crack length measurement interval. The value of 95% correlation was chosen assuming that this represented the highest correlation which could be expected.

7.2 Discussion of Results

The results of the experimental program were compared with available data from other investigators. Data available for comparison was limited but general comparisons were still possible. Comparisons were made at two points: (1) the crack growth rate data itself, and (2) fractography.

The general results were found to be internally consistent; duplicate specimens produced comparable results, and consistent with the findings of other investigators. Fractographic analysis of crack surfaces compared favorably with that of other investigators.

The results of the Monte Carlo simulation studies support the appropriateness of the general analytical methods.

7.2.1 Discussion: Crack Length Measurements

The calculated crack lengths for the experimental program are consistent with measured values. Of a total of 15 measured crack lengths for comparison, 10 or 67% were found to be within the calculated uncertainty on crack length. The error bars plotted in Figures 7.1 - 7.8 are for a 68% confidence interval. Thus one would expect that data would be outside these bounds approximately 32% of the time. This is indeed the case. Additional confirmation of the consistency of the analytical techniques is provided by the results of the Monte Carlo simulation presented in Figure 7.9. The same criteria concerning the confidence interval applies in this case and the results of the analysis are consistent with these criteria. Based on these two pieces of analysis, the conclusion can be drawn that the analytical techniques for determining crack length are consistent with the experimental data and thus are usable for the acquisition and reduction of the data.

7.2.2 Discussion: Crack Growth Rate Data

7.2.2.1 Data Presentation

As discussed earlier, the crack growth rate data can be plotted in two ways depending on the technique used to determine the estimated error on da/dn. Both techniques can provide valuable information.

The uncertainties calculated using equation 6.44 came

with the assumption that the crack growth rate is a function only of ΔK. If this is true and the fit to equation 6.39 is perfect, as would be indicated by a goodness of fit parameter, equation 6.43, equal to one, then the dependence on ΔK implies a dependence on the crack extension interval. This implicit dependence on Δa is derived from the fact the variance on da/dn calculated in equation 6.44 depends on the increment in ΔK. Thus there is an implied dependence on Δa for this special case. However, for the case where the crack growth rate is not purely dependent on ΔK, the analysis breaks down. For the case at hand, the assumption of perfect ΔK dependence is not valid. The error bars on da/dn, calculated in the above manner, must thus be viewed as only qualitative.

The second plot for each test shows error bars on da/dn based on equation 6.47. This equation exhibits a more fundamental dependence on crack length and crack length interval. However, the difficulty with this equation is, as pointed out earlier, involves getting at a value for the covariance term. With no information concerning the correlation between errors at the end points of the measurement intervals, the potential error in da/dn can range from zero, with perfect correlation, to a value approximated by the square root of the sum of the squares of the crack length uncertainties, at the end points of the crack length measurement interval. For this investigation, an estimated error on the absolute value of crack length at any given point in time, ranged from

.5 mm for air tests to 2.0 mm for high temperature tests. An error of this magnitude on Δa would lead to the conclusion that an appropriate measurement interval for meaningful data generation would be at least 5 mm and probably 10 mm. Experience indicates that this kind of uncertainty on Δa is not reasonable. A more appropriate level of uncertainty would seem consistent with a significant degree of correlation as discussed above. The data presented in the second plot for each test is based on the somewhat arbitrary assumption of 95% correlation of errors, which effectively eliminates errors on Δa as being a factor in the analysis. The determination of a more appropriate value for the correlation was beyond the scope of the analysis, as is discussed in Section 6. For comparison purposes, the data from this point on in the discussion will be presented assuming that errors on Δa are small and their effect on the results insignificant compared to errors on ΔK caused by uncertainties in the absolute value of crack length.

7.2.2.2 Crack Growth Rate Data for Sensitized Material

The crack growth rate results for the sensitized material are replotted in Figure 7.26. The enclosed areas represent areas bounded by the calculated uncertainties. The shaded area represents the data for room temperature air condition and the open areas represent the high temperature data. The data indicates that there is no statistically significant difference between the crack growth rates ob-

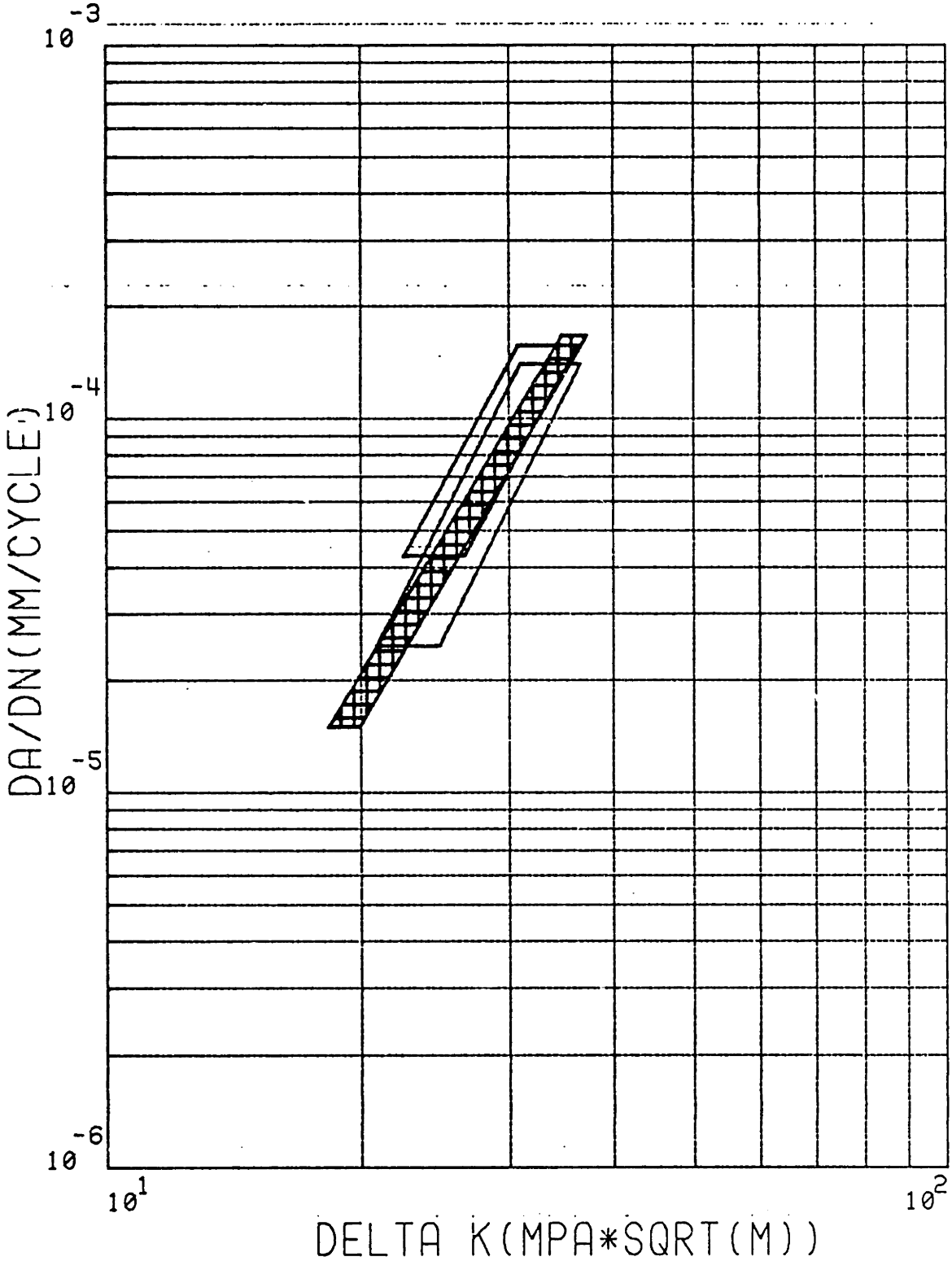

FIGURE 7.26 FATIGUE CRACK GROWTH RATE DATA FOR ALLOY-600 THERMALLY TREATED AT 700 DEG.C FOR 2 HOURS(SENSITIZED). TESTED IN HIGH PURITY DEOXYGENATED WATER AT 288 DEG.C

served at 288°C in deoxygenated high purity water.

7.2.2.3 Crack Growth Rate Data for Desensitized Material

Figure 7.27 shows the results for the desensitized material. If one ignores, for the moment, the upper shaded area, the general conclusions are the same as that for the sensitized material. The data exhibits considerably more scatter between tests but is still consistent with the estimated uncertainties. Comparison of the air data with the high temperature data reveals a weaker dependency of the growth rate of ΔK for the air data.

The upper cross hatched area in Figure 7.27 shows the data for the single test conducted in air saturated water. The data, while requiring confirmation, indicates that crack growth rates are considerably higher in the presence of oxygen. The dependency on ΔK is also less than for the low oxygen tests and is more characteristic of the air tests at room temperature.

7.2.2.4 Comparison of Sensitized and Desensitized Material Behavior

A comparison of Figures 7.26 and 7.27 reveals the following:

The fatigue crack growth rates for sensitized and desensitized material in air at 25°C are virtually identical.

The sensitized material exhibits a slightly lower

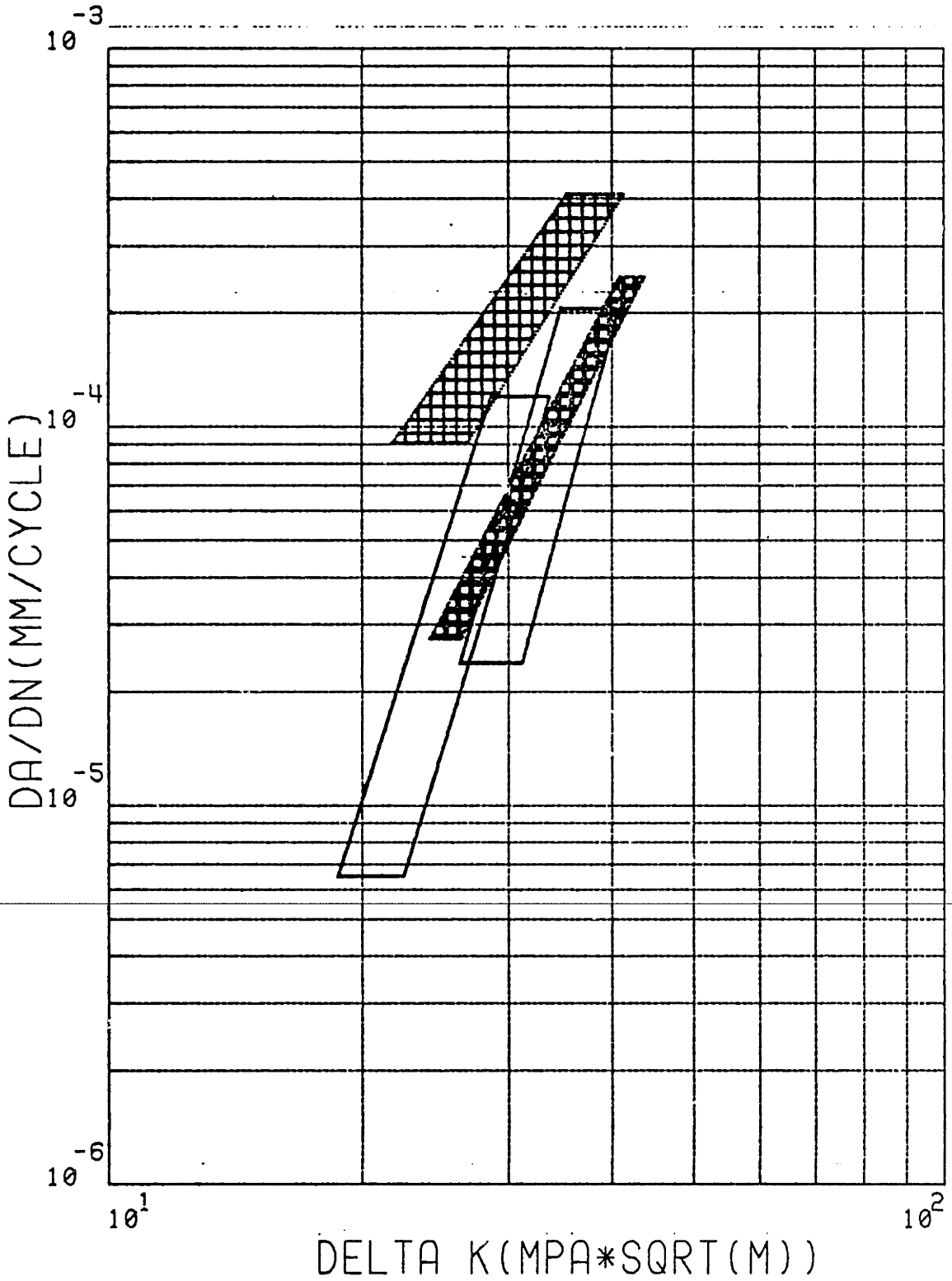

FIGURE 7.27 FATIGUE CRACK GROWTH RATE DATA FOR ALLOY-600 THERMALLY TREATED AT 700 DEG.C FOR 120 HOURS(DESENSITIZED). TESTED IN HIGH PURITY WATER(DEOXYGENATED AND AIR SATURATED), AT 288 DEG.C.

dependency on ΔK than the desensitized material in 288°C high purity deoxygenated water.

The air behavior for both conditions exhibits approximately the same dependence on ΔK.

The crack growth rate for desensitized material in high purity oxygenated water is significantly higher than that for deoxygenated water. The dependence on ΔK is similar to that of the air data for both thermal treatments.

The results of the investigation provides evidence which indicates that the presence of oxygen has a significant effect on the crack growth behavior, which is independent of thermal treatment. This conclusion is supported by the weaker and similar dependency of crack growth rate on ΔK in both air at room temperature and in high purity air saturated water at 288°C. The data also indicates that there may be a marginal effect of heat treatment on fatigue crack growth behavior in high purity deoxygenated water. Some support for this is provided by the generally weaker dependence of crack growth rates on ΔK of the sensitized material than the desensitized material.

7.2.2.5 Fractographic Results

Figures 7.28 - 7.37 show the results of the fractographic analysis of material tested in the sensitized and desensitized condition. Figures 7.28 - 7.32 show the

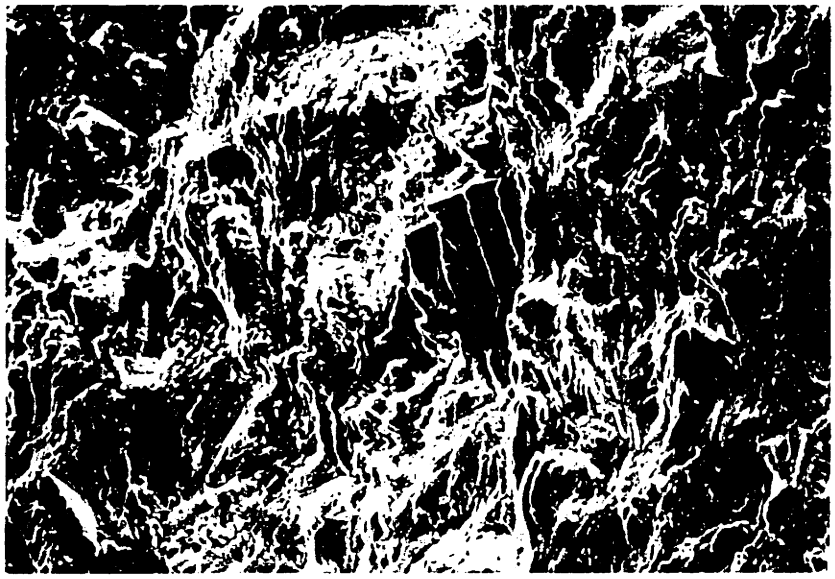

Figure 7.28 Fracture Surface of Sensitized Alloy-600 Showing General Topography, 500X. Crack Path from Bottom to Top. ΔK Approximately 20 MPa $\sqrt{m}$.

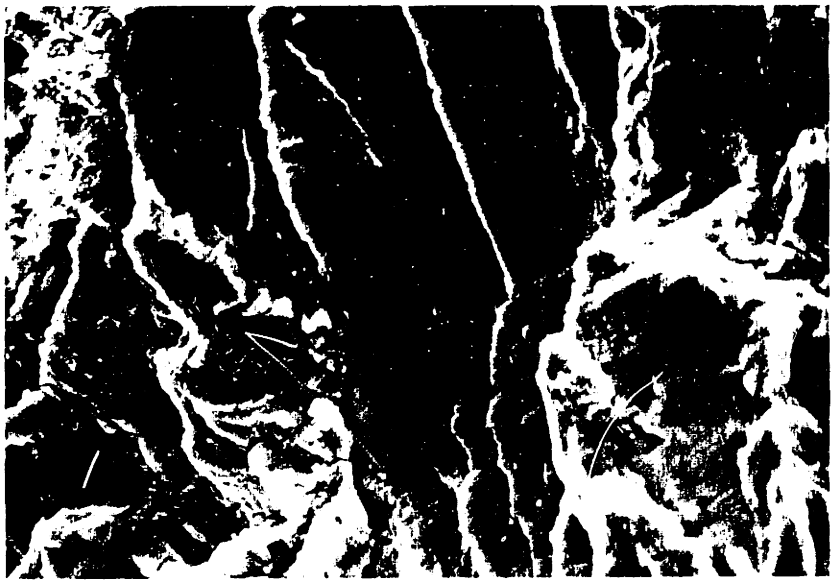

Figure 7.29 Fracture Surface of Sensitized Alloy-600 Showing Crystallographic Crack Path with Striations, 2000X. Crack Path from Bottom to Top. ΔK Approximately 20 MPa $\sqrt{m}$.

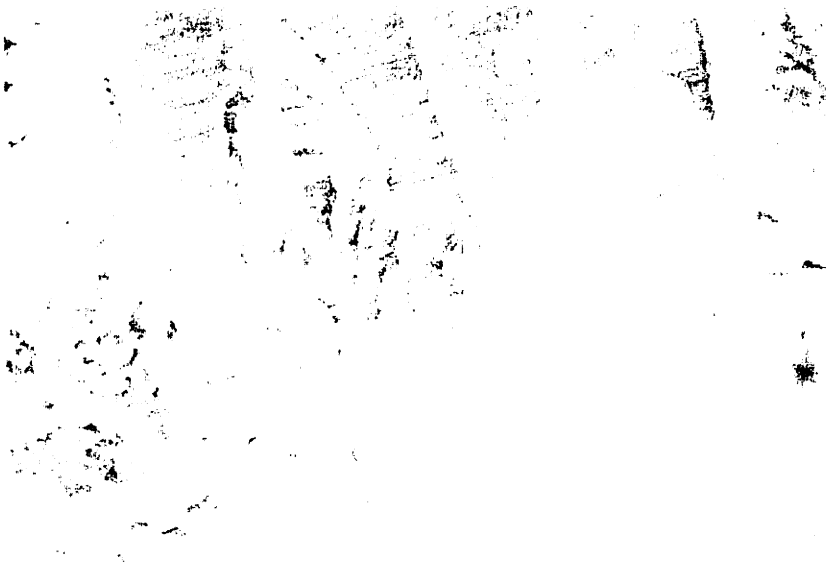

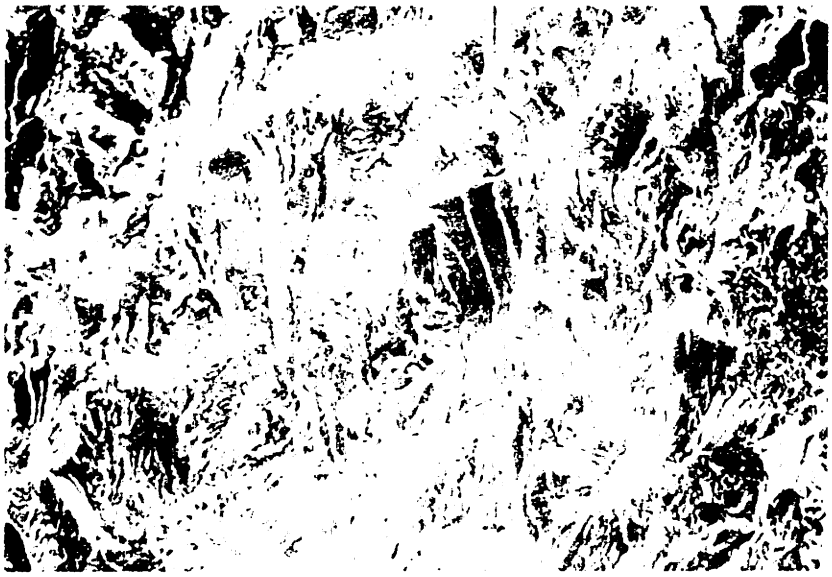

Figure 7.28 Fracture Surface of Sensitized Alloy-600 Showing General Topography, 500X. Crack Path from Bottom to Top. ΔK Approximately 20 MPa $\sqrt{m}$.

Figure 7.29 Fracture Surface of Sensitized Alloy-600 Showing Crystallographic Crack Path with Striations, 2000X. Crack Path from Bottom to Top. ΔK Approximately 20 MPa $\sqrt{m}$.

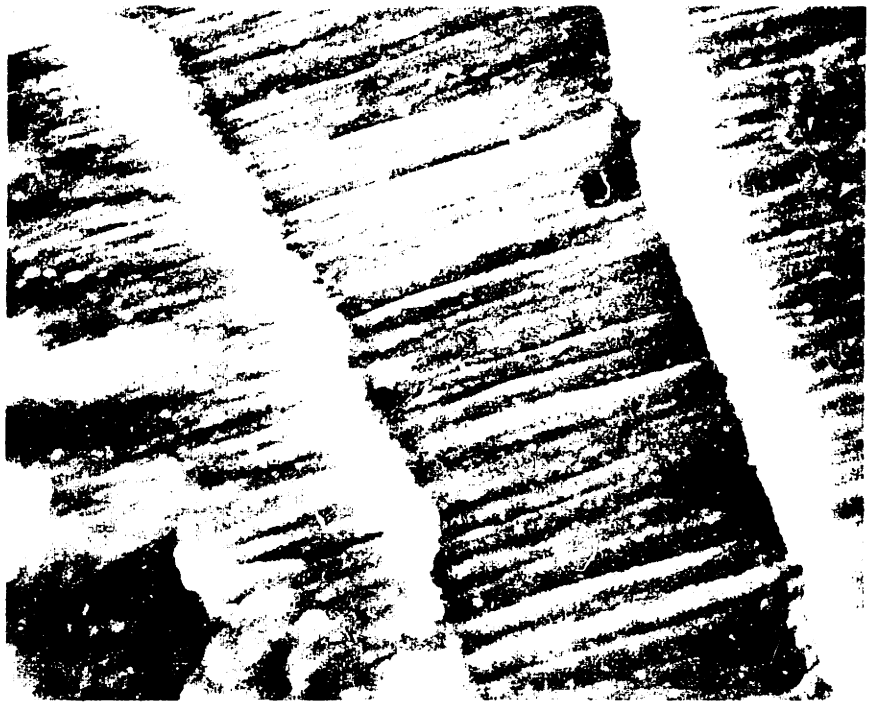

Figure 7.30 Fracture Surface of Sensitized Alloy-600 Showing Fatigue Striations, 10000X. Crack Path from Bottom to Top. ΔK Approximately 20 MPa $\sqrt{m}$.

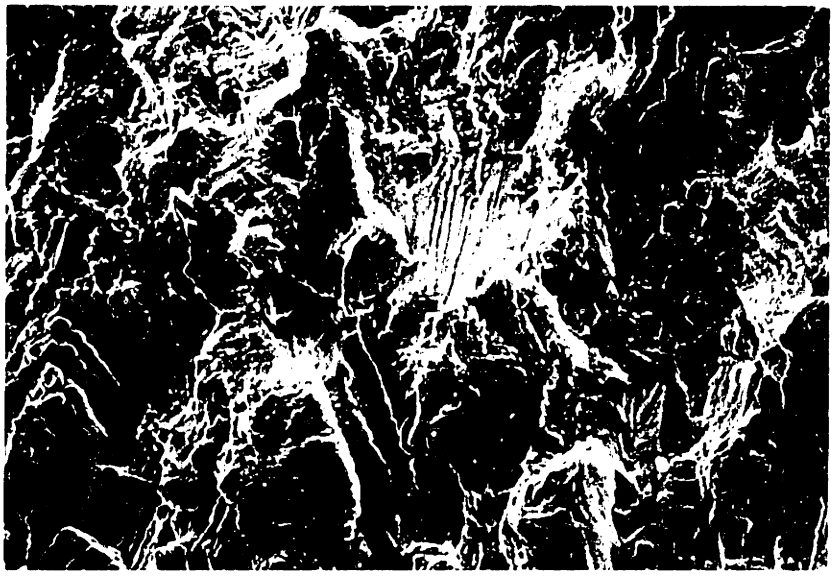

Figure 7.31 Fracture Surface of Sensitized Alloy-600 Showing General Topography, 500X. Crack Path from Bottom to Top. ΔK Approximately 40 MPa $\sqrt{m}$.

Figure 7.32 Fracture Surface of Sensitized Alloy-600 Showing Crystallographic Crack Path with Striations, 2000X. Crack Path from Bottom to Top. ΔK Approximately 40 MPa $\sqrt{m}$.

Figure 7.31 [illegible]

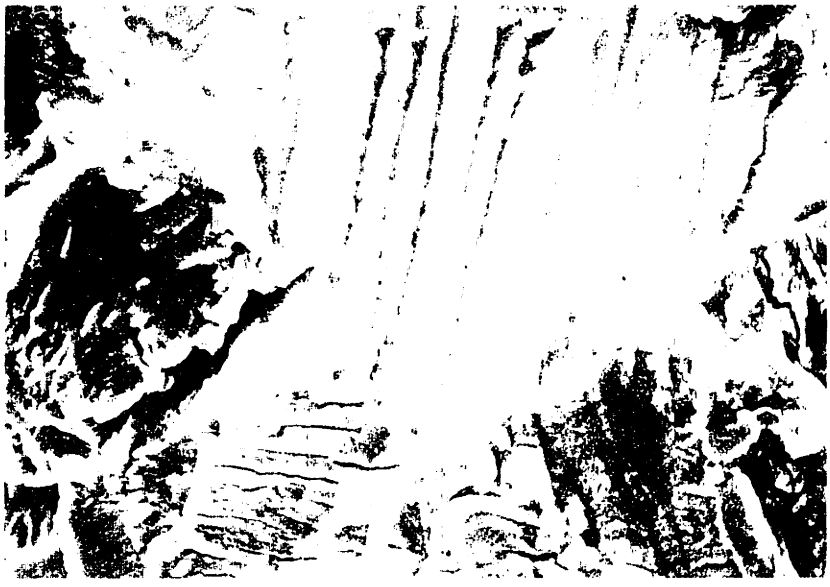

Figure 7.32 Fracture Surface of Sensitized Alloy-600 Showing Crystallographic Crack Path with Striations, 2000X. Crack Path from Bottom to Top. ΔK Approximately 40 MPa $\sqrt{m}$.

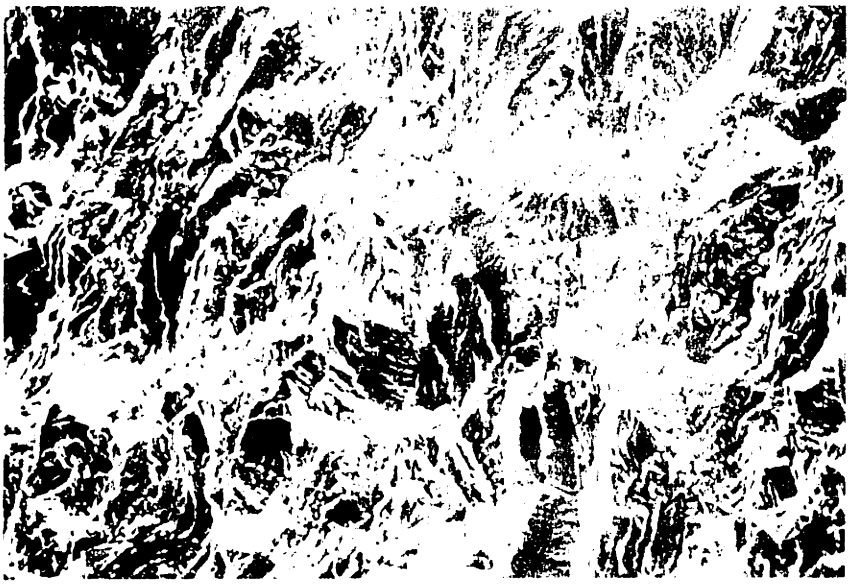

Figure 7.33 Fracture Surface of Sensitized Alloy-600 Showing General Topography, 500X. Crack Path is on Bottom to Top. ΔK Approximately 20 MPa $\sqrt{m}$.

Figure 7.34 Fracture Surface of Desensitized Alloy-600 Showing Crystallographic Crack Path With Striations, 2000X. Crack Path from Bottom to Top. ΔK Approximately 20 MPa $\sqrt{m}$.

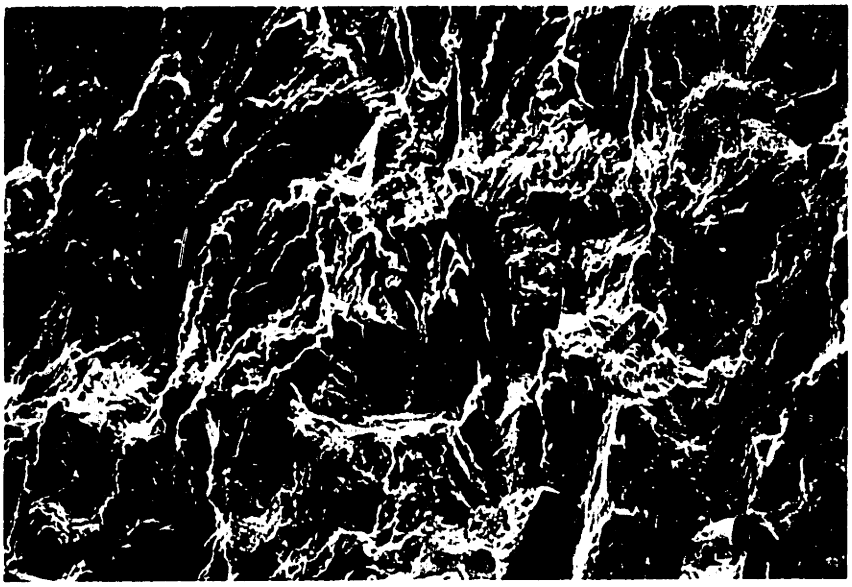

Figure 7.33 Fracture Surface of Sensitized Alloy-600 Showing General Topography, 500X. Crack Path from Bottom to Top. ΔK Approximately 20 MPa $\sqrt{m}$.

Figure 7.34 Fracture Surface of Desensitized Alloy-600 Showing Crystallographic Crack Path With Striations, 2000X. Crack Path from Bottom to Top. ΔK Approximately 20 MPa $\sqrt{m}$.

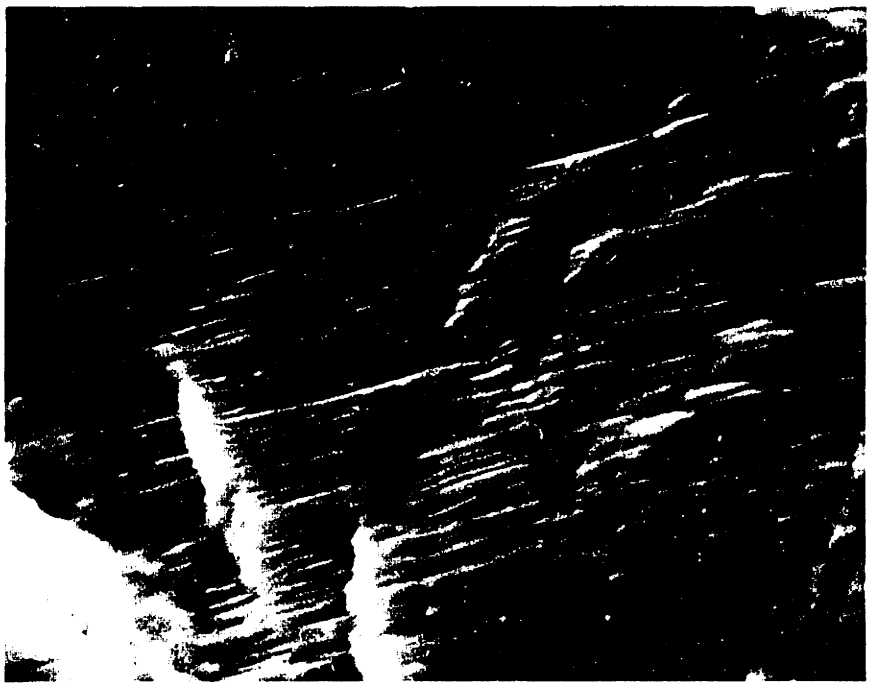

Figure 7.35 Fracture Surface of Desensitized Alloy-600 Showing Fatigue Striations, 10000X. Crack Path from Bottom to Top. ΔK Approximately 20 MPa $\sqrt{m}$.

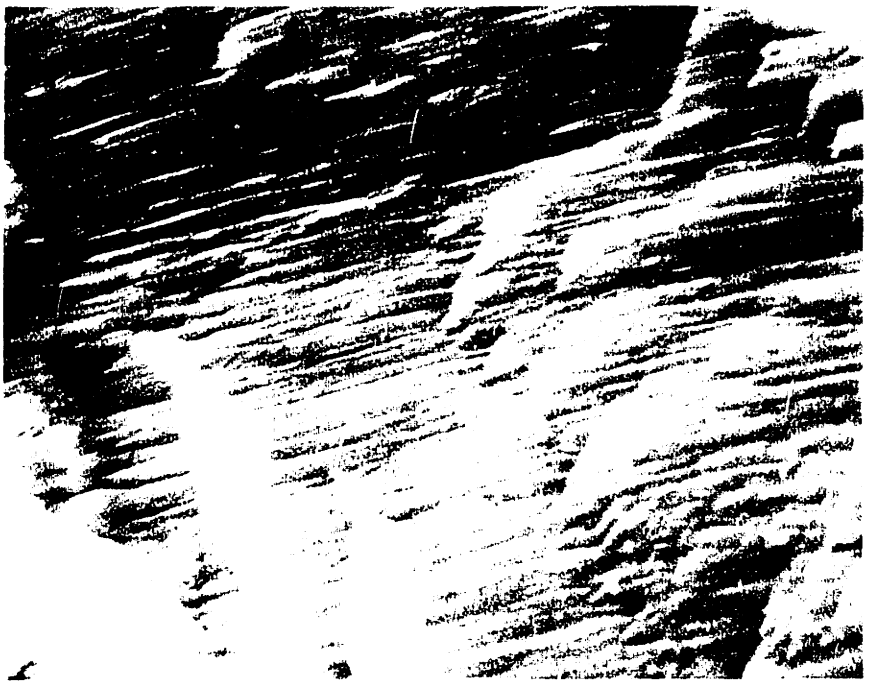

Figure 7.35 Fracture Surface of Desensitized Alloy-600 Showing Fatigue Striations, 10000X. Crack Path from Bottom to Top. ΔK Approximately 20 MPa $\sqrt{m}$.

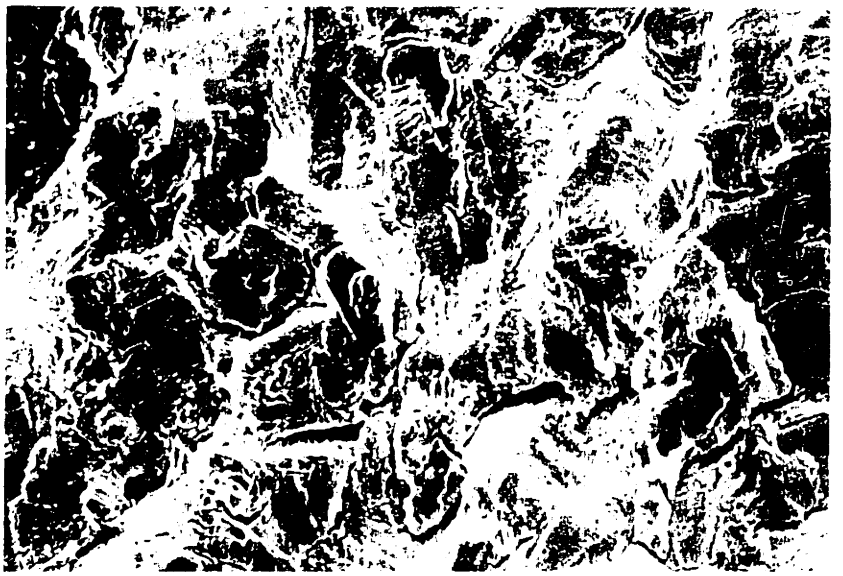

Figure 7.36 Fracture Surface of Desensitized Alloy-600 Showing Fatique Striations, 1000X. Crack Path from Bottom to Top. ΔK Approximately 40 MPa $\sqrt{m}$.

Figure 7.37 Fracture Surface of Desensitized Alloy-600 Showing Crystallographic Cycle Path With Striations, 2000X. Crack Path from Bottom to Top. ΔK Approximately 40 MPa $\sqrt{m}$.

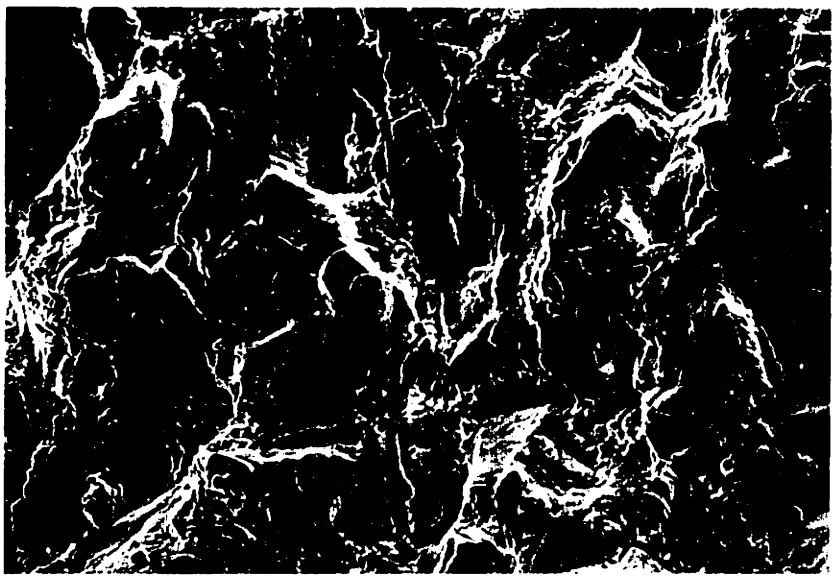

Figure 7.36 Fracture Surface of Desensitized Alloy-600 Showing Fatigue Striations, 1000X. Crack Path from Bottom to Top. ΔK Approximately 40 MPa $\sqrt{m}$.

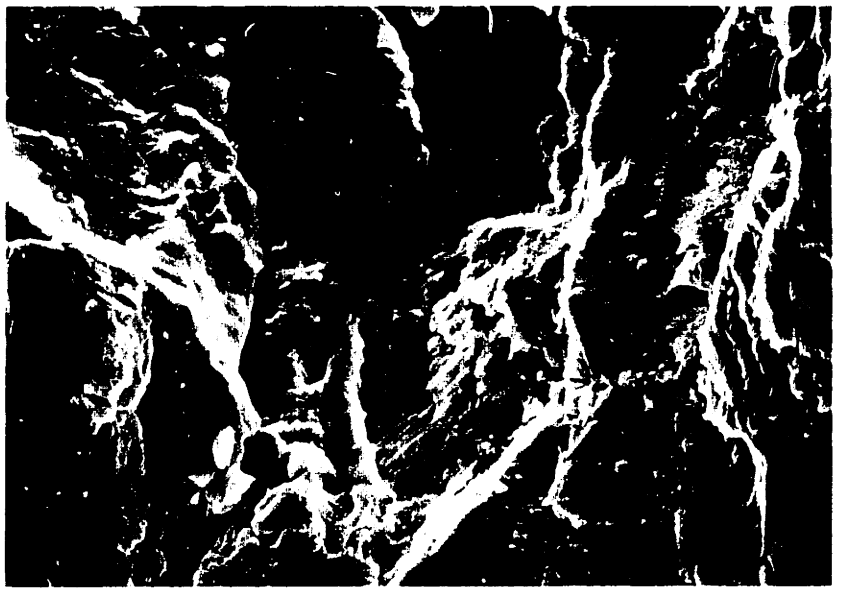

Figure 7.37 Fracture Surface of Desensitized Alloy-600 Showing Crystallographic Cycle Path With Striations, 2000X. Crack Path from Bottom to Top. ΔK Approximately 40 MPa $\sqrt{m}$.

fracture surface of a sensitized specimen tested in high purity deoxygenated water at 288°C. Figures 7.33 - 7.37 show the fracture surface of a desensitized specimen tested under the same conditions. These micrographs are representative of all specimens tested in the program. The fracture surfaces are characterized by a transgranular crack path with a tendency to by crystallographic in nature. Fatigue striations are evident on crystallographic surfaces. Crack branching is more prevalent at the higher ΔK values. The fatigue striation specing agrees well with the calculated crack growth rates. As is illustrated by the higher magnification micrographs, there is little oxide present on the fracture surfaces. This is consistent with the presence of a low oxygen environment at the crack tip.

7.2.2.6 Comparison With Previous Results

Figures 7.38 and 7.39 show the data for the sensitized and desensitized material compared with previously reported data. In general, the data generated for this study is in agreement with other more or less similar data. The only reasonably direct comparison of test conditions, however, are for tests in air and for the single test conducted in high purity air saturated water. Even for these tests it is not clear that the metallurgical conditions are comparable. The reference numbers in the Figures refer to the source of the individual data sets.

General agreement exists between fatigue crack growth

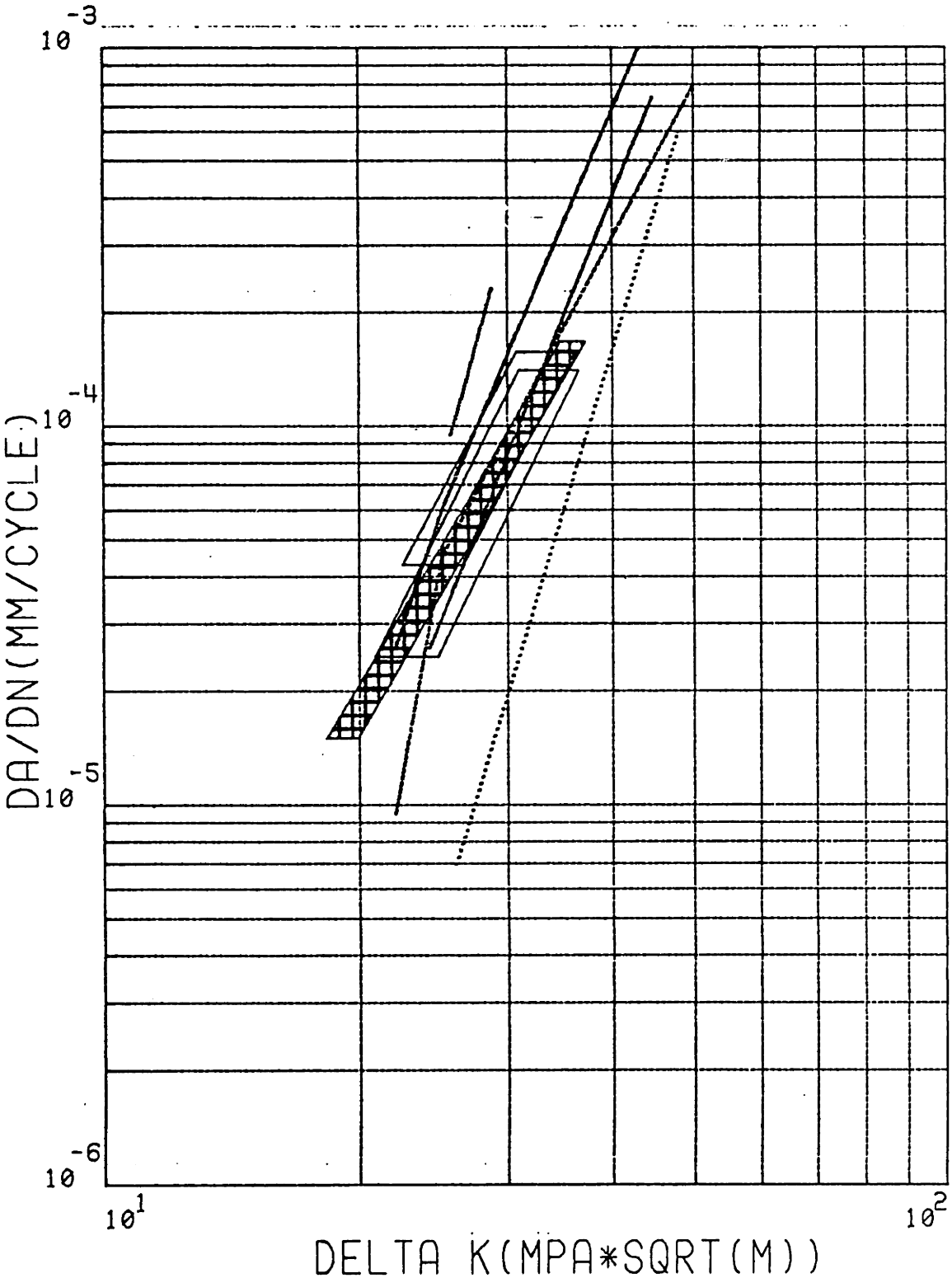

FIGURE 7.38 COMPARISION OF PREVIOUSLY REPORTED FATIGUE DATA FOR ALLOY-600 WITH THAT FROM THIS INVESTIGATION. MATERIAL TESTED IN THE SENSITIZED CONDITION. SHADED AREA, R.T. DATA THIS INVEST.

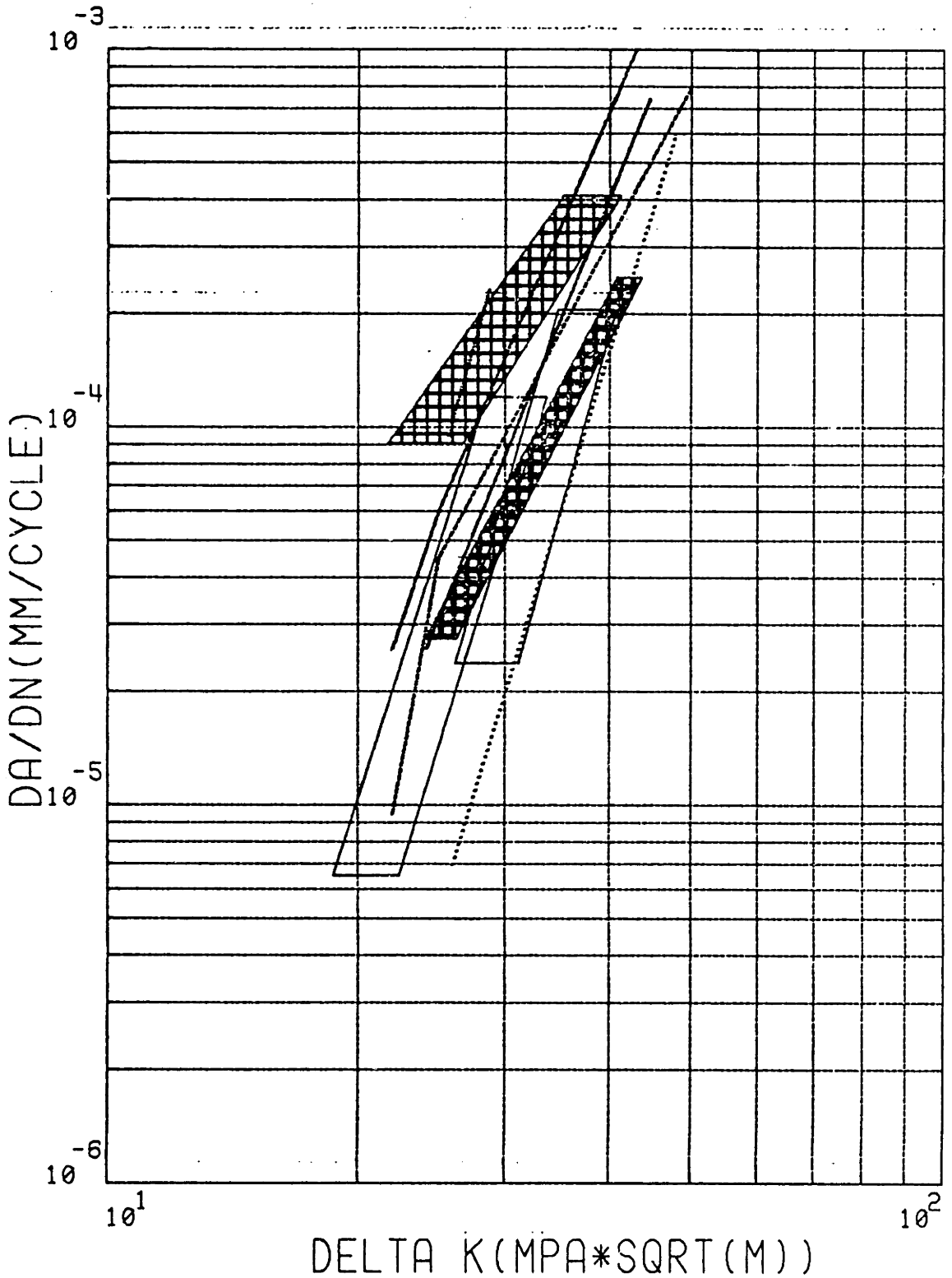

FIGURE 7.39 COMPARISION OF PREVIOUSLY REPORTED FATIGUE DATA FOR ALLOY-600 WITH THAT FROM THIS INVESTIGATION. MATERIAL TESTED IN THE DESENSITIZED CONDITION.

data generated in low oxygen environments. The data of Mills and James [12] for Alloy-600 material tested in low oxygen sodium, agrees wtih data from this program for tests in high purity deoxygenated water.

Another significant area of agreement is between Hale's [11] data for 288°C air saturated high purity water and the high oxygen test conducted in this study. This is further evidence for a significant effect of oxygen.

The data from the work of Was [13] is generally below that from this and other studies. The reason for this difference is not clear but his work was conducted with material annealed at 1150°C for 30 min. The results of the high temperature anneal were a grain size of 150 mm and a yield strength of 150 MPa. His material was thus, not typical of material in service. The extremely low yield stress could have resulted in large amounts of plasticity at the crack tip and promoted closure effects, which would have retarded crack growth. Additionally, his specimen design used 3.2 mm thick sheet while the other investigators, including this one, used a compact tension design with a minimum thickness of 12.7 mm.

The fractographic results discussed in Section 7.2.2.5 are in good agreement with those of Mills and James [12].

8.0 Summary and Conclusions

As a result of the overall experimental program, the following tasks were accomplished and conclusions drawn.

An experimental facility has been designed and constructed for the investigation of fatigue and stress corrosion cracking behavior of materials in the temperature and pressure range prototypic of Light Water Reactor (LWR) operating conditions. The system consists of three 3.8 liter titanium autoclaves, one of which is installed in conjunction with a servohydraulic fatigue machine, and associated piping and support systems. The nominal system operating temperature and pressure are 288°C and 13.7 MPa, respectively.

Experimental and analytical techniques for the generation and analysis of fatigue crack growth data in high temperatures and pressures in an autoclave system have been established and verified. A complete uncertainty analysis of the overall experimental and analytical procedures has been conducted. Confidence limits have been established for data generated using the autoclave system described above.

The results of the uncertainty analysis indicates that the dominant source of error in the system is the potential uncertainty in the calibration of the crack mouth opening displacement gauge used for compliance measurements. The analysis indicates that a potential uncertainty in crack length of ± 1-1.5 mm can be expected for tests performed at high temperature and pressure.

The overall validity of the uncertainty analysis and data reduction techniques have been demonstrated by the confirmation of calculated crack length with actual measurements. Additional confirmation has been established through the use of Monte Carlo simulations of experiments. A significant reduction in overall uncertainty would be achieved by automation of the calibration and data acquisition functions because of an increased capability to take simultaneous measurements of system variables.

The results of the uncertainty analysis indicate that a significant error in ΔK can occur as a result of uncertainty in the absolute value of crack length. A large uncertainty does not necessarily indicate that there exists a correspondingly large error in crack length increment, however. The expected error in the increment in crack length can be expected to be significantly less than errors in absolute crack length due to a high correlation between errors in crack length at the end points of the interval. The exact extent of the potential correlation was not determined in this program.

An investigation of the effect of heat treatment on the fatigue crack growth behavior of Alloy-600 has been conducted using the autoclave system. Fatigue crack growth tests have been conducted at 288°C in deoxygenated and air saturated water, respectively. These conditions simulate primary system environments for Pressurized Water Reactors (PWR) and Boiling Water Reactors (BWR), respectively.

Material in two thermally treated conditions were investigated; (1) sensitized by aging at 700°C for 2 hours, and (2) desensitized by aging at 700°C for 120 hours.

The results of the investigation indicate that there is little or no effect of thermal treatment on the fatigue crack growth behavior of Alloy-600 in deoxygenated high purity water at 288°C. Fatigue crack growth rates in high purity deoxygenated water at 288°C are not significantly different than those for room temperature air tests. However, the results of the investigation indicate that there is a significant effect of oxygen on the material behavior. For Alloy-600 desensitized by aging at 700°C for 120 hours, a difference in crack growth rates of up to an order of magnitude may exist in the ΔK range of 15-30 MPa $\sqrt{m}$, with material tested in air saturated water exhibiting the higher growth rate.

The data generated in this investigation agrees well with data from previous investigations, although direct comparison of data from this investigation with that of others was not totally possible due to a lack of data for the test conditions of interest.

9.0 Recommendations for Future Work

Based on the experience gained as a result of the experimental and analytical program, a number of recommendations for future work suggest themselves. These recommendations are as follows:

In the area of data acquisition and analysis, the automation of the acquisition and reduction functions can be expected to result in a significant improvement in system precision. The increase in precision would result from better system calibration, especially with respect to the COD gauge.

The overall applicability of the uncertainty analysis with respect to da/dn vs ΔK would be greatly improved if a reasonable value for the correlation coefficient between crack length errors over a short interval in crack length could be obtained. The required correlation analysis could be conducted if sufficient data were available for a statistical analysis of the uncertainty in the compliance calibration curve used in the analysis.

Additional tests should be performed using Alloy-600 material with the same heat treatments as

those used in this investigation to confirm the results. Particular emphasis should be placed on tests performed in air saturated high purity water.

Since the results of this investigation indicate the presence of an effect of oxygen on fatigue crack growth rates, a frequency effect might also be present. The effect of frequency should be investigated by performing tests at lower frequencies where the effect of oxygen may be magnified.

The presence of an oxygen effect also indicates that an effect of mean stress might be present. The effect of mean stress should be investigated at higher R ratios, where effects due to time dependent stress assisted cracking may manifest themselves.

References

[1] C. W. Pryor, G. F. Glei and P. A. Sherburne, "Babcock and Wilcox Nuclear Steam Generator Operating Experience," Presentation to Joint Power Generation Conference, Charlotte (1979), Babcock and Wilcox Report BR-1140.

[2] G. P. Airey, Principal Investigator, EPRI Project RP1708-1, "Optimization of Metallurgical Variables to Improve the Stress Corrosion Resistance of Inconel-600".

[3] J. Blanchet, H. Couriou, L. Grall, C. Mahieu, C. Otter, and G. Turloer, "Influence of Various Parameters on Intergranular Cracking of Inconel-600 and X-750 in Pure Water at Elevated Temperature," in Stress Corrosion Cracking and Hydrogen Embrittlement of Iron Base Alloys, Firminy, France, June 1973.

[4] H. R. Copson and G. Economy, "Effect of Some Environmental Conditions on Stress Corrosion Behavior of Ni-Cr-Fe Alloys in Pressurized Water," Corrosion, Vol. 24, No. 3, pp. 56-65, March 1968.

[5] H. Domain, R. H. Emanuelson, L. Katz, L. W. Sarrer, and G. J. Theus, "Effect of Microstructure on Stress Corrosion Cracking of Alloy-600 in High Purity Water," Technical Paper ADTPA-75-18, Babcock and Wilcox, March 1976.

[6] H. Couriou, L. Grall, P. Oliver and H. Willermoy, "Influence of Carbon and Nickel Content on Stress Corrosion Cracking of Austinitic Stainless Alloys in Pure Chlorinated Water at 350°C, " in Fundamental Aspects of Stress Corrosion, The Ohio State University, Sept. 1967, Ed. R. W. Staehle, A. J. Forty and D. Van Rooyen, NACE, Houston, TX (1969).

[7] R. C. Scarberry, S. C. Pearman and J. R. Crum, "Precipitation Reactions in Inconel Alloy-600 and Their Effect on Corrosion Behavior," Corrosion, Vol. 32, No. 10, pp. 401-406, October 1976.

[8] C. S. Tedmon Jr., and D. A. Vermilyea, "Carbide Sensitization and Intergranular Corrosion in Nickel Base Alloys," Corrosion, Vol. 27, No. 9, pp. 376-381, September 1971.

[9] M. O. Speidel, "Corrosion Fatigue in Fe-Ni-Cr Alloys", in Stress Corrosion Cracking and Hydrogen Embrittlement of Iron Base Alloys, Firming, France, 1071 (1973).

[10] L. A. James, "Fatigue Crack Propagation Behavior of Inconel-600," Int. J. Pres. Ves. & Piping (5), 1977.

[11] D. A. Hale, C. W. Jewett, J. N. Kass, "Fatigue Crack Growth Behavior of Four Structural Alloys in High Temperature High Purity Oxygenated Water", J. Eng. Mat. Tech., Vol. 101, pp. 191-198, July 1979.

[12] W. J. Mills and L. A. James, "The Fatigue-Crack Propagation Response of Two Nickel-Base Alloys in a Liquid Sodium Environment", ASME Pressure Vessel and Piping Conference, San Francisco, June 25-29, 1979.

[13] G. S. Was, ScD Thesis, Massachusetts Institute of Technology, May 1980.

[14] A. Saxena and S. J. Hudak, Jr., "Review and Extension of Compliance Information for Common Crack Growth Specimens", Int. J. of Fracture, Vol. 14, No. 5, Oct. 1978.

[15] J. C. Newman, Jr., "Stress Intensity Factors and Crack Opening Displacements for Round Compact Specimens," NASA Technical Memorandum 80174, Oct. 1979.

[16] J. C. Newman, Jr., "Stress Analysis of the Compact Specimen Including the Effects of Pin Loading", ASTM STP 560, 1974, pp. 105-121.

[17] S. J. Hudak, Jr., A. Saxena, R. J. Bucci, and R. C. Malcolm, Development of Standard Methods of Testing and Analyzing Fatigue Crack Growth Rate Data, AFML-TR-78-40, Dec. 1977.

[18] J. C. Newman, "Crack Opening Displacements in Center Crack, Compact and Crack Line Wedge Loaded Specimens", NASA-TN-D-8628.

[19] W. K. Wilson, Eng. Fracture Mechanics, Vol. 2, 1970, pp. 169-171.

[20] R. G. Ballinger, R. M. Latanision, W. C. Moshier, R.M.N. Pelloux, "The Role of Uncertainty in the Measurement of Crack Length by Compliance Techniques", International Specialists Meeting on Subcritical Crack Growth, Freiburg, W. Germany, May 13-15, 1981.

[21] P. R. Bevington, Data Reduction and Error Analysis for the Physical Sciences, New York, McGraw-Hill, 1969.

[22] R. Ballinger, UCRAK--A Program to Estimate Uncertainty in Crack Growth Data, Report to the Electric Power Research Institute, October 1981.

[23] S. T. Rolfe, J. M. Barsom, Fracture and Fatigue Control in Structures-Applications of Fracture Mechanics, Prentice-Hall, Englewood Cliffs, New Jersey, 1977.